HARVARD UNIVERSITY
Graduate School of Arts and Sciences



DISSERTATION ACCEPTANCE CERTIFICATE

The undersigned, appointed by the

Department of Chemistry & Chemical Biology

have examined a dissertation entitled:

Patterning Metal Oxides Using Electrochemical Methods and Exploring the Dynamics of Water-Splitting Catalysts

presented by : Evan Charles Jones

candidate for the degree of Doctor of Philosophy and hereby certify that it is worthy of acceptance.

Signature _____
Typed name: Professor Daniel G. Nocera

Signature _____
Typed name: Professor George Whitesides

Signature _____
Typed name: Professor Yogesh Surendranath

Date: 16 April 2018

Patterning Metal Oxides Using Electrochemical Methods and Exploring the Dynamics of Water-Splitting Catalysts

A dissertation presented

by

Evan Charles Jones

to

The Department of Chemistry and Chemical Biology
in partials fulfillment of the requirements

for the degree of

Doctor of Philosophy
in the subject of
Chemistry

Harvard University
Cambridge, Massachusetts

April 2018

© 2017 – Evan Charles Jones

All rights reserved.

Dissertation Advisor: Professor Daniel G. Nocera Evan Charles Jones

Patterning Metal Oxides Using Electrochemical Methods and Exploring the Dynamics of Water-Splitting Catalysts

Artificial photosynthesis is the electrochemical decomposition of water into oxygen and hydrogen driven by solar energy, allowing for the storage of solar energy in chemical bonds. Integrated photoelectrochemical cells (PECs), such as the "artificial leaf," have the potential to reduce the cost of artificial photosynthesis. In a buried-junction PEC configuration, a catalyst for the oxygen evolution reaction (OER) is deposited onto one surface of a photovoltaic, with a catalyst for the hydrogen evolution reaction (HER) deposited on the opposite side. Such designs eliminate the need for metallic wires, thereby reducing the material cost of the device.

A problem faced by the artificial leaf is a loss in efficiency resulting from the absorption of sunlight by the catalyst. Catalysts can be appropriately distributed using lithography, but at a significant expense of time and material. In view of this challenge, simple electrochemical methods can be used to control the distribution of catalyst on a substrate. Here, we examine an electrochemical method that allows for the patterning of metal oxides over conductive surfaces. Reactive interfacial patterning promoted by lithography, or "RIPPLE," allows for the formation of sub-micron ridges of oxide by employing cyclic voltammetry. The method is expanded to include oxides that are known as efficient OER catalysts. Furthermore, the tolerance of this method to pattern electrochemically-deposited metal films, as well as metal films on rough substrates, suggests it is well suited for patterning catalysts in a scalable fashion.

We find that the patterns generated by RIPPLE using a linear potential scan (cyclic voltammetry) can be identically reproduced by utilizing a square wave function (binary-potential step method). The reduction of applied potentials not only simplifies the method, but also sheds light on the mechanism by which the patterns are formed. A scaling analysis reveals the mass transport limitations that govern pattern formation. We further investigate how the lithographic resist influences mass transport. Understanding this relationship inspires a new patterning technique that allows us to substitute the lithographic resist with an emulsion. Finally, we attempt patterning at a triple-phase interface, thereby obviating the masking requirement altogether.

The dynamics of metal oxides under OER catalysis is of relevance to the preservation of oxide patterns. An oxide undergoing dynamic changes to its surface would result in a homogenously distributed film. We explore the dynamics of a Co oxide-based OER catalyst as a function of pH, which elucidates fundamental behavior of the catalyst during deposition and OER operation. Furthermore, we investigate dynamic catalysts that exploit the equilibria observed under dynamic conditions.

TABLE OF CONTENTS

Title Page i
Copyright Page ii
Abstract iii
Table of Contents iv
List of Figures viii
List of Tables xix
Acknowledgments xx

Part 1. Introduction 1
1.1 Motivations for solar energy 2
1.1.1 Fossil fuels and conventional energy production 2
1.1.2 Solar energy 4
1.2 The components of a competitive solar energy system 6
1.2.1 Converting solar energy 6
1.2.2 Cheap PVs are not enough 6
1.2.3 Using the oxidation of water to store energy 8
1.2.4 Overpotential 9
1.2.5 Hydrous metal oxide films for OER 10
1.3 Integrated water-splitting devices 13
1.3.1 PV and OEC interplay in a PEC 15
1.3.2 Catalyst loading 16
1.4 Patterning materials 18
1.4.1 Catalyst distribution 18
1.4.2 Electrochemical micromachining 20
1.4.3 RIPPLE 20
1.5 Overview 22
1.6 References 24

Part 2. Expanding the applicability of RIPPLE beyond Ge to other materials and substrates 29
2.1 Introduction 30
2.2 Results 31
2.2.1 Electron beam deposited Co 31
2.2.2 Electron-beam deposited Ni and the effect of chloride ions 33
2.2.3 RIPPLE on rough substrates 35
2.2.4 Patterning electroplated Co 36

2.2.5 Performing catalysis with a patterned Co film 39
2.2.6 Plasma-enhanced reduction 42
2.3 Discussion 42
2.3.1 Patterning cobalt metal 42
2.3.2 Patterning in the presence of chloride 50
2.3.3 Patterning cobalt films on FTO 52
2.3.4 Patterning electroplated Co 53
2.3.5 Oxygen evolution on RIPPLE patterns 54
2.3.6 Reducing Ge and Co patterns 55
2.4 Conclusion 56
2.5 Experimental Methods 57
2.5.1 Substrate preparation 57
2.5.2 Electrochemical methods 58
2.5.3 Catalyst preparation and characterization 59
2.5.4 Plasma reduction 59
2.5.5 Microscopy 60
2.6 References 60

Part 3. Development and mechanistic studies of a binary potential step patterning method **62**
3.1 Introduction 63
3.2 Results 64
3.2.1 Patterning Co by a binary potential step method 64
3.2.2 Correlating applied potential to pattern evolution 67
3.2.3 Patterning Ge by a binary potential step method 68
3.2.4 Investigating the influence of Co^{2+} under the resist 71
3.2.5 Modeling Co diffusion and ring spacing 73
3.3 Discussion 75
3.3.1 Developing a binary potential step method for RIPPLE-like pattering of Co 75
3.3.2 Co redox behavior under patterning conditions 76
3.3.3 Comparing patterns formed in Co and Ge 76
3.3.4 Dependence of pattern formation on Co^{2+} 78
3.3.5 Developing and evaluating the Co pattern model 80
3.4 Conclusion 84
3.5 Experimental Methods 85
3.5.1 Working electrode fabrication 85
3.5.2 General electrochemical methods 86
3.5.3 Microscopy 87

3.6 References 87

Part 4. Studying resist behavior and developing a method for lithography-free electrochemical patterning **89**

4.1 Introduction 90
4.2 Results 92
4.2.1 AFM analysis of resist 92
4.2.2 Modulating resist thickness 92
4.2.3 Electrochemical pattering with lacquer beads 96
4.3 Discussions 97
4.3.1 Resist behavior under patterning conditions 97
4.3.2 Influence of the resist's properties on underlying pattern geometry 98
4.3.3 Electrochemical patterning with emulsions as a lithography-free approach 98
4.4 Conclusion 99
4.5 Experimental Methods 100
4.5.1 Working electrode fabrication 100
4.5.2 General electrochemical methods 101
4.5.3 Microscopy 102
4.6 References 102

Part 5. Patterning at a triple-phase boundary **104**

5.1 Introduction 105
5.2 Results 106
5.2.1 Electrochemically-generated air-liquid interfaces 106
5.2.2 Patterning in a vertical configuration at a triple phase boundary 107
5.2.3 Optical and electrochemical characterization of the patterned samples 110
5.2.4 Determining cell potential 112
5.2 Discussion 114
5.3.1 Electrochemically-generated, redox active moving boundaries 114
5.3.2 Electrochemical patterning using a dip coater method 115
5.3.3 Electrochemical and optical properties of patterned Co 117
5.3.4 Converting from a three-electrode configuration to a two-electrode configuration 118
119
5.4 Conclusion 120
5.5Experimental Methods 120
5.5.1 Substrate preparation 120
5.5.2 General electrochemical methods 120

5.5.3 Patterning under H_2 bubbles 121
5.5.4 Patterning at the solution-air interface 121
5.5.5 Microscopy 122
5.5.6 Integrating sphere spectroscopy 122
5.6 References 122

Part 6. Exploring the dynamics of the pre-catalyst for oxygen evolving catalysts **124**
6.1 Introduction 125
6.2 Results 127
6.2.1 Co-OEC migration 127
6.2.2 Co-OEC under acidic conditions 130
6.2.3 Dissolution of CoP_i films in 0.1 M H_3PO_4 133
6.2.4 Exploring Fe acid-stable OER catalysts 137
6.2.4.1 Fe(III) nitrate 137
6.2.4.2 Fe(III) acetate 138
6.2.4.3 Fe(III) and Fe(II) sulfate 143
6.2 Discussion 143
6.2.1 Evaluating the dynamic of CoP_i under catalytic conditions 143
6.3.2 Studying CoP_i under dynamic conditions 147
6.3.3 CoP_i deposition onto an FTO electrode 150
6.3.4 Assessing materials as dynamic precatalysts for an acid-stable electrolysis system 151
6.3.4.1 Fe(III) nitrate 156
6.3.4.2 Fe(III) acetate 157
6.3.4.3 Fe(III) and Fe(II) sulfate 160
6.3.5 Towards engineering a competitive OER system 160
6.4 Conclusion 161
6.5 Experimental Methods 162
6.5.1 General electrochemical methods 162
6.5.3 Co-OEC pre-catalyst preparation 163
6.5.4. Detecting Co migration using a four-electrode configuration 164
6.5.5 Spectrometric quantification of Co 164
6.5.6 O_2 measurements 164
6.5.7 *In situ* electrochemical UV-Vis spectroscopy 165
6.5.8 Microscopy 165
6.6 References 166

LIST OF FIGURES

Figure 1.1. (a) Atmospheric CO_2 as measured from Mauna Loa Observatory, Hawaii (e.g. the Keeling Curve). Longest record of direct measurements of CO_2 (—) and seasonally corrected data (—). Data from Reference 5. (b) Model depicting greenhouse effect. Temperature without greenhouse gases (—), with natural greenhouse gases (—), and with anthropogenic CO_2 (—). Readapted from Reference 7. 3

Figure. 1.2. The Sun is an ideal source of energy. Left: The Sun is depicted with sustained nuclear fusion occurring in its core. Center: Solar radiation diffuses through space and eventually reaches the Earth, where some is absorbed and reflected by the atmosphere. Readapted from Reference 18. Right: The daily availability of terrestrial solar energy on Earth's surface, showing relative intensity of sunlight representative for daily time course. 5

Figure 1.3. Economic viability of a solar energy system for a homeowner. Plot assumes California household with a 10 MWh demand, a 4 kW PV array, a 4 kWh battery, and flat retail rates. Prices as of December 2015 shown as gray oval. Rooftop PV modules only add net present value (NPV) to a home if electricity retail rates increase, or PV or storage systems decrease. Readapted from Reference 21. 7

Figure 1.4. Co-OEC, a hydrous metal oxide catalyst for the OER half-reaction. (a) Structure of catalyst as determined from XAS with octahedral Co (blue spheres) bound to bridging O (red spheres).. (b) Edge sites are the proposed active sites of Co-OEC. Mn-OEC and Ni-OEC are proposed to have analogous bulk structures and bridging-oxo active sites. Reprinted with permission from Casey Brodsky. 11

Figure 1.5. Schematic of an integrated, wireless solar water-splitting device. The hydrogen evolving catalyst (HEC) can be NiMoZn or CoP. 13

Figure 1.6. (a) Exchange current density as a function of charge passed during film deposition. Charge passed correlates with the number of active sites, which increases activity and film thickness. This results in a diffusion limitation to active sites. Activity is predicted to obey $I_0=I_0^{max}\tanh(Q_{dep}/Q_{dep}^{opt})$, where I_0^{max} is exchange current limited by diffusion and Q_{dep}^{opt} is where activity begins to become less dependent on film thickness. The red square marks the charge passed for the film 16

shown in (b). (b) Co-OEC film (below yellow tape) on FTO illustrating parasitic light absorption of a film were Q_{dep} = 300 mC/cm^2.

Figure 1.7. Catalytic waves for OER catalysts with high (—) and low (—) Tafel slopes overlaid with j-V curves for a buried junction device before (—) and after (—) catalyst loading. Dashed lines show relative operating current densities for the four combinations. 17

Figure 1.8. Schematics of PECs with various OEC loadings and distributions. (a) Thick, homogenously distributed OEC significantly blocks PV from light (b) Homogenously distributed OEC must be extremely thin (3 nm, far below Q_{dep}^{opt}) in order not to impair PEC efficiency. (c) Thick OEC distributed on half of the PEC allows light transmission, but holes must flow from the most distal excited site (yellow circle) and to the most distal active site (blue circle), thereby increasing resistive loss (ρ of FTO = 7–41 Ω/sq). (d) Evenly distributed OEC shortens the path length that holes must travel to reach active sites. (e) Further distributing OEC increases mass transport, but also results in higher current densities. (f) Combination of (b) and (e) yet to be explored. 19

Figure 1.9. The RIPPLE technique, as first reported, can be summarized in 8 steps represented by the arrows: 1. Substrate surface is prepared for coating (p-Si is etched) 2. Optional protective layer, such as ITO, is sputtered onto the substrate. 3. Material film is deposited. 4. Resist is spin-coated over film. 5. Resist is exposed using lithography. 6. Resist is developed. 7. Cyclic voltammetry is performed on the sample. 8. Resist is stripped off. 21

Figure 2.1. (a) SEM image (SE2 detector) of a 250 nm Co film patterned by RIPPLE by cycling from 0.4 V to and from 1.3 V at 100 mV/s in 0.1 M H_2SO_4. (b) Cyclic voltammogram used to generate pattern in (a). Scan order designated on left side. (c) SEM image (SE2 detector) of a 250 nm Co film patterned by RIPPLE by cycling from 0.4 V to and from 1.3 V at 100 mV/s in 0.1 M K_2SO_4. 31

Figure 2.2. Patterns generated by cyclic voltammetry, with five cycles from 0.4 V to and from 1.3 V at 100 mV/s in 0.1 M K_2SO_4. (a) SEM images (In-lens detector, grey) and EDS maps for cobalt (green), oxygen (red), and silicon (blue). (b) 3D rendering of AFM height data with height profile of diametric cross-section (inset on bottom right). 32

Figure 2.3. Patterning metals by RIPPLE in the presence of Cl^-. (a) SEM image (SE2 detector) of a 250 nm Ni film patterned by RIPPLE by cycling from 0.4 V to and from 1.3 V at 100 mV/s in 0.1 M H_2SO_4 and 0.5 M KCl. (b) AFM height map for a pattern in (a). (c) SEM image (SE2 detector) of a 250 nm Co film patterned by RIPPLE by cycling from 0.4 V to and from 1.3 V at 100 mV/s in 0.1 M H_2SO_4 and 0.5 M KCl. (d) AFM height map for a pattern in (c). 34

Figure 2.4. Roughness of different substrates as determined from AFM. (a) AFM height map of Si wafer. Surface roughness R_{RMS} value of 350 pm. (b) AFM height map of FTO-coated glass. Surface roughness R_{RMS} value of 6.4 nm. 35

Figure 2.5. A patterned film on FTO-coated glass. (a) FTO coated with 250 nm Co and PMMA resist, after patterning. Transparent section at bottom is where the sample was exposed to 0.1 M K_2SO_4 during a cycle from 0.4 V to and from 1.3 V at 100 mV/s. (b) SEM image (SE2 detector) of patterns on sample in (a). Patterns are located at arrays of holes in resist. 36

Figure 2.6. 120 C/cm^2 Co electroplated onto FTO. (a) SEM image of the film's structure. (b) SEM image of the edge of electroplated Co metal film (120 C/cm^2) delaminating from underlying FTO. (c) Magnification of blue box in (b). 37

Figure 2.7. RIPPLE pattern in electroplated Co. Patterns generated by cyclic voltammetry, with five cycles from 0.4 V to and from 1.3 V at 100 mV/s in 0.1 M K_2SO_4. SEM image (grey) and EDS maps for cobalt (green), oxygen (red), and silicon (blue). 37

Figure 2.8. FIB cross section of a RIPPLE pattern in electroplated Co. From top to bottom: SEM image (grey) and EDS maps for cobalt (green), oxygen (red), and silicon (blue). First ring from center is on left; second ring from center is on right. 38

Figure 2.9. Anodization of a Co RIPPLE pattern. (a) Current trace for Co patterned by RIPPLE held at 0.85 V (below OER but above the $Co^{3+/4+}$ couple). (b) EDS elemental maps of RIPPLE pattern after anodization for cobalt (green) and oxygen (red) (c) CV of Co patterned by RIPPLE after anodization, scan rate 0.1 V/s. Prewave at 0.8 V corresponds to $Co^{3+/4+}$ couple, while catalytic wave at left is indicative of OER. 39

Figure 2.10. OER over 10 hr using a Co sample patterned by RIPPLE. (a) Current trace for anodized Co sample held at 1.0 V in 0.1 M KP_i, pH 7. (b) O_2 evolved by 40

patterned Co-OEC as measured by a fluorescent probe (red) and O_2 calculated from charge passed assuming a quantitative Faradaic efficiency (black).

Figure 2.11. Patterns after 10 hrs electrolysis at 1.0 V in 0.1 M KP_i, pH 7. (a) SEM image of Co RIPPLE pattern, ET = 3 kV. (b) SEM image (ET = 14 kV, grey) and EDS maps for cobalt (green), oxygen (red), and silicon (blue). 41

Figure 2.12. H_2 plasma-enhanced reduction of a Ge pattern, (a) before and (b) after PECVD. SEM micrograph (grey) and EDS elemental maps for germanium (yellow), oxygen (red), and silicon (blue). 43

Figure 2.13. EDS spectrum for H_2 plasma-enhanced reduction of a Ge pattern, before (red) and after (blue) PECVD. Peaks correspond to O K-edge (K 0.53 keV), F K-edge (0.68 keV), Na K-edge (1.04 keV), Ge L-edge (1.19 keV), Al K-edge (1.49 keV), and Si K-edge (1.74 keV). 44

Figure 2.14. H_2 plasma-enhanced reduction of a Co pattern, (a) before and (b) after PECVD. SEM micrograph (grey) and EDS elemental maps for cobalt (green), oxygen (red), and silicon (blue). 45

Figure 2.15. EDS spectrum for H_2 plasma-enhanced reduction of a Co pattern, before (red) and after (blue) PECVD. Peaks correspond to O K-edge (K 0.53 keV), F K-edge (0.68 keV), Co K-edge (0.78 keV), Al K-edge (1.49 keV), and Si K-edge (1.74 keV). 46

Figure 2.16. Pourbaix diagram for Co in water, 25 °C. Not all species considered. Colors denote theoretical conditions for metallic Co (green), corrosion (red), and passive oxide formation (blue). Arrows represent equilibria shifting as $[Co^{2+}]$ increases from 10 nM to 1 M. Dashed lines mark H_2/H^+ equilibrium (bottom) and H_2O/O_2 (top). Data from Reference 9. 48

Figure 2.17. Pourbaix diagram for Ni in water, 25 °C. Not all species considered. Colors indicate theoretical conditions for metallic Ni (green), corrosion (red), and passive oxide formation (blue). Dark red region is probable experimental conditions of corrosion in solutions not containing chloride. Arrows represent equilibria shifting as $[Ni^{2+}]$ increases from 10 nm to 1 M. Dashed lines mark H_2/H^+ equilibrium (bottom) and H_2O/O_2 (top). Data from Reference 9. 50

Figure 2.18 The effect of increasing the concentration of chloride for Ni in 0.5 M H_2SO_4 with no chloride (black), 0.1% NaCl (red), 0.5% NaCl (blue), and 3.5% NaCl (green). Data from Reference 10. 51

Figure 3.1. (top) Potential–time view and (bottom) corresponding current-time view of a binary-potential step method for patterning cobalt in 0.1 M K_2SO_4. 64

Figure 3.2. Patterns formed in a Co film by alternating between 0.4 V (10 s) and 1.3 V (3 s) 10 times in 0.1 M K_2SO_4. (a) Optical microscope images at 50× magnification. (b) SEM image (top left) and EDS elemental maps of cobalt (green), oxygen (red), and silicon (blue). (c) AFM map with height-profile of a diametric cross section (inset on right). 65

Figure 3.3. Dependence of Co pattern geometry on potential duration for five applications of the two-potential sequence, 0.4 V and 1.3 V, followed by one application of 0.4 V. To determine the effect of the duration of 0.4 V, 1.3 V was held for 3 s for each application and 0.4 V was held for the specified time indicated over each image (horizontal row). Similarly, 0.4 V was held at 10 s each application and 1.3 V was held for the time identified at the left of each image (vertical column). The center image shows both potentials held for 3 s. Samples imaged at 50× magnification. 66

Figure 3.4. Patterns in Co with conserved radial dimensions formed by sequentially increasing potential step durations in 0.1 M K_2SO_4. Images from (a) optical microscope with 50× objective and (b) SEM. 67

Figure 3.5. Evolution of the same Co pattern generated by alternating between 0.4 V (10 s) and 1.3 V (3 s) ten times (graphically described by Figure S1). (a) After 10 s, (b) 13 s (c) 23 s, and (d) the final pattern (75 s). Red dashed-circle corresponds to the etch front after applying 0.4 V for 10 s. Sample imaged at 63× magnification using water immersion objective. 68

Figure 3.6. Patterns formed in a Ge film by altering between 0.4 V and 1.1 V in 0.1 M K_2SO_4. (a) SEM micrograph of a pattern after five repetitions of the sequence 0.4 V (20 s) followed by 1.1 V (20 s). (b) EDS map for O of (a). (c) SEM micrograph of a pattern after five repetitions of the sequence 1.1 V (20 s) followed by 0.4 V (20 s) (reverse of (a)). (d) EDS map for O of (c). 69

Figure 3.7. Dependence of Ge pattern geometry on potential duration for five 70

applications of the two-potential sequence, 1.1 V and 0.4 V, followed by one application of 1.1 V. To determine the effect of the duration of 0.4 V, 1.1 V was held for 20 s for each application and 0.4 V was held for the specified time indicated over each image (horizontal row). Similarly, 0.4 V was held at 20 s each application and 1.1 V was held for the time identified at the left of each image (vertical column). The center image shows both potentials held for 30 s. Samples imaged at 50× magnification.

Figure 3.8. Application of (a) 0.2 V, (b) 0.3 V, and (c) 0.4 V for 10 s. Red dashed-circle corresponds to the etch front after applying 0.4 V for 10 s. Sample imaged at 50× magnification. 71

Figure 3.9. Applying 0.4 V over 30 s, followed by 1.3 V over 20 s successively (left column) and after a 30 min delay at open circuit (right column). SEM images (grey) and EDS maps for cobalt (blue), oxygen (red), and silicon (green). 72

Figure 3.10. (a) A schematic showing the diffusion from the etching front to the bulk electrolyte. Arrows schematically indicate the diffusion flux of Co^{2+}. Cross section is axisymmetric around the dash-dotted line. (b) Finite element simulation for the steady state concentration distribution of Co^{2+} (—), SO_4^{2-} (—), and K^+ (—) under the resist. Dashed black line marked the edge of the opening. 73

Figure 3.11. Predicted ring spacing from finite-element simulations. Ring positions (blue) relative to a 1 μm-diameter circular opening (black). Note ring spacing decreases with increasing distance from the opening. 74

Figure 3.12. Pourbaix diagram for Ge in water, 25 °C. Not all species considered. Colors indicate theoretical conditions for metallic Ge (green), corrosion (red), and passive oxide formation (blue). Arrow represents equilibrium shifting as $[HGeO_3^-]$ increases from 0.1 mM to 1 M. Dashed lines mark H_2/H^+ equilibrium (bottom) and H_2O/O_2 (top). Data from Reference 2. 78

Figure 4.1. Optical micrographs of patterns formed under 950 PMMA C4 spin-coated at 4000 rpm. Patterns were generated by alternating between 0.4 V (10 s steps) and 1.3 V (3 s steps) 25 times in 0.1 M K_2SO_4. Note, rings become less defined and coalesce as the pattern moves further from the opening in the resist. 91

Figure 4.2. (a) AFM height data of 950 PMMA C4 spun at 4000 rpm after cycling between 0.4 V and 1.3 V. Unsymmetrical increase in surface height in respect to the opening in the resist is an artifact caused by scanning parallel to the x-axis. (b) Composite of image in panel (a) overlaid on an AFM height map of a pattern (mapped without solution or resist) generated on the same sample. 93

Figure 4.3. Patterns formed by applying 0.4 V (3 s) followed by 1.3 V (3 s) ten times in 0.1 M K_2SO_4. Resist type (S1800 series photoresist or PMMA e-beam resist) denoted at top left. Film thickness at top right. Optical microscope 50× objective. 94

Figure 4.4. Patterns beneath resists examined by solution AFM. (a) S1805 spin-coated at 7000, (b) S1805 spin-coated at 2000 rpm, (c) S1818 spin-coated at 3000 rpm and (d) 950 PMMA C4 spin-coated at 4000 rpm. The electrochemical methods to generate the patterns are as follows: application of 0.4 V (3 s steps) followed by 1.3 V (3 s steps) 4 times for patterns in panels (a) and (b), 10 times for patterns in (c) and (d). Black dashed circles are 20 μm in diameter. 95

Figure 4.5. AFM height maps of select resist surfaces after patterning. (a) S1805 spin-coated at 7000 (280 nm), (b) S1805 spin-coated at 2000 rpm (480 nm), (c) S1818 spin-coated at 3000 rpm (2100 nm), and (d) 950 PMMA C4 spin-coated at 4000 rpm (740 nm). Unsymmetrical increase in surface height in respect to the opening in the resist is an artifact caused by scanning in the x-direction. (a) and (b) exhibit tears near the opening caused by the AFM tip. 96

Figure 4.6. Patterning by a lithography-free approach using lacquer beads as a mask. (a) Lacquer-water emulsion. (b) Beads of lacquer drop-casted onto cobalt. (c) Patterns formed under lacquer beads by applying 3 s steps of 0.4 V followed by 1.3 V 15 times in 0.1 M K_2SO_4. (d) AFM height map of a pattern formed by the procedure used in (c). 97

Figure 5.1. (a) Schematic of system used for patterning using an electrochemically generated gas bubbles. A moving boundary is defined as metal is etched from under the bubble. (b) and (c) Optical micrographs of rings made after applying 1-s step potentials of 0.4 V and 1.3 V. 20× magnification. 106

Figure 5.2. Patterning at the solution-air interface. (a) A samples patterned using the lacquer emulsion method in Part 4. Round pattern in center is due to a lacquer 107

bead. (b) Toward the upper limit of patterning in the sample shown in (a). Pattern gradually becomes less defined. 20× magnification. 107

Figure 5.3. Schematic illustrating operation of dip coater as utilized for electrochemically patterning oxide over the surface of a substrate. 108

Figure 5.4. Co-coated FTO (a) before and (b) after being electrochemically patterned using immersion to generate a moving boundary. Optical micrographs (20×) of the patterned surface (c) at the center and (d) at the edge of the sample. 108

Figure 5.5. Ridges on patterned sample from Figure 5.3. (a) SEM of oxide ridges (grey), with corresponding EDS elemental maps for Co (green), O (red), and Sn (blue). (b) Linear addition of elemental EDS maps shown in (a). 109

Figure 5.6. SEM micrograph from Figure 5.4 magnified 2.25 to show local ridge distribution. (a) SEM of oxide ridges (grey), with corresponding EDS elemental maps for Co (green), O (red), and Sn (blue). (b) Linear addition of elemental EDS maps shown in (a). 110

Figure 5.7. Integrating sphere (a) transmittance and (b) reflectance spectra for Co-OEC on FTO and patterned electrochemically Co on FTO. FTO (—), 30 mC/cm^2 CoPi (—), 150 mC/cm^2 CoPi (—), 250 mC/cm^2 CoPi (—), 400 mC/cm^2 CoPi (—), and patterned sample (—) after anodization in KP$_i$ at 1 V (30 min). 111

Figure 5.8. Current-time profile for 30 mC/cm^2 Co-OEC (—) and the patterned sample above (—) held at 1.0 V in KP$_i$, pH 7. 112

Figure 5.9. Potential-time traces for patterning a Co-coated (100 nm) FTO using a binary-potential step method coupled with immersion (10 μm/s). (a) Applied voltage steps of 0.4 V and 1.3 V vs. Ag/AgCl. (b) OCP-time trace vs. Pt counter electrode resulting from the potential-time trace in (a). 113

Figure 5.10. Circuit diagram for a device for patterning using the triple-phase interface method. Potentiometers govern wave height (right), pulse width (top left), and amplitude (bottom left). Square wave circuit design elements adapted from Reference 16. Electrical output tested in circuit simulator. 119

Figure 6.1. (a) Schematic of four-electrode configuration. The first electrode (E1) 127

is 1 cm^2 FTO loaded with 30 mC CoP_i. The second electrode (E2) is 1 cm^2 FTO. E2 is held at 0.85 in both experiments. Electrolysis proceeds for 72 hr. (b) OER currents for E1 and E2. For the experiment where E1 is poised at 1 V: E1 before electrolysis (—), E1 after electrolysis (—), E2 after collection (—). For the experiment where E1 is at open circuit potential: E1 before electrolysis (—), E1 after electrolysis (—), and E2 after collection (—). FTO (dashed —) represents E2 before.

Figure 6.2. Fabrication of CoP_i micro-discs on FTO: 1. Resist is spin-coated over film. 2. Holes (50 μm dia) are made in the resist using lithography. 3. CoP_i is electrochemically deposited into holes in resist. 4. Resist is stripped off. (*bottom left inset*) Optical micrograph of CoP_i micro-disc. 128

Figure 6.3. Circle of 150 mC/cm^2 CoP_i on 1 cm^2 square section of FTO before (left column) and after, 24 hr electrolysis at 1 V in KP_i buffer (pH 7) without (center column) and with (right column) stirring 24 hr. Rows correspond to SEM (grey), Co (cyan), P (yellow), O (green), and Sn (magenta). 129

Figure 6.4. CVs at various [Co^{2+}] and pHs. [Co^{2+}]: 0 mM (—), 1 mM (—), 10 mM (—) and 100 mM (—). (a) pH 2.5, (b) pH 3.0, (c) pH 3.5, (d) pH 4.0, (e) pH 4.5, (f) pH 5.0, and (g) pH 5.5. 130

Figure 6.5. Pourbaix diagram for 1 mM Co^{2+}. E corresponds to a current density of 5 mA/cm^2. The blue line is a linear fit for pH 2.5–4 and has a slope of –118 mV/pH. 131

Figure 6.6. Expanded views of micro-prewaves for 1 mM Co^{2+}. pHs: 5.5 (—), 5.0 (—), 10 mM (—) and 100 mM (—).100 mM (—).100 mM (—).100 mM (—). (a) Enlarged current scale of pH composite from Figure 6.4 showing micro-prewave (10 μA/cm^2) (b) Forward scans of micro-prewaves shifted by 120pH V to highlight pH dependence. Current and potential scales reversed for clarity of increase. Note prewave (—) rising at left of catalytic waves. 132

Figure 6.7. Expanded view of Figure 6.3c (pH 3.5) illustrating Co dependence of micro-prewave. [Co^{2+}]: 0 mM (—), 1 mM (—), 10 mM (—). 132

Figure 6.8. Bulk electrolysis with FTO electrode at 1.3 V, KP_i (pH 2.5), 1 mM Co^{2+}. 133

Figure 6.9. (a) Current profile for a 100mC/cm^2 CoP_i film immersed in 0.1 M H_3PO_4 while operating at 1.8 V. Cell volumes compared are 4 mL (—) and 40 mL (—). FTO without CoP_i operating at identical conditions in a 40 mL cell is provided for reference (—). (b) An expanded view of steady state currents observed in (a). No stirring was used. Cells contain two identical compartments separated by a frit. 134

Figure 6.10. O_2 probe data for 250mC/cm^2 CoP_i film immersed in 8 mL 0.1 M H_3PO_4 while operating at 1.8 V. Measured O_2 (—) and theoretical O_2 calculated from charge passed (—). 136

Figure 6.11. Tafel plot for 0.2 M Fe(III)$(NO_3)_3$ (pH 3) with iR subtraction from η (●) and without iR compensation (●). Lines fit to uncompensated data from $10^{-6.8}$–$10^{-4.1}$ A (–) and $10^{-4.1}$–$10^{-3.2}$ A (–) exhibit Tafel slopes of 56 mV/dec and 325 mV/dec. Overpotential scale calculated for OER in pH 3 and referenced to NHE. 137

Figure 6.12. Current trace of 0.2 M $Fe(NO_3)_3$ at 2.0 V, corresponding to upper limit of Tafel plot in Figure 6.11. 138

Figure 6.13. Tafel plot for 0.2 M $Fe(H_3C_2O_2)_3$ (pH 3) without stirring and withough iR compensation (●), with stirring and iR compensated for measured resistance (R_{FTO}+$R_{solution}$)(●) and compensated only for FTO (R_{FTO} ~20 Ω) (●). Linear fit for iR uncompensated data from $10^{-3.4}$–$10^{-1.5}$ A (–) exhibits a Tafel slopes of 26 mV/dec. FTO (○) and IrOx (○) data for reference. IrOx data acquired in pH 1 and corrected for pH 3 assuming 60 mV/pH Nerstian shift. Overpotential scale calculated for OER in pH 3 and referenced to NHE. IrOx data from Reference 9. 139

Figure 6.14. CV for 0.2 M $Fe(H_3C_2O_2)_3$ at 10 V/s. iR compensation set to 0 Ω (—), 10 Ω (—), 20 Ω (—), 30 Ω (—), 40 Ω (—), and 41 Ω (—). Note: solution resistance varies with each setup. 140

Figure 6.15. OER faradaic efficiency measurements for 0.2 M $Fe(H_3C_2O_2)_3$ at high current densities. (a) O_2 evolved at 1.75 V as measured by fluorescent probe 1.75 V (—)and O_2 evolved assuming 100% Faradaic efficiency of charge passed (—). (b) Faradaic efficiency measured by gas chromatography. 141

Figure 6.16. *In situ* UV-Vis spectrum for dilute (~0.01 M) $Fe(H_3C_2O_2)_3$ in 0.1 M HNO_3 operating at 1.8 V. Spectra normalized to 700 nm (not shown). Note shoulder at 275–320 nm and feature at 520–560 nm characteristic of FeO_4^{2-}. 142

Figure 6.17. Mechanism for CoP_i adapted from Reference 17 with additional pathways A, B, and C. 145

Figure 6.18. Pourbaix diagram for a CoPi film operating at 30 μA, illustrating third and first order proton dependence for deposition (●) and OER (●), respectively. Note the predicted crossover region at pH 5.5, where the red line for OER crosses the green line extrapolated for deposition. Data from References 18 and 22. 147

Figure 6.19. Pourbaix diagram for Fe in water, 25 °C. Colors indicate theoretical conditions for solid Fe (green) and soluble (red). FeO_4^{2-}, a species of interest for OER catalysts, is labeled in yellow. Arrow represents equilibrium shifting as $[Fe^{3+}]$ increases from 0.1 mM to 1 M. Dashed lines mark H_2/H^+ equilibrium (bottom) and H_2O/O_2 (top). Data from Reference 21. 154

Figure 6.20. (a) Tetrahedral structure of ferrate. (b) Bi-ferrate structure formed under acidic conditions. 155

LIST OF TABLES

Table 1.1. Metal oxide oxygen evolving catalysts studied in our group. Lower Tafel slopes indicate catalysts that respond with more activity per overpotential in the activation-controlled regime. 12

Table 4.1. Resist thickness values from commercial datasheets and measured values. 34

Table 6.1. Co analysis for CoP_i distribution between the electrode and electrolyte at low pH. 134

Table 6.2. Commodity base and precious metal prices as of April 2018. Data from Reference 24. 153

Table 6.3. Solubility of various Fe(III) Salts. Data from Reference 39. 156

ACKNOWLEDGEMENTS

No discovery in the following print can compare to what the scientist before me has accomplished, with a fraction of the instrumentation and resources that are at my disposal. I nonetheless submit this thesis in tribute to my predecessors' progress, which has provided my niche in chemical research.

I am indebted to my graduate advisor, Professor Daniel Nocera, who has been the biggest external influence in my life's course. One of the most notable things about working in the Nocera Group is the liberty imparted to the researcher. Having such independence in experimentation allows the researcher to achieve confidence in his research habits that cannot be gained by any other means. Some perceive this style as a hands-off approach; however, to allow a graduate student to freely pursue his or her own curiosity requires a vast amount of resources and trust, both of which Dan provides liberally. It also requires the advisor to be extremely effective in his guidance. I will not attempt to prove Dan's effectiveness as an advisor; his reputation precedes him. I will affirm, however, that Dan's wit, intensity, and knowledge are unmatched. His true character is often obscured by his passion and personality. However, the astute will attest, Dan's intentions are as noble as they come. This body of work represents only a portion of what I learned while working under Dan's guidance. Thank you, Dan.

I also thank my thesis committee, Professor George Whitesides and Professor Yogi Surendranath, for their time and expertise during our meetings. Their advice has helped steer my research in rewarding directions. Thank you, both.

There are many people to whom I express the upmost appreciation for their support and teachings. I thank Ms. Erickson and Mr. Kohler for inspiring my interest in chemistry at Haslett High School. I thank Professor Kate Plass at Franklin & Marshall College for her guidance in inorganic chemistry and for introducing me to laboratory research. I also thank Professor Katie Ford for helping me hone my creativity, Professor Robert Battistini for encouraging my interest in chemistry despite my initial doubts, and President John Fry for taking my interest in artificial photosynthesis seriously.

I remember it like it was just a week ago that I met Kwabena Bediako on a rainy day on the steps of Lobby 7—thank you for mentoring me as an undergraduate and as a graduate student, and teaching me the art of electrochemistry. Also, thanks to Mike Huynh for serving as my unofficial secondary mentor. Between these two colleagues, I learned not only the majority of my electrochemical knowledge, but also how to conduct independent research. In addition, my experience working with Kwabena prepared me for mentoring my own undergraduate. There are many things that I could mention here, but all sentiments may be succinctly conveyed by a single word: Ready?

Thanks, also, to Dr. Dilek Dogutan for her investment in the group. She helps our group in more ways than I will ever know, and I can say with confidence that the scientific successes of the lab are the direct results of her efforts. Thank you, Dilek.

I worked with dozens of members from the Nocera Group as an undergraduate and graduate student. They all define my standard for what constitutes real intelligence. I often strived to imitate their mindsets, so they can be credited for my intellectual advancement during my PhD. I acknowledge the Nocera Group members from my earlier years in the group, for teaching me by example with their skills and intellect: my first office mate at Harvard, Manos Roumpelakis, whom I always enjoyed finding new local Greek restaurants with; Dan Graham, one of the funniest, most genuine people I have ever met; Christopher Gaglihardi, "the insult master!;" Bryce Anderson, my personal strength trainer; Christopher Lemon, thank you for the many dinners at Tanjore; Robert Halbach, you were missed in my last years in the group; Dave Powers; Andrew Maher; Lisa Olshansky; Yi Liu; Arturo Pizano; Andrew Ullman; Mike Marshak; Matt Chambers; Bon Jun Koo; and Cassandra Cox. A few senior members only overlapped with me for a summer or so at MIT during my undergraduate experience, but their impressions on me were nonetheless significant: Yogi Surendranath; Dino Villagrán; Tom Teets; Changhoon Lee; Bob McGuire; Joep Pijpers; and Elizabeth Karnas.

I would also like to acknowledge the recent and current members of the group. Charlie Margarit and I became friends right away, often expressing our thoughts and frustrations in a most civil manner from our respective offices and benches. I now consider Charlie one of my closest friends. Thank you for all the times you helped me out. I would say something else, but it would be highly inappropriate. Also thanks to Guillaume Passard, in Paris, and David Jaramillo, at Berkeley, for the many good times (and the occasional discussion on chemistry). Kagome! Thanks also to Nancy Li for working with me during all the lectures we taught and for cranking out problem sets like a beast. My many late-night discussions with Seung Jun Hwang were helpful motivators, as was observing his relentless work habits. The legend, Jeremy Warner of Oxford Medical School, kept me company in the cleanroom many a time and even helped with some of my experiments. I thoroughly enjoyed our conversations on literature, poetry, and philosophy. Ryan Murphy, now at Berkeley, was likewise a pleasure to converse with around the lab. Eric Bloch's spontaneity and intensity is an amazing thing to witness. He will make a great chemistry professor. Tom Kempa was another influential colleague in the lab; thank you for initiating my project and helping me with all the crazy instruments in Professor Lieber's lab. The chemical understanding possessed by Chong Liu, Tuncay Ozel, and Kelsey Sakimoto seems incomprehensible; thank you for the many discussions and offering your guidance. Xiaowen Feng and Brandon Greene also had expert advice to impart during my group meetings.

As I became a senior member in the group, I was privileged to continue meeting and working with incredible new colleagues and friends. Casey taught me to always take secondhand explanations with a grain of salt. There are countless times when I referenced some knowledge I was previously taught and she showed me data that contradicted the statement. Zamyla Chan has an engineering outlook that resulted in many nifty experimental setups. She was often at MIT to do specialized work there, but when she was around lab, she was always a positive force. David Gygi is a research animal and always a help in lab. I sincerely hope he does not get burned

out despite the enormous effort he puts into the group. I thank Zander (Flanders) Deetz and Ben Zhang for their friendship and frequently participating in our informal wine tasting evenings. I also thank Zander for being a chill office mate. Thanks to Joe Elias and Serge Ruccolo for being great friends and for the many lunches. The Harvard Cabin ski trip was a blast. I also thank Ben Martindale, Yangzhong Qin, and Matt Nava for making my final year in the group worth it

There are additional members who I did not get a chance to know very well, but their friendliness in lab is nonetheless appreciated: Mengran Liu; Billy Woodford; Ryan Hadt; Xizhu Zhao; Seung Woo Lee; and Noémie Elgrishi.

I thank Karen Nocera for hosting the lab at Dan's and her home for the annual summer BBQ's and Christmas parties and also for being one of the kindest people I have ever met.

The administrators that helped out our group were imperative in the operations of GACs and other meetings. They include Allison Kelsey, Lisa Lubarr, Carolyn Moore, and Lindsey Shepard. Thank you for making the most elusive individuals in the world accessible.

I thank my collaborators, Professor Zhigang Suo and Qihan Liu, for their phenomenal work in finite element simulations and teaching me about scaling analyses.

I had the privilege of working with Roger Jin, an undergraduate at Harvard. Over the summer, Roger showed dedication and commitment to research equal to that of any graduate student. When I encountered a problem, I could explain the issues to Roger and he would unfailingly procure a thoughtful idea. He was a pleasure to work beside.

Some other people I would like to mention who enriched my graduate experience: the amazing staff at CNS, particularly Professor David Bell, Ed Macomber, Phillip de Rouffignac, Jules Gardener, Adam Graham, Andrew Magyar, and Jason Tresback; Ed Mitchell for skillfully crafting our glassware; all of the administrators and staff who served in the chemistry department, with special thanks to Allen Alloise, Elizabeth Lennox, Kathy Oakley, Barbara Anderson, Mike Paterno, John Randazzo, Chris Perry, and the many individuals who work behind the scenes here. I also would like to mention Professor Kate Konschnik, Professor Ted Betley, Professor Ted Sichelman, Professor Michael Meurer, Professor Peter Murray, Professor Roald Hoffman, the Harvard evening van drivers, especially Jack and Bob, and our lab's warm custodian, Jose. Also thank you to Dean and Joy Velozo, Felipe Herrera and Tom Brush, and Mark and his wife at P&K, for providing 90% of my sustenance. Many of the individuals mentioned here went above professional interactions with me and some would even oblige me to a lunch every now and then.

I thank Joey Aldrich, Louis (Bill) Eisenbrenner, Tim Jewell, Jason Seitcheik, and Christian Zinkhan for their enduring friendship and the hilarious memories. You are still missed, Tim. I also thank Jared Cohn and Jason Seitchik for their friendship and their efforts in literally teaching me the fundamentals of chemistry.

Also acknowledged are the Harvard College Men's Club Ice Hockey team and the Harvard Business School Rugby Football Club. I made many friends in both organizations, and I

had a lot of fun competing along their side. In a weird way, hockey seemed to go full-circle, since I am not certain that I would have ended up here if it were not for youth hockey.

My parents have always been my biggest supporters. They have been there every step, helping me become better and offering their guidance and patience. What they have done for me goes far beyond whatever duty parents have in raising their son. It is incredible. Thank you, Mom and Dad. *This thesis is dedicated to you.*

My brother, Andrew, is currently engrossed in medical school. I am excited, yet awed, to see him becoming a doctor. I feel like we were exploring the backyard together just the other day. I would not be the person I am without our frequent and creative interactions as youths. I thank him for his friendship while we were growing up.

My grandmother always showed interest and support in my accomplishments. Up until her final days, she managed to keep up with the events in my life, despite being very ill. I thank her for her constant investment and love. I couldn't have asked for a more thoughtful grandmother. I admire the strength, resilience, and passion that she demonstrated in her life. Although she just barely missed my graduation, I am thankful that she was able to see me grow along the way, and I believe she found gratification in witnessing just that.

I am proud to say my grandfather, Professor Robert Kouyoumjian, belonged to the first group of people mentioned here: the great scientists before me. I am only beginning to appreciate his work in wave diffraction theory, which proved revolutionary in the field of electrical engineering. Despite his great achievements as a scientist, I remember him for possessing the most attentive, humble attitude. His work is beyond comparison of what I could achieve in a thesis, but I often entertain the idea that our scientific interests were both tied to electrical phenomena. Thank you for inspiring my earliest curiosities in science, and being a loving grandfather in general.

During some of the most challenging moments in my research experience, Ariana Bratt provided her love, support, and advice. She is one of the hardest working persons I have ever met. Thank you, Ariana, for your faithfulness and companionship. I also thank Susan Snow and Rick Bratt for their hospitality and kindness.

I am grateful for financial assistance from the National Science Foundation for a research fellowship. I also acknowledge the NSF CCI Solar Fuels initiative for financial assistance.

Finally, I am thankful, yet skeptical, of my improbable path thus far. I can say with certainty that in the last six years, I have met incredible individuals and worked with extraordinary technologies. I have also gained humility and maturity. My future will benefit from every lesson, from the influence of a π-acceptor on a ligand field, to the importance of choosing battles; my perception and actions shall always account for these lessons.

I would like to acknowledge everyone who has contributed to this thesis in any way.
Thank you.

Part 1. Introduction

Portions of this chapter have been published:
Bediako, D. K.; Costentin, C.; Jones, E. C.; Nocera, D. G.; Savéant, J.-M. *J. Am. Chem. Soc.,* **2013,** *135,* 10492-10502.

1.1 Motivations for solar energy

The cumulative global effects of burning fossil fuels make a revolution in energy production one of the most urgent pursuits of our lifetime. Indeed, the ultimate applications of this project are with that goal in mind. While it is tempting to subscribe to any technological pursuit that advertises to curb CO_2 emissions, it is important to first understand the underlying problems so that valuable resources (i.e. time and money) are not rashly wasted.[1]

1.1.1 Fossil fuels and conventional energy production

The combustion of fossil fuels (natural gas, petroleum, and coal) presently accounts for 86% of the United States' energy production (1.9×10^{10} metric tons oil equivalent) and 86% (1.1×10^{11} metric tons oil equivalent) of global energy production.[2] To put this number in perspective, the current global consumption of energy in fossil fuels amounts to burning *the volume of Lake Erie* in crude oil every 5 years.[3] Fossil fuels represent a sink for carbon in the long-term carbon cycle, where carbon is exchanged between rocks, the ocean, the atmosphere, the biosphere, and soil on the order of millions of years.[4] Complete combustion of the fuel releases chemical energy as carbon and hydrogen are oxidized, which results in the emission of CO_2 and water according to Equation 1.

$$C_xH_y + \left(x + \frac{y}{4}\right) O_2 \rightarrow xCO_2 + \frac{y}{2} H_2O \qquad \text{(Eq 1.1)}$$

Modern atmospheric CO_2 concentration has thus increased since the beginning of mass fossil fuel utilization during the industrial revolution, as evidenced by nondispersive infrared spectroscopy of the atmosphere and analysis of bubbles in ice cores.[5] Global CO_2 levels have just exceeded 400 ppm in 2017 (Figure 1.1a), higher than in the last 600 millennia and likely higher than in

the past 20 million years. Fossil fuels and cement emissions are calculated to have had a cumulative output of 3.3×10^{11} metric tons of carbon between 1850 and 2006, with an additional 1.6×10^{11} metric tons resulting from deforestation. In all, anthropogenic CO_2 is estimated to constitute *30% of present-day atmospheric* CO_2.[6]

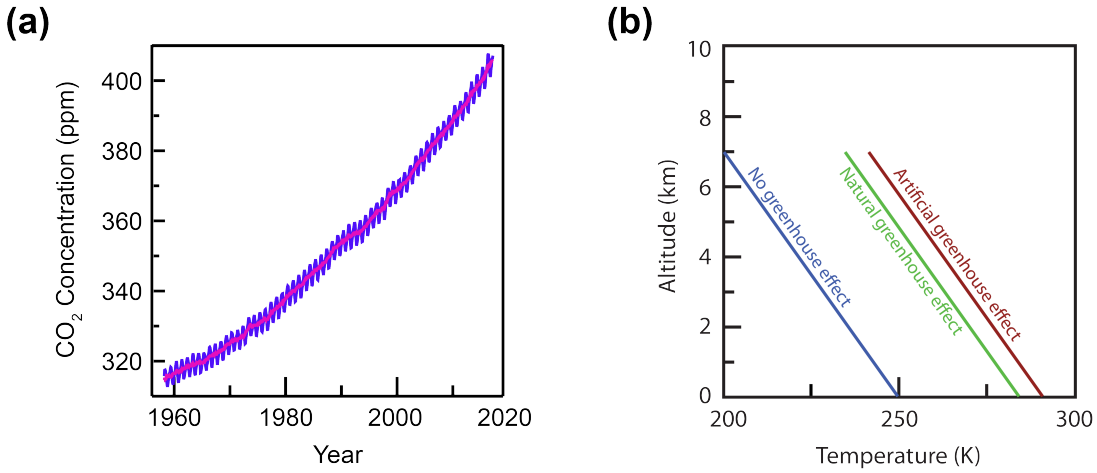


Figure 1.1. (a) Atmospheric CO_2 as measured from Mauna Loa Observatory, Hawaii (e.g. the Keeling Curve). Longest record of direct measurements of CO_2 (—) and seasonally corrected data (—). Data from Reference 5. (b) Model depicting greenhouse effect. Temperature without greenhouse gases (—), with natural greenhouse gases (—), and with anthropogenic CO_2 (—). Readapted from Reference 7.

Since CO_2 is passive towards short-wavelength solar radiation and absorbs long-wavelength IR radiation, such as heat radiating from Earth, CO_2 acts as a "greenhouse gas" and effectively elevates the altitude where outgoing IR radiation escapes Earth (Figure 1.1b).[7] Svante Arrhenius was the first to provide a rigorous calculation on how man-made CO_2 might influence the global climate.[8,9] Since then, more elaborate models have been developed to predict the influence of CO_2 on global temperatures, which predict changes from catastrophic sea level increases to changes in weather patterns.[10,11] Indeed, an increase in average temperatures as low as 0.8 C could trigger irreversible positive feedback loops.[11] Today, the hike in anthropogenic CO_2

has manifested as an extensive list of national climate-related problems and the warmest years on record.[12,13]

The CO_2 problem is intensified by predictions of a growing global population, which is expected to require a 100% increase in energy demand from 2000 to 2050.[14] The lower carbon intensity of gross world product (CO_2 emission required for a unit for global economic growth), coupled with rapidly increasing CO_2 emissions, exacerbates the spike of CO_2 in the atmosphere.[6] The CO_2 problem is thus a larger energy problem, particularly in the developing world, where soaring populations and want of technological capabilities and infrastructure drive down the carbon intensity of GDP. A logical answer is finding an affordable solution to primary energy production that can accommodate the developing world. Nuclear, wind, and biomass energy sources are not tenable replacements.[14] Across all measures, the Sun universally stands out as the best alternative energy source and the only single alternative source that can satisfy the global energy demand.[14]

1.1.2 Solar energy

The Sun is a main sequence star of spectral class G. At its core, protons are converted into He through proton-proton chain fusion.[15] Since the sum of four protons weighs less than a helium nucleus, 0.7% of the protons' mass is released as energy and shed as radiation, which in turn "powers" the star (Figure 2, left). The Sun converts 4.3×10^9 kg into energy every second, outputting 3.8×10^{14} TW.[16] Despite this enormous power, the Sun is estimated to maintain hydrostatic equilibrium for another 4.5×10^9 years.

As solar radiation emitted by the Sun travels through space, it diffuses. It is then absorbed and reflected by Earth's atmosphere (Figure 1.2, center). The energy density of sunlight

that reaches Earth's orbit is 1,367 W/m^2 and averages 200 W/m^2 at midlatitudes.[17] In total, the sun deposits 120,000 TW of radiation onto the Earth's surface, or 10,000 times the power that humans use today and, unlike conventional fossil fuel combustion, direct solar-to-electric technologies can generate primary energy without detrimental emissions. Given that this extraordinary energy is distributed across the planet, sunlight is the only scalable, stable, clean, and readily available alternative energy source to meet the forecasted energy demand of the next several decades.[14]

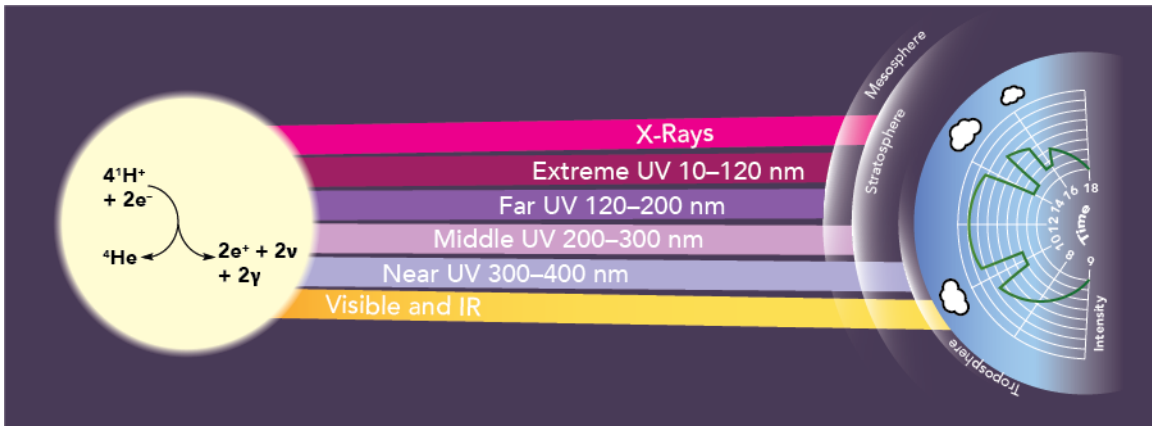


Figure. 1.2. The Sun is an ideal source of energy. Left: The Sun is depicted with sustained nuclear fusion occurring in its core. Center: Solar radiation diffuses through space and eventually reaches the Earth, where some is absorbed and reflected by the atmosphere. Readapted from Reference 18. Right: The daily availability of terrestrial solar energy on Earth's surface, showing relative intensity of sunlight representative for daily time course.

A challenge to solar energy dependence is that its carrier particle, the photon, cannot efficiently drive mechanical or electric appliances. (Photons have neither mass nor electric charge.) This presents the challenge of engineering a system that directly utilizes solar energy and thus requires a method to convert photons to electricity or heat.

Another disadvantage of solar energy is the flux of insolation. Insolation experiences diurnal variation, as well as annual variation due to Earth's axial tilt (Figure 1.2, right). The shade

of clouds can influence terrestrial solar radiation for spans ranging from minutes to weeks. If solar energy were to displace fossil fuel, a reliable storage system is necessary to provide constant energy during periods of little to no sunlight.

1.2 The components of a competitive solar energy system

While there are many components that go into constructing an operable solar energy system, it is useful to think of the complete system as two sub-systems: a mechanism for converting solar energy and a mechanism for storing the solar energy.

1.2.1 Converting solar energy

The photovoltaic effect represents the most direct conversion from sunlight into electricity. Sunlight (as photons) illuminates a semiconductor and electric energy is generated immediately. No additional steps are needed for the conversion.[19] The lack of additional steps makes photovoltaics (PVs) a promising mode of harnessing solar energy. Conventional solar cells are fabricated from Si, one of the most common elements on Earth. A depletion layer is formed at the junction between p-type and n-type Si, which in turn creates an electric field. The electric field separates hole-electron pairs that are formed when electrons are excited by sunlight, and this results in electricity.

1.2.2 Cheap PVs are not enough

Solar electricity is still extremely expensive, and therefore not yet competitive with electricity generated from fossil fuel.[17,20] For PV systems to become competitive, the levelized cost of

electricity from a PV must achieve grid parity.[21] As Figure 1.3 illustrates, the success of a practical solar energy system is dependent on both the cost of the PV module, as well as the cost of storage.

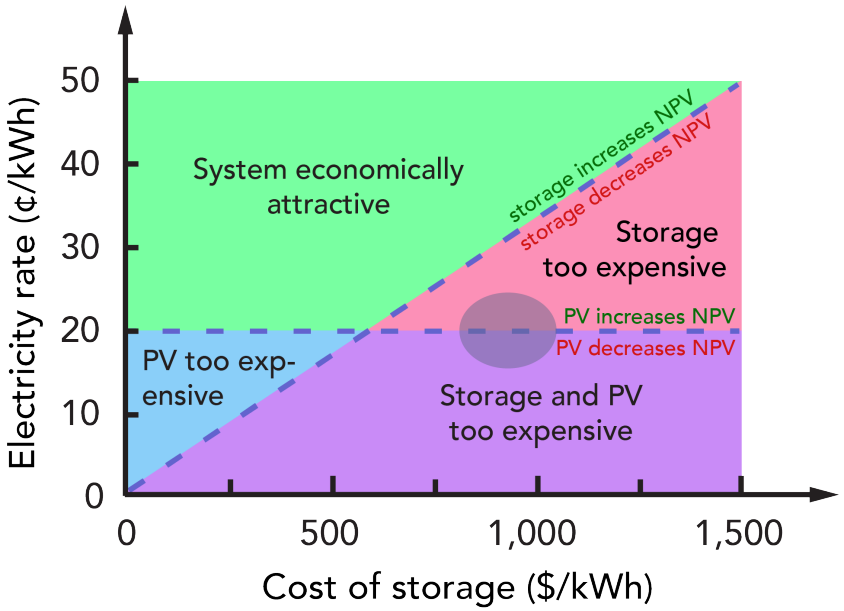


Figure 1.3. Economic viability of a solar energy system for a homeowner. Plot assumes California household with a 10 MWh demand, a 4 kW PV array, a 4 kWh battery, and flat retail rates. Prices as of December 2015 shown as gray oval. Rooftop PV modules only add net present value (NPV) to a home if electricity retail rates increase, or the cost of PV or storage systems decrease. Readapted from Reference 21.

Installing a PV system can cost three times that of the battery system.[21] However, as Figure 1.3 illustrates, the cost of electricity from a PV system is competitive with electricity retail rates, while the cost of storage decreases the net present value of the total system. Therefore, the cost for the storage system also limits the competitiveness of a solar energy system. This problem also presents the opportunity to make a more competitive solar energy system by lowering the cost of the storage system. There are three key qualities identified as necessary for a cost-

effective storage system: efficiency, robustness, and scalability.[22] All three of these factors will influence the levelized cost of solar electricity.

1.2.3 Using the oxidation of water to store energy

As an abundant material on Earth, water is an ideal material to incorporate into a storage system. Water-splitting is the electrolysis of water into its constituent elements, oxygen and hydrogen (Eq 1.2). Water-splitting can also describe the oxidative half reaction of water to yield protons, but for now we will assume that hydrogen is evolved, following the equation:

$$H_2O \rightarrow \frac{1}{2}O_2 + H_2 \qquad E^0 = 1.23\ V - 59mV\ pH \qquad \text{(Eq 1.2)}$$

The free enthalpy for Eq. 1.2 necessitates a minimum input of 1.23 V. The products thus store 1.23 V of usable energy per charge, regardless of how much energy is used to drive the reaction. The stored energy can be recovered by either performing the reverse reaction in a conventional hydrogen fuel cell or by burning H_2 directly.

The ubiquity of water makes water-splitting an attractive mechanism of storing energy. In addition, hydrogen has the highest specific energy of known fuels and a low viscosity, making it easy to transport in pipes. This led scientists some decades ago to the idea of an entire hydrogen economy infrastructure.[23] However, hydrogen gas has a very low volumetric energy density. It also leaks rapidly due to its low viscosity, causes embrittlement of metals, and forms explosive mixtures with O_2. Recent bioengineered systems have demonstrated the ability to produce liquid fuel such as isopropanol from solar generated hydrogen, thereby translating the stored energy of hydrogen into a liquid fuel with a larger energy density.[24,25] If this strategy of fuel production is to succeed at appreciably lowering global CO_2 emissions, we bear in mind that the overall

system (including energy recovery) must meet grid parity and be accessible to developing countries. Efficiency and cost (which are in many ways intertwined) will therefore be critical aspects of a successful water-splitting storage system.

1.2.4 Overpotential

The efficiency of an electrochemical system is often interpreted from the required overpotential for a specific reaction. The overpotential, η, is the difference between the applied potential, E, and the reversible potential, E^0.[26]

$$\eta = E - E^0 \qquad \text{(Eq 1.3)}$$

A goal in engineering a competitive solar energy system is for the applied potential of the storage process to approach E^0. In fact, if we want to enhance the efficiency of an electrochemical system, the only parameter we can influence is the overpotential. There are different types of overpotentials for a given electrochemical process, which all limit the reaction rate.[26] The activation overpotential, η_{ac}, is the kinetic quantity that acts on the electrochemical energy of activation. The activation overpotential is the desired parameter in electrokinetic studies. The resistance overpotential, η_{jR}, is the ohmic drop in potential due to resistance of electron flow through a material. Finally, the concentration overpotential, η_{conc}, is the mass-transport limitation. This overpotential compensates for the gradient of species near an electrode's surface. The observed overpotential for an electrochemical system is the sum of these overpotentials.

$$\eta = \eta_{ac} + \eta_{jR} + \eta_{conc} \qquad \text{(Eq 1.3)}$$

Returning to the concept of storing energy by splitting water, the overall overpotential will include the activation overpotentials for the reactions at both the anode and the cathode. The anodic and cathodic half reactions of water-splitting are shown, respectively:

$$2H_2O \rightarrow O_2 + 4H^+ + 4e^- \qquad E^0 = 1.23\,V - 59mV\,pH \qquad \text{(Eq 1.3)}$$

$$2H^+ + 2e^- \rightarrow H_2 \qquad E^0 = 0\,V - 59mV\,pH \qquad \text{(Eq 1.4)}$$

Note that Eq 1.3, coined the oxygen evolution reaction (OER), involves four protons and four electrons for every oxygen molecule generated. This complex transfer of charged species results in a high kinetic barrier, and hence larger activation overpotential than the cathodic half-reaction, or hydrogen evolution reaction (HER).[27] In order to overcome the kinetic barriers of OER, proton coupled electron transfer (PCET) must be accommodated by a mechanism that stores charge and discharges it cumulatively.[28,29] Towards these ends, our group has investigated OER catalysts.

1.2.5 Hydrous metal oxide films for OER

Co-, Ni-, and Mn-based oxygen-evolving catalysts (Co-OEC, Ni-OEC, and Mn-OER, respectively) can abate the kinetic penalty (overpotential) of the four-electron, four-proton water oxidation reaction.[30–32] Films of the catalysts self-assemble onto an electrode from buffer solutions (phosphate (P_i) or borate (B_i), depending on the metal) containing low concentrations of the respective metal ion. The catalysts are composed of Earth abundant materials and operate under acidic (pH 3, specifically Mn-OEC)[32] or neutral (pH 7-9) conditions at near 100% Faradaic efficiency. Catalyst films can self-heal, thereby maintaining stable activity over extended intervals.[31,33,34]

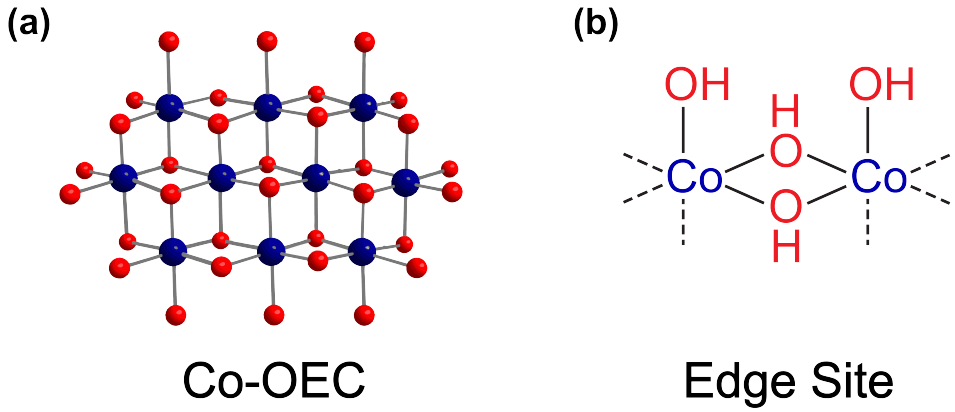


Figure 1.4. Co-OEC, a hydrous metal oxide catalyst for the OER half-reaction. (a) Structure of catalyst as determined from XAS with octahedral Co (blue spheres) bound to bridging O (red spheres). (b) Edge sites are the proposed active sites of Co-OEC. Mn-OEC and Ni-OEC are proposed to have analogous bulk structures and bridging-oxo active sites.[35,36] Reprinted with permission from Casey Brodsky.[37]

Extensive analysis has been performed in order to identify the catalysts' active sites and structures. The Co-OEC, for instance, has been identified as a mixed $Co^{(III)}$-$Co^{(IV)}$ species, as determined by electron spin resonance (EPR). X-ray absorption spectroscopy (XAS) and X-ray absorption fine structure spectroscopy (EXFAS) indicate clusters containing rows of repeating units of CoO_2 that are staggered every column, resulting in a three-dimensional dice lattice (Figure 1.4).[38]

Since the metal redox couple responsible for the electrochemical formation (deposition) of the catalyst occurs at a potential less oxidizing than catalysis of OER, the loading of catalyst on the electrode (and to some extent, the film thickness) can be modulated by controlling the charge at potentials below OER. The number of active sites scale with the amount of metal oxide deposited on the electrode, and therefore, the activity of a film of catalyst is dependent on the deposition procedure. This is also due to the films being porous, allowing water to permeate the catalyst.[38,39]

The activity of an electrochemical catalyst can be described by its Tafel plot (log of current density as a function of overpotential). The two electrokinetic parameters that determine a Tafel plot are the Tafel slope and the exchange current density (the extrapolated current at no overpotential). The Tafel slope is determined by the electrochemical mechanism, while the exchange current density depends on the number of active sites, as well as intrinsic properties of the catalyst, such as conductivity (η_{jR}). Since the exchange current density depends on the deposition procedure, the Tafel slope is a useful benchmark for how catalysts respond to potentials in the activation limited region, where catalysis is not limited by mass transport. Table 1.1 catalogs the Tafel slopes of our metal oxide OECs, which are among the most active OECs known.

Table 1.1. Metal oxide oxygen evolving catalysts studied in our group. Lower Tafel slopes indicate catalysts that respond with more activity per overpotential in the activation-controlled regime.

OER catalyst	Deposition buffer	OER conditions	Tafel slope (mV/decade)	Reference
Mn oxide	None	P_i, pH 7	120	40
Mn oxide*	None	P_i, pH 7	70	40
Mn oxide	None	P_i, pH 2.5	650	40
Mn oxide*	None	P_i, pH 2.5	90	40
Co oxide	P_i	P_i, pH 7	59	38
Co oxide	P_i	B_i, pH 9.2	52	41
Ni oxide	B_i	B_i, pH 9.2	120	31
Ni oxide*	B_i	B_i, pH 9.2	29	36

*preconditioned
P_i: phosphate buffer
B_i: borate buffer

These metal oxide catalysts satisfy the three requirements—efficiency, stability, and scalability—needed for a competitive solar storage system. As such, catalytic water-splitting offers a realistic strategy for storing solar energy. With a practical storage component in hand, we

turn our attention to realizing a complete system that could expedite the transition from fossil fuel dependency to solar energy.

1.3 Integrated water-splitting devices

The PV component of a solar energy system can be coated with an OER catalyst to form an integrated photoelectrochemical cell (PEC). Our group has demonstrated this by coating PVs with metal oxide catalysts with the aim of constructing an integrated solar system that could be distributed to the nonlegecay world. The success of this effort is contingent on designing a device that can be cheaply mass-produced. The general principle behind the design is a layered architecture, where each layer has a function in the process of storing energy from sunlight in the

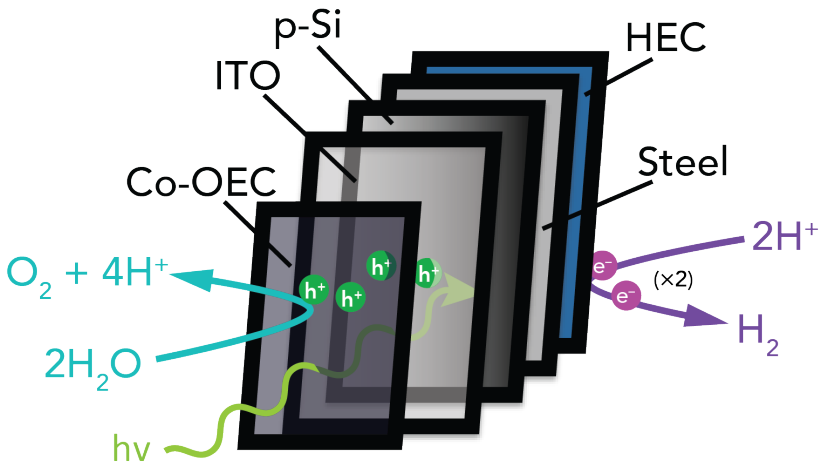


Figure 1.5. Schematic of an integrated, wireless solar water-splitting device.[42] The hydrogen evolving catalyst (HEC) can be NiMoZn or CoP.[25]

chemical bond of H_2. The advantages of this design are the absence of wires and packaging (which saves on material cost) and the ability to assemble the device entirely in one dimension, so that tool precision requirements are relaxed (as compared to assembly of 2D integrated chip).

The layers consist of a transparent conductive oxide (TCO)-coated triple-junction crystalline-Si PV, in which Co-OEC has been deposited onto the p-doped silicon (p-Si) side (Fig 1.5).[42] In such a configuration, the light-collecting side functions as the anode, while on the reverse side, a hydrogen-evolving catalyst is deposited. ITO is used as a transparent protective barrier, preventing the p-Si from oxidation, which would otherwise negate its light-absorption properties (although FTO can also be used as the TCO).[43] This construct represents a simple device that can be operated in water to store solar energy as evolved H_2 and O_2 gas.

A separated PV system coupled to an electrolyzer does not require the addition of a TCO. However, this advantage of separating the PV from the electrolyzer is comparatively small, since the PV system still requires Ag for finger contacts and bus bars, as well as metal wiring to the electrolyzer. In 2010, 2000 t of Ag were used for contacts on Si PVs, amounting to 7% of the total annual world Ag supply or 30% of all Ag used in electronics.[44] Ag supplies cannot keep pace with PV production if the industry is to meet future energy demands. The amount of Ag required is determined solely by the trade-off of resistive power loss. Cu is not a suitable material due to both resistivity and Cu's ability to diffuse rapidly into Si, thereby compromising the PV.[44] Since ITO is applied in a thin film (~400 nm), resistive loss is attenuated using minimal material. A cost analysis suggests that moving to other TCOs does not significantly reduce the cost of a solar capture device, since In is used in such a small quantity in ITO.[45] Removing the TCO altogether results in considerations to the solution junction, which greatly complicates the device. Moreover, a dedicated electrolyzer system would require a stable electrode to support a catalyst or to serve as the catalyst itself. Conventional electrolyzers use Pt, which is currently one of the most expensive commodity elements.

1.3.1 PV and OEC interplay in a PEC

The PEC described above was can achieve a solar-to-fuel efficiency of 10%, with forecasted efficiencies upward of 15%.[46] Every increment of efficiency and cost will determined the overall cost of electricity against readily available fossil fuels.

To achieve the highest solar-to-fuels possible, the PV should employ multiple junctions in order to capture as much of the solar spectrum as possible and also to supply the overpotential required to drive OER. To absorb different energies of the solar spectrum, the content of Ge in each layer is varied (more Ge results in a lower bandgap, which absorbs lower energy photons).[47] While a typical single junction Si cell may have an open circuit voltage (V_{oc}) of 0.7–0.8 V , multi-junction cells can achieve a V_{oc} of 1.49 V. (GaInP/GaAs/Ge PVs can attain a V_{oc} of 2.62 V.)[48] Since multi-junction cells absorb more of the solar spectrum, they also have a larger efficiency (32%) than single junction cells (10-25%). The difference in efficiency is also in part to multi-junction cells having a lower short circuit current density (J_{sc}, 14.37 mA/cm^2) than single junction cells (42.7 mA/cm^2), and the lower current results in less resistive loss in the contacts. While a lower J_{sc} results in a decrease in the upper limit of current, the higher V_{oc} means that the multi-junction cell can meet the potentials required to drive OEC at an appreciable rate, so overall, the multi-junction cell will perform OER at significantly larger currents according to the catalyst's electrokinetic behavior. Multi-junction PVs also have larger fill factors, which can support higher currents at more anodic potentials. While the PV has its own solar-to-electric efficiency, the interplay between the j-V curve of the PV and the catalyst's electrokinetics determines the overall solar-to-fuels efficiency of a PEC.[49]

1.3.2 Catalyst loading

A significant variable in designing a PEC is the catalyst loading. As previously mentioned, hydrous metal oxides, like Co-, Ni- and Mn-OEC, are generally porous. Since these catalyst films are porous, they have internal active sites. Thus, catalytic activity generally scales with film thickness. While the Tafel slope remains the same for films of various thicknesses (the slope is dependent on the catalytic mechanism), increases in activity are observed as an increase in exchange current density (Figure 1.6a). While differences in exchange current densities for different catalyst loadings appear inappreciably small, they scale logarithmically with potential and are hence significant at higher potential regimes. Having more catalyst loading per geometric area is equivalent to decreasing the overpotential required to sustain a given current density.

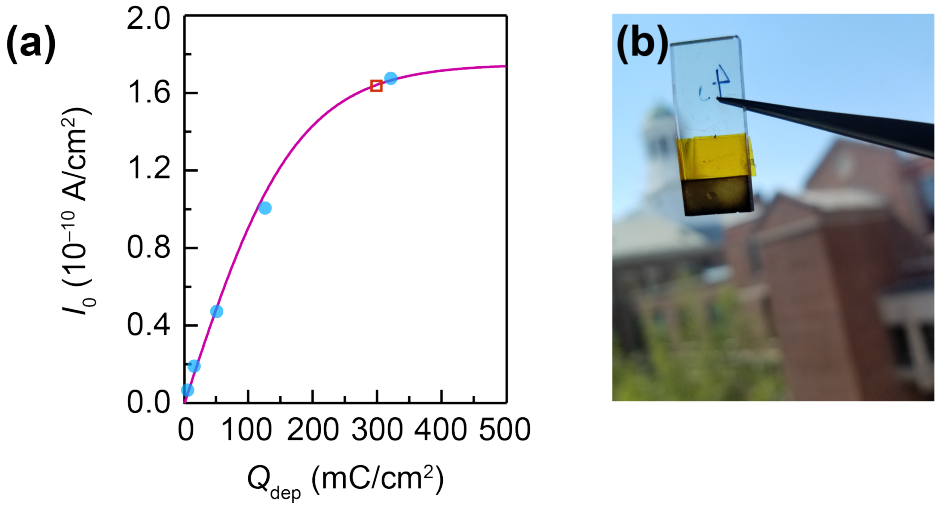


Figure 1.6. (a) Exchange current density as a function of charge passed during film deposition. Charge passed correlates with the number of active sites, which increases activity and film thickness. This results in a diffusion limitation to active sites. Activity is predicted to obey $I_0=I_0^{max}\tanh(Q_{dep}/Q_{dep}^{opt})$, where I_0^{max} is exchange current limited by diffusion and Q_{dep}^{opt} is where activity begins to become less dependent on film thickness. The red square marks the charge passed for the film shown in (b). (b) Co-OEC film (below yellow tape) on FTO illustrating parasitic light absorption of a film were Q_{dep} = 300 mC/cm^2.

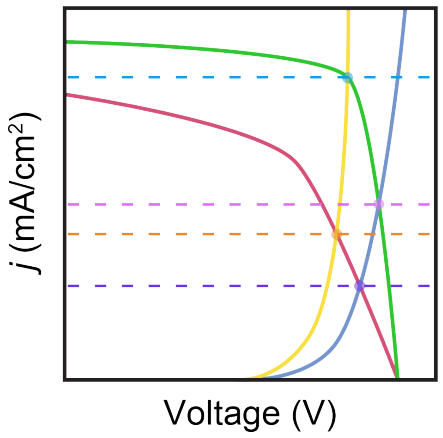


Figure 1.7. Catalytic waves for OER catalysts with high (—) and low (—) Tafel slopes overlaid with j-V curves for a buried junction device before (—) and after (—) catalyst loading.[49,50] Dashed lines show relative operating current densities for the four combinations.

There are limits, however, to how much the catalyst loading can influence the exchange current density. After a certain value of charge is passed for depositing the film (Q_{dep}), the exchange current density is predicted to diminish according to a hyperbolic tangential relationship caused by diffusion through the film. This implies that there is some optimal Q_{dep}, Q_{dep}^{opt}, that should be used for deposition.

Even so, there is another interplay in a PEC that precludes optimizing the device through the homogenous deposition of an OEC with $Q_{dep} = Q_{dep}^{opt}$; the interaction between the OEC and sunlight prevents light from reaching the PV. Figure 1.6b demonstrates this interplay for a Co-OEC film near its Q_{dep}^{opt}. Having a large catalyst loading in this configuration will erode the observed fill factor and actually cause the overall efficiency of the device to decrease.

Figure 1.7 illustrates how these interplays interact together in an integrated PEC. Depending on the choice of PV and the light absorption of the catalyst, the relative efficiency of the system may depend more on the catalyst loading, the Tafel slope, or choice of PV.[49] For instance, if the PV is operating at potentials where the current for OER is activation controlled or

mixed controlled, then any decrease of the fill factor can dramatically curb the efficiency of the device, especially for catalysts with low exchange current densities and low Tafel slopes that would otherwise run near the V_{oc} of the PV.

Trotochaud *et al.* have calculated an optimal thickness for a Co oxide OEC coating of just 3 nm.[51] NiCoOx and NiFeOx are predicted to have even smaller optimal thicknesses that are less than 1 nm. At this thickness, a hydrous oxide is composed of small islands rather than a homogenous film, which would likely change the results of the model. It is also worth noting that they treat the PV as an ideal photodiode and only change the J_{sc} value as a function of catalyst loading. Regardless, their calculation illustrates the impact that a catalyst's parasitic light absorption has on PEC efficiency.

1.4 Patterning materials

The ability to distribute oxide OER catalysts over an electrode could offer a new strategy for improving the artificial leaf. However, the method of distributing the catalyst must be affordable to implement and also account for resistive losses.

1.4.1 Catalyst distribution

Aside from impractically thin films, a catalyst can be selectively distributed over a PEC to increase transmission to the PV. Figure 1.8c–e shows different geometries of an OEC on a PV. For the case where catalyst is distributed as a homogenous film on one half of the PV (Figure 1.8c), an increase in exposed PV would increase the solar-to-fuel efficiency of the device, but the distance between the excited electron-hole pairs and OEC active sites results in resistive

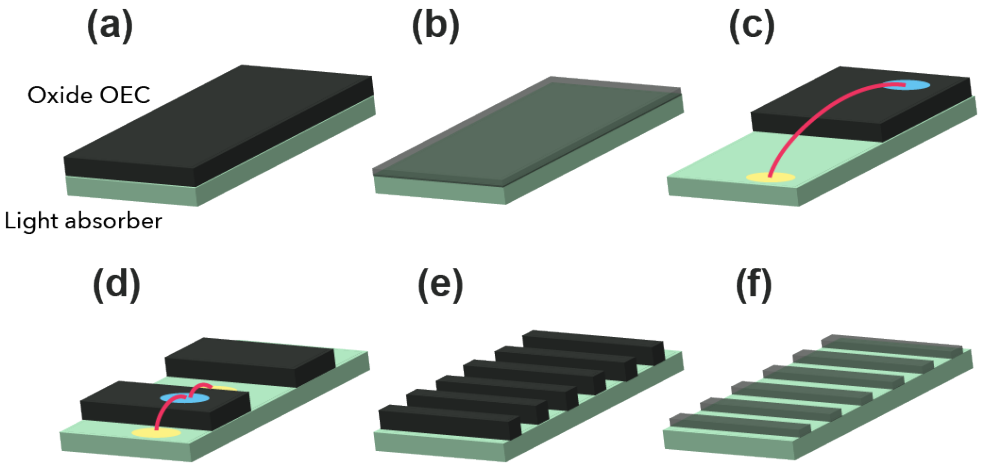


Figure 1.8. Schematics of PECs with various OEC loadings and distributions. (a) Thick, homogenously distributed OEC significantly blocks PV from light (b) Homogenously distributed OEC must be extremely thin (3 nm, far below Q_{dep}^{opt}) in order not to impair PEC efficiency.[51] (c) Thick OEC distributed on half of the PEC allows light transmission, but holes must flow from the most distal excited site (yellow circle) and to the most distal active site (blue circle), thereby increasing resistive loss (ρ_{FTO} = 7–41 Ω/sq).[43] (d) Evenly distributed OEC shortens the path length that holes must travel to reach active sites. (e) Further distributing OEC increases mass transport, but also results in higher current densities.[52] (f) Combination of (b) and (e) yet to be explored.

losses due to the sheet resistance of TCO (for F-doped Sn oxide (FTO), ρ = 7–41 Ω/sq).[43] Instead, the OEC could be distributed evenly across the PV as discrete islands or bands. Chen *et al.* examined some of the ways that distributing an opaque catalyst over a light absorber would affect the overall solar-to-fuel efficiency of the device.[52] In their study, Pt islands were distributed over As-doped Si. This catalyst geometry led to multiple interesting consequences. For one, the mass transport to the catalyst is increased by radial diffusion. However, the geometry also causes an increase in current density, which increases η_{jR}. The optimal solar-to-hydrogen efficiency was calculated to be 25% corresponding to a geometric filling fraction of 5%.

While Chen's study provides data that informs on the patterning of opaque catalysts, such as noble metals, it neglects the possible permutations of patterning semi-transparent metal oxides. Furthermore, their use of lithography and lift-off adds an expense if fabricating a competitive PEC system. Addressing these limitations could lead to more efficient, cost-effective solar energy systems. Fabrication and patterning strategies that are relevant to achieving just that are described in the following sections.

1.4.2 Electrochemical micromachining

Electrochemical micromachining (EMM) is a method for microfabrication whereby materials are electrochemically etched on the micron to sub-micron scale by performing electrochemistry, typically through small openings in an insulating mask, such as a photoresist.[53,54] EMM affords precise control of the etching rate and extent of material etched. It allows any material to be smoothly shaped, regardless of the material's domain size or hardness, providing that the material is conductive. Furthermore, unlike mechanic micromachining techniques, no tool wearing is incurred in EMM.[55–58] Conventional EMM has been limited to the removal (etching) of material, which restricts the technique to precision milling.

1.4.3 RIPPLE

We recently reported a method of EMM designated reactive interface patterning promoted by lithographic electrochemistry (RIPPLE), which allows for patterning micron- and submicron-scale concentric rings (resembling a ripple pattern) in thin films of metal or semi-metal overlaying a substrate. The method relies on cyclic voltammetry (CV) and lithogra-

phy.[59] Patterns of concentric rings are achieved by submerging the sample in 0.5 M H_2SO_4, which allows the metal to be electrochemically etched through a small (2 μm × 2 μm) square perforation. RIPPLE is schematically described in Figure 1.9. For a 250 nm film of Ge, it was found that rings of Ge oxide 20 nm wide and 200 nm tall could be formed around the perforations. The ring diameter and period can be controlled by the scan rate, and the number of rings can be controlled by the number of cycles. Cu metal was also successfully patterned in this fashion, resulting in Cu oxide rings. The patterns are highly reproducible and possess interesting photonic properties. Our efforts to develop this technique are elaborated in Part 2.

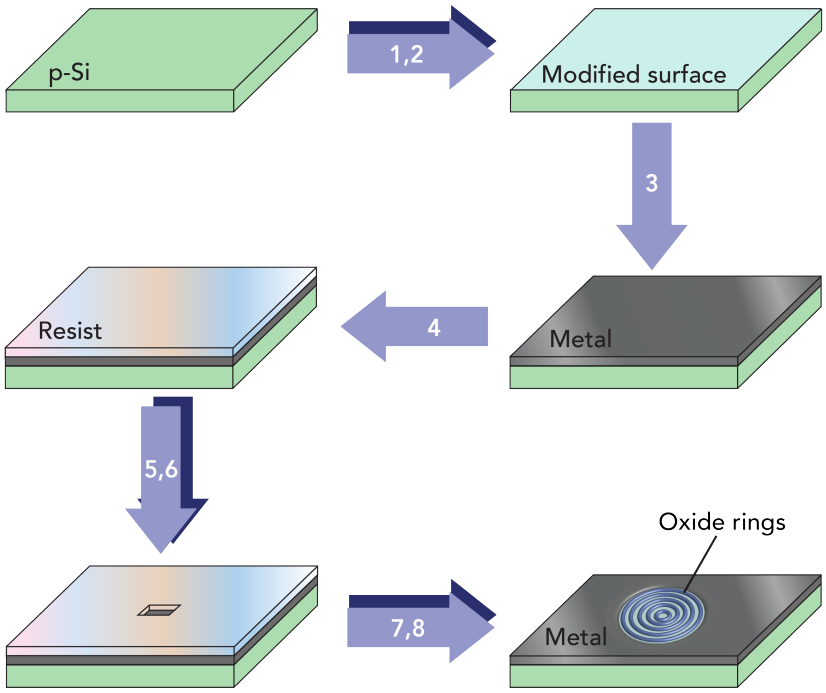


Figure 1.9. The RIPPLE technique, as first reported, can be summarized in 8 steps represented by the arrows: 1. Substrate surface is prepared for coating (p-Si is etched) 2. Optional protective layer, such as ITO, is sputtered onto the substrate. 3. Material film is deposited. 4. Resist is spin-coated over film. 5. Resist is exposed using lithography. 6. Resist is developed. 7. Cyclic voltammetry is performed on the sample. 8. Resist is stripped off.[59]

The RIPPLE method could be used to directly pattern oxide OECs. González-Flores *et al.* has shown that a crystalline Co oxide converts to our phosphate-based Co-OEC under water-splitting conditions.[60] Of particular relevance, our group has previously demonstrated that metal Co can be directly converted to Co-OEC by application of a sufficiently anodic potential in the presence of phosphate buffer.[61] These studies provide the basis for using RIPPLE to distribute rings of a functional OEC.

1.5 Overview

This thesis details how the work on the RIPPLE project resulted in a low-cost, scalable procedure that could be applied to the challenge of making a competitive PEC device. The ensuing results pertaining to RIPPLE represent our group's first efforts in the field of EMM. Progress was achieved largely as a team effort, especially initially, with an original team consisting of then-graduate student, Kwabena Bediako, and then-postdoctoral researcher, Tom Kempa. As the project progressed, interests shifted from fundamental understanding of an electrochemical phenomenon towards real-world application to an important scientific challenge of our time.

Succeeding this introduction, Part 2 details the exploratory phase of RIPPLE, investigating its applicability to a variety of materials and also optimizing parameters for new materials. The possible compositions of electrochemically-generated patterns are expanded in this way. Electroplated materials and coarse substrates are patterned to test RIPPLE's tolerance for imperfections and surface roughness. These results are aimed at simplifying sample preparation. Part 2 also looks at the applicability of RIPPLE to an OER catalyst, namely Co-OEC.

In Part 3, the electrochemical technique is changed from a scanning function to a concerted binary step procedure, producing patterns by alternating between two discrete voltages. This new method simplifies electrical component requirements and affords better control over pattern geometry. In addition, insight is provided into the patterning mechanism. The mechanism is understood through a model that successfully simulates a pattern. Knowledge of the mechanism allows us to further refine the technique by avoiding mass transport limitations.

Part 4 examines the role of the overlying resist. By varying the Young's modulus or thickness of the resist, new patterns are observed, as predicted by the model in Part 3. Understanding how the resist affects the pattern inspires a new patterning technique that replaces the resist with particles dispersed as an emulsion. Since the new technique no longer requires lithography or other precision fabrication techniques, a scalable method is realized that is capable of patterning materials on the benchtop.

Part 5 looks at patterning materials by exploiting the three-phase interphase formed while suspending a substrate in solution. The use of a gaseous phase to engender a moving boundary obviates the need for a solid-state mask, thereby further lowering the costs of patterning. Part 5 concludes with a demonstration of a new method for fabricating parallel, submicron oxide wires. Future direction for the project is outlined.

Finally, Part 6 explores the dynamics of Co-OEC as a function of pH. This analysis yields information on the fundamental behavior of Co-OEC during deposition and OER catalysis. Our understanding of the factors underlying OEC dynamics leads to a new Fe-based, acid-stable OEC with extraordinary OER activity.

In summary, the initial focal point of this project was developing RIPPLE as a fabrication technique and understanding how patterns form. However, the applicability of using elec-

trochemistry to distribute metal oxides over an electrode is the specific real-world application that motivates this work. This purpose is aligned with the objectives of our group to design a solar energy system that will be competitive with fossil fuels.

1.6 References

(1) Whitesides, G. M.; Crabtree, G. W. *Science* **2007,** *315,* 796–798.

(2) BP Statistical Review of World Energy, 2016. https://www.bp.com/content/dam/bp/en/corporate/pdf/bp-statistical-review-of-world-energy-2016-full-report.pdf (accessed May 1, 2017).

(3) Approximate conversion factors. BP Statistical Review of World Energy. https://www.bp.com/content/dam/bp/pdf/energy-economics/statistical-review-2016/bp-statistical-review-of-world-energy-2016-approximate-conversion-factors.pdf (accessed May 1, 2017).

(4) Berner, R. A. *Nature* **2003,** *426,* 323–326.

(5) NOAA, ESRL, Global Monitoring Division. Trends in Atmospheric Carbon Dioxide. https://esrl.noaa.gov/gmd/ccgg/trends/ (accessed May 1, 2017).

(6) Canadell, J. G.; Le Quéré, C.; Raupach, M. R.; Field, C. B.; Buitenhuis, E. T.; Ciasis, P.; Conway, T. J.; Gillett, N. P.; Houghton, R. A.; Marland, G. *PNAS* **2007,** *104,* 18866–18870.

(7) Rodhe, H.; Charlson, R.; Crawford, E. *Ambio,* **1997,** *26,* 2–5.

(8) Uppenbrink, J. *Science* **1996,** *272,* 1122.

(9) Arrhenius, S. *Philos. Mag.* **1896,** *41,* 237–276.

(10) Winkelmann, R.; Levermann, A.; Ridgwell, A.; Caldeira, K. *Sciecne Adv.,* **2015,** *1,* 1–5.

(11) IPCC 2007, Summary for Policymakers, in *Climate Change 2007: Impacts, Adaptation and Vulnerability. Contribution of Working Group II to the Fourth Assessment Report of the Intergovernmental Panel on Climate Change,* Cambridge University Press, Cambridge, UK.

(12) Hayhow, K.; Kossin, J.; Kunkel, K.; Stephenes, G.; Thorne, P.; Vose, R.; Wehner, M.; Willis, J. *The Third National Climate Assessment,* U.S. Global Change Research Program, May, 2014.

(13) NOAA, National Centers for Environmental Information. State of the Climate: Global Climate Report for March 2017. Published online April 2017. https://www.ncdc.noaa.gov/sotc/global/201703 (accessed on May 3, 2017).

(14) Lewis, N. S.; Nocera, D. G. *PNAS* **2007,** *104,* 15729–15735.

(15) Bethe, H. A. *Physical Review* **1938,** *55,* 434–456.

(16) Eddy, J. A. "A New Sun, the Solar Results from Skylab." NASA Report SP-402 (1979).

(17) Lewis, N. S.; Nocera, D. G. *The Bridge,* **2015,** *45,* 41–47.

(18) Philips, T. Science@NASA. A Puzzling Collapse of Earth's Upper Atmosphere. https://science.nasa.gov/science-news/science-at-nasa/2010/15jul_thermosphere/ (accessed May 1, 2017).

(19) Martin, G. Solar Cells: Operating Principles, Technology, and Applications, 1st ed.; Prentice-Hall International: London, 1982

(20) Lowen, A.; van Sark, W.; Schropp, R.; Faaij, A. *Sol. Energy Mater. Sol. Cells* **2016,** *147,* 295–314.

(21) Rowlands-Rees, T.; Izadi-Najafabadi, A.; Orlandi, I. "Distributed Solar and Storage – ICEF Roadmap 1.0" December 2015.

(22) McKone, J. R.; Lewis, N. S.; Gray, H. B *Chem. Mater.* **2014,** *26,* 407–414.

(23) Bockris, J. O'M. *Int. J. Hydro.* **2002,** *27,* 731–740.

(24) Torella, J. P.; Gagliardi, C. J.; Chen, J. S.; Bediako, D. K.; Colón, D.; Way, J. C.; Silver, P. A.; Nocera, D. G. *PNAS,* **2015,** *112,* 2337–2342.

(25) Liu,C.; Colón, B. C.; Ziesack, M.; Silver, P. A.; Nocera, D. G. *Science,* **2016,** *352,* 1210–1213.

(26) Gileadi, E. *Physical Electrochemistry: Fundamentals, Techniques and Applications*, 1st ed.; Wiley-VCH: Weinheim, 2011.

(27) Eisenberg, R.; Gray, H. B. *Inorg. Chem.* **2008**, *47*, 1697–1699.

(28) Cukier, R. I. Nocera, D. G. *Annu. Rev. Phys. Chem.* **1998,** *49,* 337–369.

(29) Surendranath, Y.; Nocera, D. G. *Prog. Inorg. Chem.* **2011,** *57,* 505–560.

(30) Kanan, M. W.; Nocera, D. G. *Science* **2008,** *321,* 1072.

(31) Dincă, M.; Surendranath, Y.; Nocera, D. G. *PNAS* **2010,** *107,* 10337.

(32) Huynh, M.; Bediako, D. K.; Nocera, D. G. *J. Am. Chem. Soc.* **2014,** *136,* 6002–6010.

(33) Lutterman, D. A.; Surendranath, Y.; Nocera, D. G. *JACS* **2009,** *131,* 3838–3839.

(34) Surendranath, Y.; Lutterman, D. A.; Liu, Y.; Nocera, D. G. *J. Am. Chem. Soc.* **2012,** *134,* 6326–6336.

(35) Huynh, M.; Bediako, D. K.; Liu, Y.; Nocera, D. G. *J. Phys. Chem. C.* **2014,** *118,* 17142–17152.

(36) Bediako, D. K.; Surendranath, Y.; Nocera, D. G. *J. Am. Chem. Soc.* **2013,** *135,* 3662–3674.

(37) Ullman, A. M.; Brodsky, C. N.; Li, N.; Zheng, S.–L.; Nocera, D. G. *J. Am. Chem. Soc.* **2016,** *138,* 4229–4236.

(38) Kanan, M. W.; Yano, J.; Surendranath, Y.; Dincă, M.; Yachandra, V. K.; Nocera, D. G. *J. Am. Chem. Soc.* **2010,** *132,* 13692–13701.

(39) Bediako, D. K.; Lassalle-Kaiser, B.; Surendranath, Y.; Yano, J.; Yachandra, V. K.; Nocera, D. G. *J. Am. Chem. Soc.* **2012,** *134,* 6801.

(40) Huynh, M. Shi, C.; Billinge, S. J. L.; Nocera, D. G. *J. Am. Chem. Soc.* **2015,** *137,* 14887–14904.

(41) Esswein, A. J.; Surendranath, Y.; Reece, S. Y.; Nocera, D. G. *Ener. Env. Sci.* **2011,** *4,* 499–504.

(42) Nocera, D. G. *Acc. Chem. Res.* **2012,** *45,* 767–776.

(43) Cox, C. R.; Winkler, M. T.; Pijpers, J. J. H.; Buonassisi, T.; Nocera, D. G. *Ener. Env. Sci.* **2013,** *6,* 532–538.

(44) Green, M. A. *Prog. Photovolt: Res. Appl.* **2011,** *19,* 911–916.

(45) Louwen, A.; van Sark, W.; Schropp, R.; Faaij, A. *Sol. Ener. Mater. Sol. Cells,* ***I2016,*** *147,* 295–313.

(46) Nocera, D. G. *Acc. Chem. Res.* **2017,** *50,* 616–619.

(47) Reddy, P. J. *Solar Power Generation: Technology, New Concepts, & Policy* Taylor & Francis Group, LLC-CRC Press: Boca Raton, FL, 2012.

(48) Green, M. A.; Emery, K.; Hishikawa, Y.; Warta, Wilhelm *Prog. Photovolt: Res. Appl.* **2011,** *19,* 84–92.

(49) Surendranath, Y.; Bediako, D. K.; Nocera, D. G. *PNAS* **2012,** *109,* 15617–15621.

(50) Reece, S. Y.; Hamel, J. A.; Sung, K.; Jarvi, T. D.; Esswein, A. J.; Pijipers, J. J. H.; Nocera, D. G. *Science,* **2011,** *334,* 645–648.

(51) Trotochaud, L.; Mills, T. J.; Boettcher, S. W. *J. Phys. Chem. Lett.* **2013,** *4,* 931–935.

(52) Chen, Y.; Audesirk, H.; Xiang, C.; Lewis, N. S.; *Ener. Env. Sci.* **2015,** *8,* 1736–1747.

(53) Köhler, M. Etching in Microsystem Technology; Wiegand, A., Transl.; Wiley-VCH: Weinheim, Germany, 1999; pp 74–79.

(54) Kern, P.; Veh, J.; Michler, J. *J. Micromech. Microeng.* **2007,** *17,* 1168–1177.

(55) Li, W.; Quandai, W.; Xiuqing, H.; Yucheng, D.; Bingheng, L. *Process. Int. J. Adv. Manuf. Tech.* **2010,** *51,* 155–162.

(56) Schuster, R.; Kirchner, V.; Allongue, P.; Ertl, G. *Science* **2000,** *289,* 98–101.

(57) Datta, M.; Romankiw, L. T. *J. Electrochem. Soc.* **1989,** *136,* 285C–292C.

(58) Datta, M.; Landolt, D. *Electrochim. Acta* **2000,** *45,* 2535–2558.

(59) Kempa, T. J.; Bediako, D. K.; Kim, S.-K; Park, H.-G. Nocera, D. G. *PNAS* **2015,** *112,* 5309–5313.

(60) González-Flores, D.; Sánchez, I.; Zaharieva, I.; Klingan, K.; Heidkamp, J.; Chernev, P.; Menezes, P. W.; Driess, M.; Dau, H.; Montero, M. L. *Angewandte* **2015,** *127,* 2502–2506.

(61) Young, E. R.; Costi, R.; Paydavosi, S.; Nocera, D. G.; Bulović *Ener. Env. Sci.* **2011,** *4,* 2058–2061.

Part 2. Expanding the applicability of RIPPLE beyond Ge to other materials and substrates

Portions of this chapter have been published:
Kempa, T. J.; Bediako, D. K.; Jones, E. C.; Kim, S.-K.; Park, H.-G.; Lieber, C. M.; Nocera, D. G. *J. Am. Chem. Soc.*, **2015,** *137,* 3739–3742.

2.1 Introduction

It was observed in our group that when a chemical vapor deposition (CVD)-grown film of Ge metal coated with a polymer resist containing lithographically-generated square openings (2 μm × 2 μm) is subjected to CV (0.1–1.2 V vs. Ag/AgCl) in 0.1 M H_2SO_4, patterns containing concentric rings of Ge oxide appear centered around each opening. Moreover, the number of the rings and spacing between rings are determined by the number of cycles and the scan rate, respectively. The number of rings, N_R, follow the function $N_R = N_{CV} - 1$, where N_{CV} is the number of cycles. Rings are 20 nm high and 360 nm wide. Performing the same experiment in 0.1 M K_2SO_4 results in N_R periodic "terraces," which sequentially decrease in height from the center. Patterns could also be generated in films coated on nonconductive plastic sheets.

This observation led to a technique designated as reactive interface patterning promoted by lithographic electrochemistry (RIPPLE). Besides allowing patterns to be generated quickly from a relatively simple lithographic feature, this process also allows patterning over sloped surfaces, where line-of-site lithography cannot access without rotating the entire sample around an axis in the plane of the substrate. The complexity of the patterns, which are formed in a matter of seconds, makes RIPPLE an exceptionally facile approach to fabrication.

The succeeding sections will discuss patterning electron-beam deposited Co and Ni and electroplated Co. These metals are of interest to our group because of their oxides' ability to perform catalytic OER under buffered conditions at low overpotentials. We will also examine the effect of the roughness of the substrate in order to test the tolerance of RIPPLE for imperfections in the substrate's surface. Lastly, we propose a strategy for creating entirely metallic

patterns indirectly by RIPPLE. Creating patterns of new materials by RIPPLE allows us to determine the scope of this technique.

2.2 Results

2.2.1 Electron-beam deposited Co

To replicate the Ge RIPPLE patterns in Co, an analogous sample was prepared by depositing a 250 nm thick Co metal film onto a Si substrate. PMMA electron-beam resist was spin coated over the Co, as was previously done for Ge, and 2 μm × 2 μm square openings were lithographically defined in the PMMA. The bias was then cycled linearly between various potentials. After cycling to and from 0.4 V and 1.3 V at 100 mV/s in 0.1 M H_2SO_4, well-defined circular patterns were generated at each opening in the resist, as apparent by SEM (Figure 2.1a). The CV shows a steady increase in current consistent with an increasing electrode surface area (Figure 2.1b). While these patterns do verify RIPPLE's ability to pattern Co metal, Co rapidly

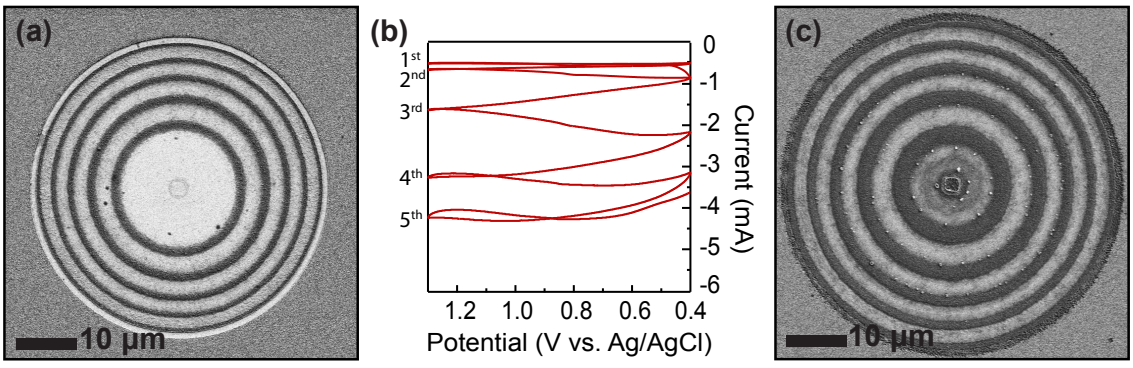


Figure 2.1. (a) SEM image (SE2 detector) of a 250 nm Co film patterned by RIPPLE by cycling from 0.4 V to and from 1.3 V at 100 mV/s in 0.1 M H_2SO_4. (b) Cyclic voltammogram used to generate pattern in (a). Scan order designated on left side. (c) SEM image (SE2 detector) of a 250 nm Co film patterned by RIPPLE by cycling from 0.4 V to and from 1.3 V at 100 mV/s in 0.1 M K_2SO_4.

and spontaneously dissolves under acidic conditions.[1] Thus, the same RIPPLE method was carried out at higher pH. Performing the same procedure in 0.1 M K_2SO_4 (pH 8.4) yielded similar results, but with wider oxide rings (dark rings, Figure 1c).

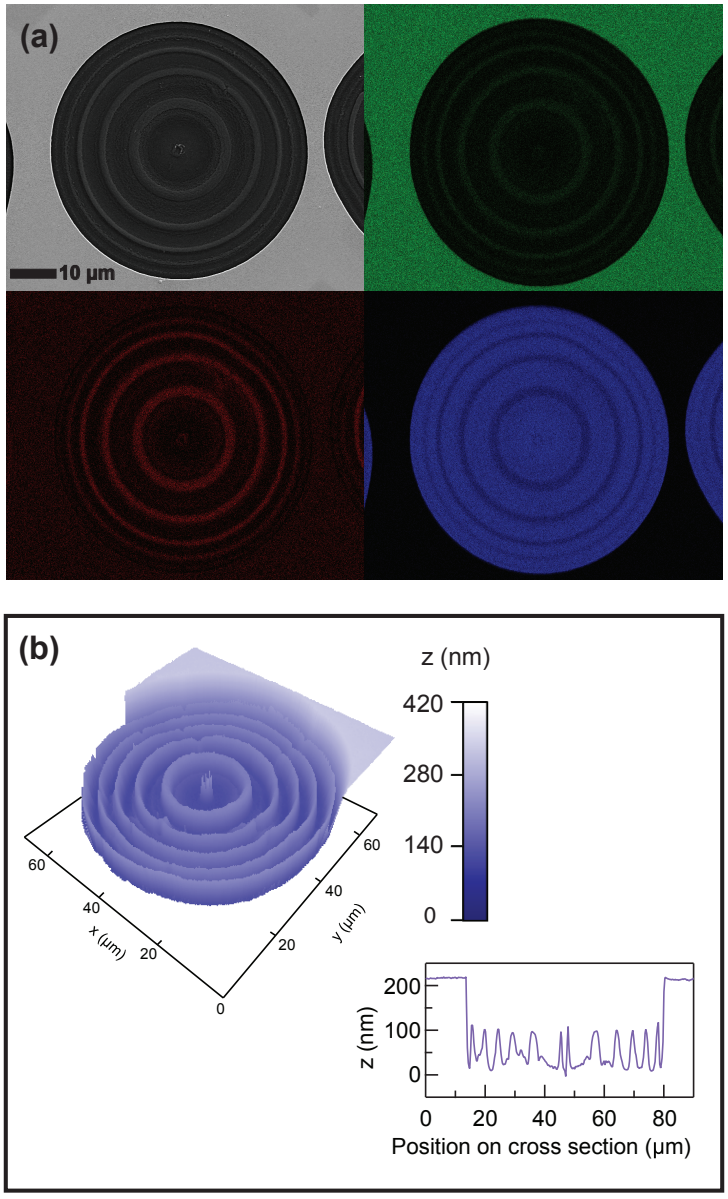


Figure 2.2. Patterns generated by cyclic voltammetry, with five cycles from 0.4 V to and from 1.3 V at 100 mV/s in 0.1 M K_2SO_4. (a) SEM images (In-lens detector, grey) and EDS maps for cobalt (green), oxygen (red), and silicon (blue). (b) 3D rendering of AFM height data with height profile of diametric cross-section (inset on bottom right).

EDS elemental maps reveal that rings of the pattern contain high concentrations of Co and O while regions between the rings only show the signature for Si, presumably from the underlying Si substrate (Figure 2.2a). The AFM height map of the pattern shows that the rings corresponding to Co and O are 100 nm tall and 2 μm wide and spaced 3 μm apart, although the ring widths and widths between rings decrease as a function of the radius (Figure 2.2b). In addition, an island appears at the center of the pattern, which was also observed in Ge patterns. Potentials applied within or outside the 0.4–1.3 V window resulted in highly disordered features or no pattern formation at all.

2.2.2 Electron-beam deposited Ni and the effect of chloride ions

The same parameters used in the CV method that permitted the patterning of Co were applied to an analogous sample containing a Ni metal film in replace of Co metal. In 0.1 M H_2SO_4 and 0.1 M K_2SO_4, no changes were observed in the metal film after application of the same CV used to pattern Co. Varying the parameters of the CV failed to incur any changes in the sample. Chloride was then added as KCl to the solution. In 0.5 M KCl and 0.1 M H_2SO_4, patterns were formed with poorly defined rings as compared to the Co pattern formed in 0.1 M K_2SO_4 (Figure 2.3a,b), while no change in the metal was observed in a solution containing 0.5 M KCl and 0.1 M K_2SO_4. Identical patterns as those produced in 0.5 M KCl and 0.1 M H_2SO_4 could also be achieved in Ni using a solution of 0.5 M HCl. RIPPLE was also attempted on Ni samples in 0.1 M H_2SO_4 with 0.1 M, 50 mM, and 10 mM. Patterns were not observed at concentrations less than 0.1 M KCl in 0.1 M H_2SO_4.

We next sought to examine the effects of Cl^- on the Co system. 0.5 M KCl was added to 0.1 M K_2SO_4 and the electrochemical procedure used to generate the pattern in Figure 2a was

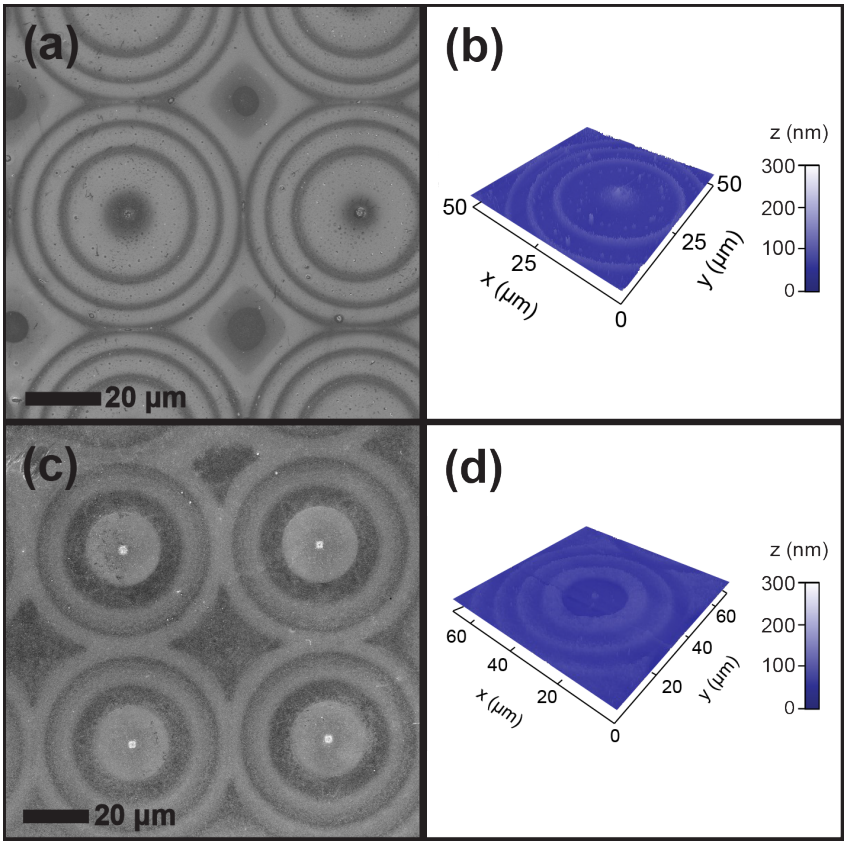


Figure 2.3. Patterning metals by RIPPLE in the presence of Cl^-. (a) SEM image (SE2 detector) of a 250 nm Ni film patterned by RIPPLE by cycling from 0.4 V to and from 1.3 V at 100 mV/s in 0.1 M H_2SO_4 and 0.5 M KCl. (b) AFM height map for a pattern in (a). (c) SEM image (SE2 detector) of a 250 nm Co film patterned by RIPPLE by cycling from 0.4 V to and from 1.3 V at 100 mV/s in 0.1 M H_2SO_4 and 0.5 M KCl. (d) AFM height map for a pattern in (c).

repeated on a film of 250 nm Co (Figure 2.3c,d). The features in the resulting pattern were similarly "washed-out" as those formed in Ni in 0.5 M KCl and 0.1 M K_2SO_4.

2.2.3 RIPPLE on rough substrates

After establishing a RIPPLE method for two metals with OER-active oxides, we next examined how the roughness of the substrate influences the ability to generate patterns by RIPPLE. Roughness of a substrate is often measured by the parameter roughness root means squared parameter, or R_{RMS}.[2] R_{RMS} can be calculated from an AFM height map of a surface by taking the RMS average of deviations in the height profile of a surface. For comparison, the R_{RMS} of FTO is 6.4 nm, whereas the R_{RMS} of Si is 350 pm – over an order of magnitude smoother (calculated from Figure 4a,b). Films of Co were electron-beam evaporated onto FTO and coated

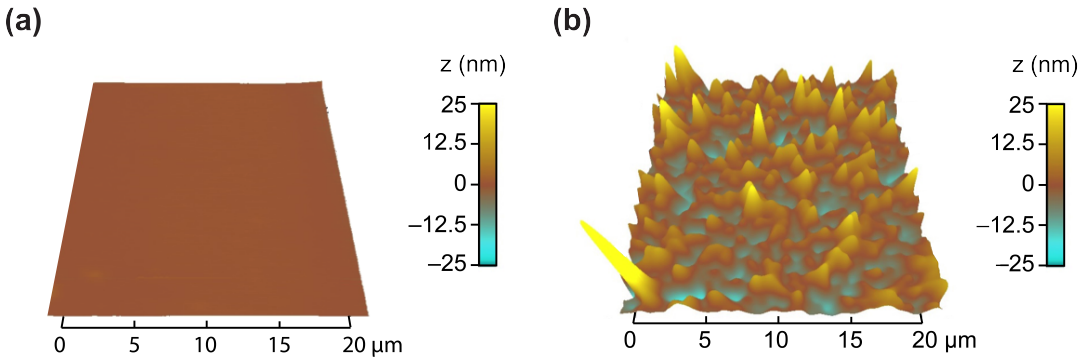


Figure 2.4. Roughness of different substrates as determined from AFM. (a) AFM height map of Si wafer. Surface roughness R_{RMS} value of 350 pm. (b) AFM height map of FTO-coated glass. Surface roughness R_{RMS} value of 6.4 nm.

with PMMA resist, which was then perforated using electron-beam lithography. The sample was partially immersed in 0.1 M K_2SO_4 so that the openings in the resist were submerged and the potential was cycled five times between 0.4 V and 1.3 V. The area of the sample that was immersed in solution turned transparent, as evident upon visual inspection (Figure 2.5a). Figure 2.5b shows that circular patterns of concentric rings were formed at each opening.

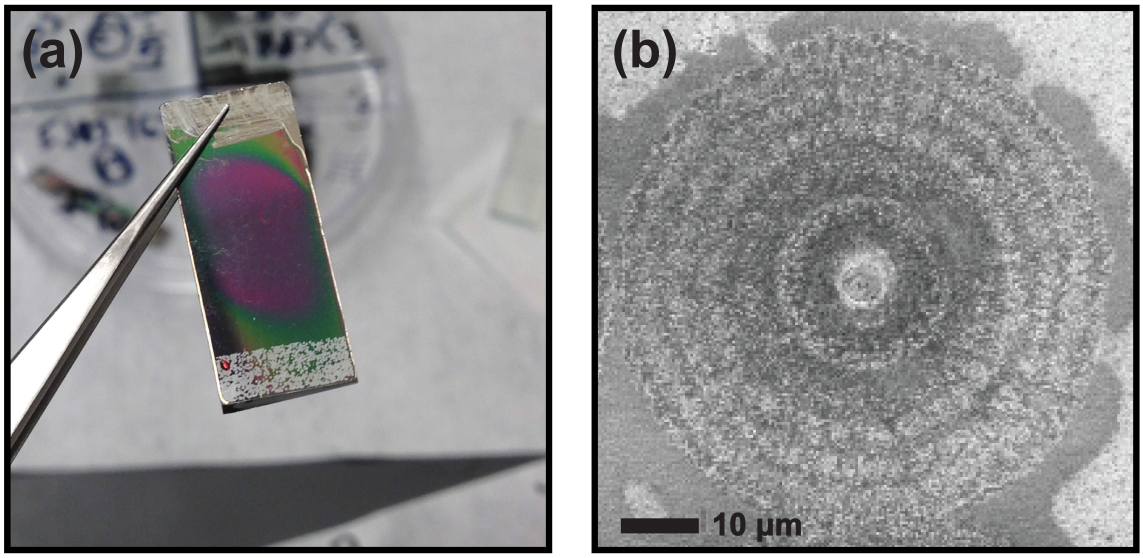


Figure 2.5. A patterned film on FTO-coated glass. (a) FTO coated with 250 nm Co and PMMA resist, after patterning. Transparent section at bottom is where the sample was exposed to 0.1 M K_2SO_4 during a cycle from 0.4 V to and from 1.3 V at 100 mV/s. (b) SEM image (SE2 detector) of patterns on sample in (a). Patterns are located at arrays of holes in resist.

2.2.4 Patterning electroplated Co

Co was then electroplated onto FTO glass from a previously reported $CoSO_4$ citrate bath by passage of 120 C/cm^2 (see experimental methods 2.5.1 for details).[3–5] As shown by SEM, the electroplating process results in platelets of Co metal rather than a smooth film. (Figure 2.6a). The platelet domains are between 1 and 2 µm long and on the order of 100 µm thick. Side profiles of the film show that it is on the order of 1 µm thick (Figure 2.6b,c).

The electroplated Co films were then coated in PMMA resist and patterned by RIPPLE by following the same procedure used in patterning e-beam evaporated Co. SEM and EDS reveal rings of oxide similar to those in the patterns formed in e-beam evaporated Co (Figure 2.3). Some Co is detected in the gap between the rings. SEM and EDS show that the rings conserve the platelet structure and are composed of Co and O.

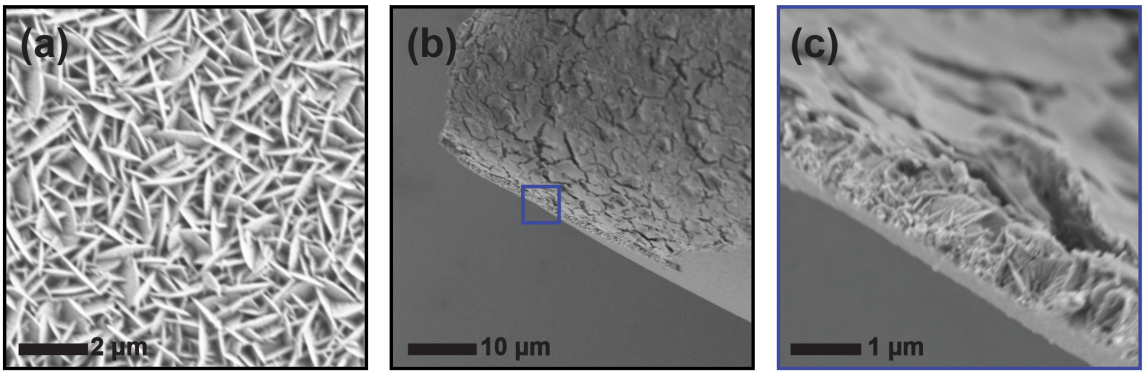


Figure 2.6. 120 C/cm^2 Co electroplated onto FTO. (a) SEM image of the film's structure. (b) SEM image of the edge of electroplated Co metal film (120 C/cm^2) delaminating from underlying FTO. (c) Magnification of blue box in (b).

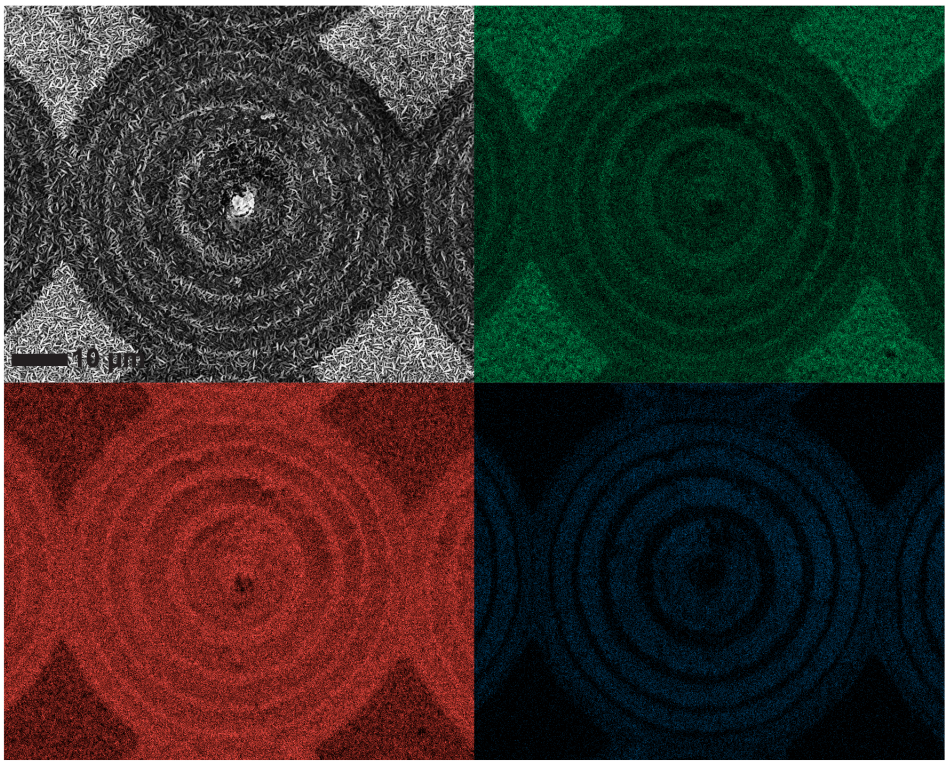


Figure 2.7. RIPPLE pattern in electroplated Co. Patterns generated by cyclic voltammetry, with five cycles from 0.4 V to and from 1.3 V at 100 mV/s in 0.1 M K_2SO_4. SEM image (grey) and EDS maps for cobalt (green), oxygen (red), and silicon (blue).

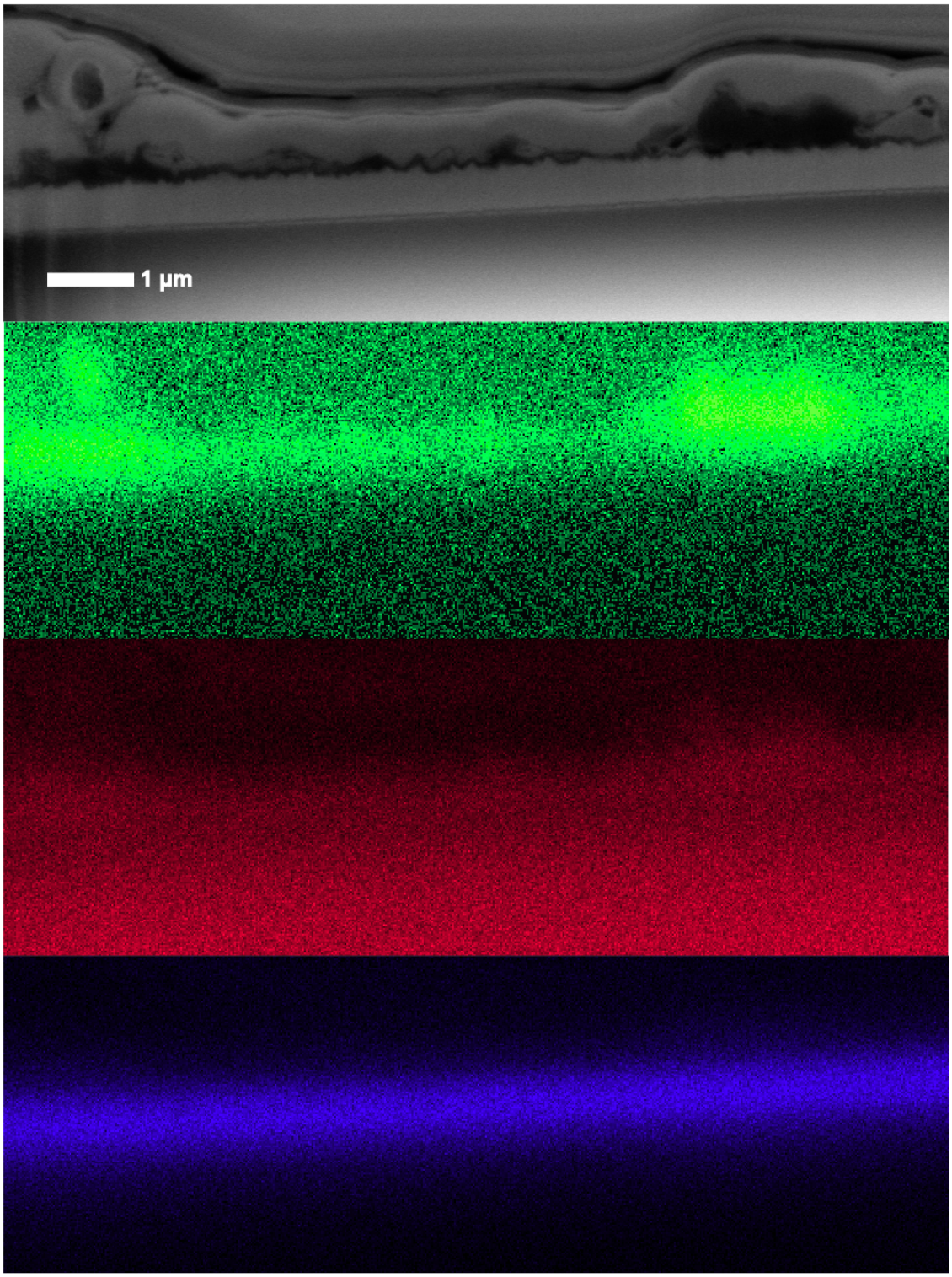


Figure 2.8. FIB cross section of a RIPPLE pattern in electroplated Co. From top to bottom: SEM image (grey) and EDS maps for cobalt (green), oxygen (red), and silicon (blue). First ring from center is on left; second ring from center is on right.

FIB cross sections reveal that the oxide rings are 1 μm tall (Figure 2.8). FIB also confirms that approximately 100 nm Co oxide lies between the rings. By examining the rings of the electroplated Co pattern, it is apparent from the cross-section SEM micrograph that a disordered structure extends to the substrate.

2.2.5 Performing catalysis with a patterned Co film

A Co film deposited over Pt-coated Si was patterned into concentric ring structures following the method described in Section 2.2.1. Anodization of this patterned Co substrate was performed following a method that has previously been shown to yield Co-OEC from Co metal (Figure 2.9a).[6] SEM and Co and O EDS maps of the anodized Co

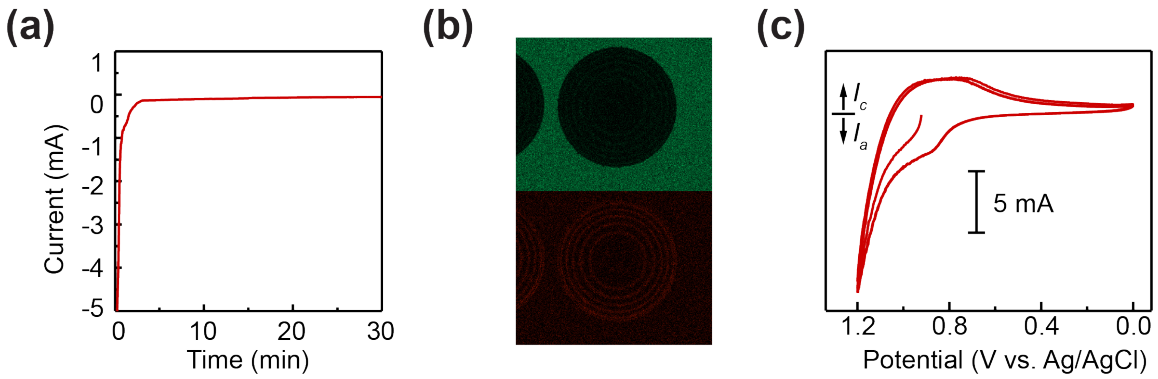


Figure 2.9. Anodization of a Co RIPPLE pattern. (a) Current trace for Co patterned by RIPPLE held at 0.85 V (below OER but above the $Co^{3+/4+}$ couple).[7] (b) EDS elemental maps of RIPPLE pattern after anodization for cobalt (green) and oxygen (red) (c) CV of Co patterned by RIPPLE after anodization, scan rate 0.1 V/s. Pre-wave at 0.8 V corresponds to $Co^{3+/4+}$ couple, while catalytic wave at left is indicative of OER.

pattern reveal well-defined concentric rings composed of the anticipated Co-OEC (Figure 2.9b). CVs of the Co-OEC film exhibit a catalytic wave at 1.0 V (Figure 2.9c) indicative of the water-splitting reaction. Furthermore, the significant steady-state catalytic current for potentials ≥ 0.9 V is consistent with that reported for electrodeposited Co-

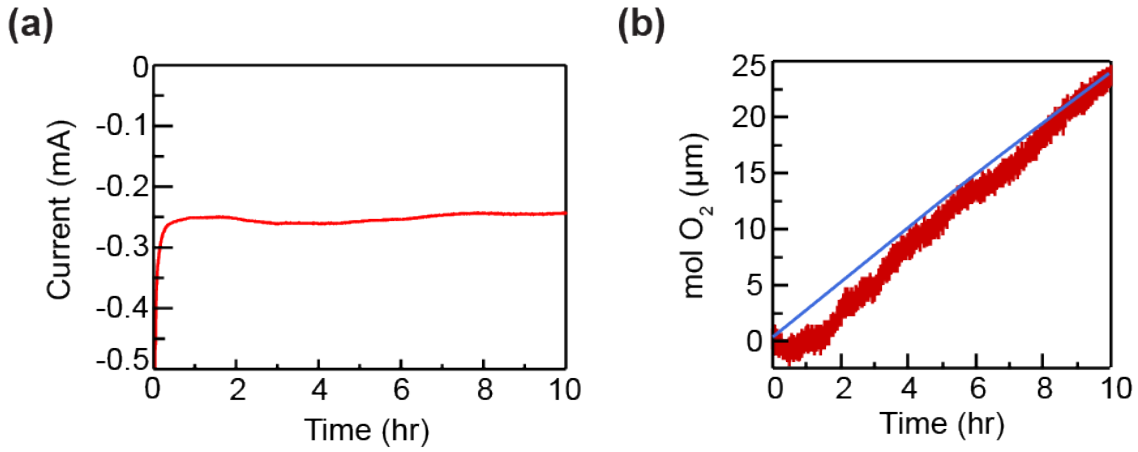


Figure 2.10. OER over 10 hr using a Co sample patterned by RIPPLE. (a) Current trace for anodized Co sample held at 1.0 V in 0.1 M KP_i, pH 7. (b) O_2 evolved by patterned Co-OEC as measured by a fluorescent probe (red) and O_2 calculated from charge passed assuming a quantitative Faradaic efficiency (black).

OEC films.[7] Electrolysis of a cm^2 area of this sample over 10 hr results in a stable current of –2.5 mA (Figure 2.10b). An oxygen probe experiment carried out over 10 hr using the patterned substrate shows a Faradaic efficiency of >99% for O_2 evolution (Figure 2.10a).

After 20 hrs of electrolysis at 1.0 V in 0.1 M KP_i (pH 7), the patterns were examined by SEM and EDS. SEM microscopy of a pattern shows a film deposited across the pattern (Figure 2.11a). The overlying material exhibits cracking. Spacing between fragments reveal the underlying pattern, though the pattern geometry is also visible in the topography of the overlying material. The spacing between fragments also suggests that the film has contracted. EDS indicates the overlying film contains Co and O (Figure 2.11b).

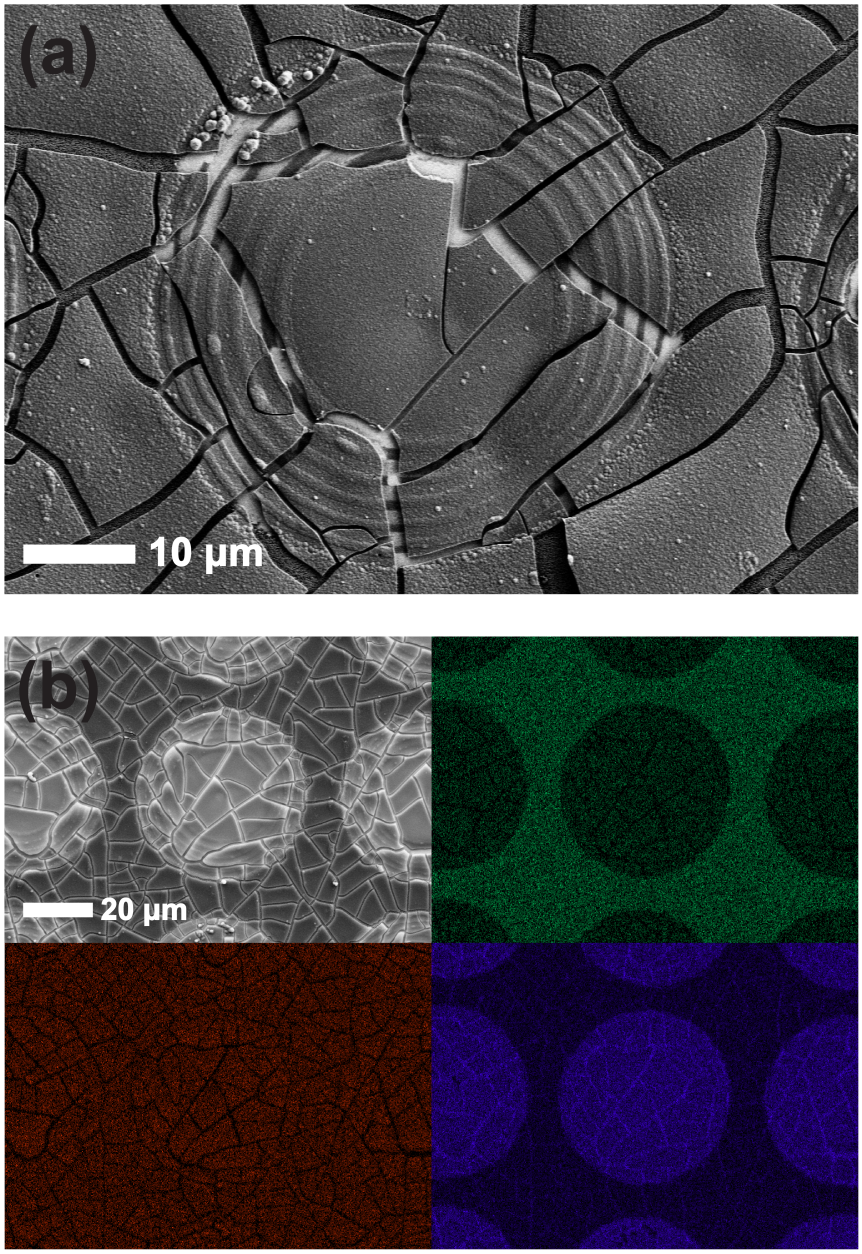


Figure 2.11. Patterns after 10 hrs electrolysis at 1.0 V in 0.1 M KP_i, pH 7. (a) SEM image of Co RIPPLE pattern, ET = 3 kV. (b) SEM image (ET = 14 kV, grey) and EDS maps for cobalt (green), oxygen (red), and silicon (blue).

2.2.6 Plasma-enhanced reduction.

H_2 plasma-enhanced chemical vapor deposition (PECVD) was employed to reduce RIPPLE patterns formed in e-beam evaporated elemental Ge and Co (see Experimental Methods 2.5.3 for details). The Ge patterns were imaged by SEM before and after reduction (Figure 2.12). The patterns are still discernable and well-defined after the reduction process. EDS elemental maps show a marked decrease in the O K-edge of the pattern after reduction (Figure 2.12b). The EDS spectra in Figure 2.13 have peaks corresponding to the O K-edge (K 0.53 keV), F K-edge (0.68 keV), Na K-edge (1.04 keV), Ge L-edge (1.19 keV), Al K-edge (1.49 keV), and Si K-edge (1.74 keV).[8] The spectra also verify a decrease in overall O post-PECVD (Figure 2.13). SEM of the Co patterns before and after PECVD show the pattern geometry is maintained after the reduction process. EDS elemental maps show a decrease in O composition of the rings (Figure 2.14), which is also visible in the EDS spectra (Figure 2.15). The EDS spectra for the Co sample shows peaks that match the O K-edge, F K-edge, Co K-edge (0.78 keV), Al K-edge, and Si K-edge.

2.3 Discussion

2.3.1 Patterning Co metal

We have two motivations for patterning Co by RIPPLE; first, as an oxide, the features of a Co pattern are expected to behave as Co-OEC; and second, there is a general desire to expand the applicability of the RIPPLE method to new materials. Towards the latter, each material behaves differently under different electrochemical conditions, requiring the optimization of the procedure.

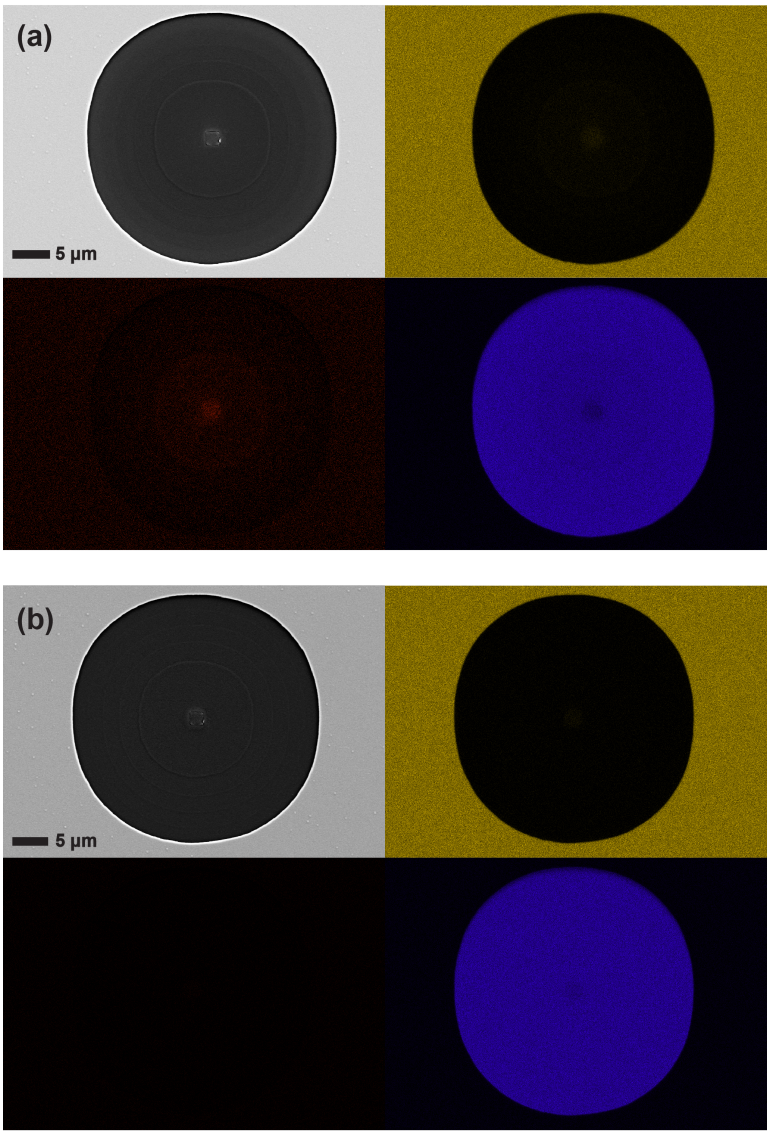


Figure 2.12. H_2 plasma-enhanced reduction of a Ge pattern, (a) before and (b) after PECVD. SEM micrograph (grey) and EDS elemental maps for germanium (yellow), oxygen (red), and silicon (blue).

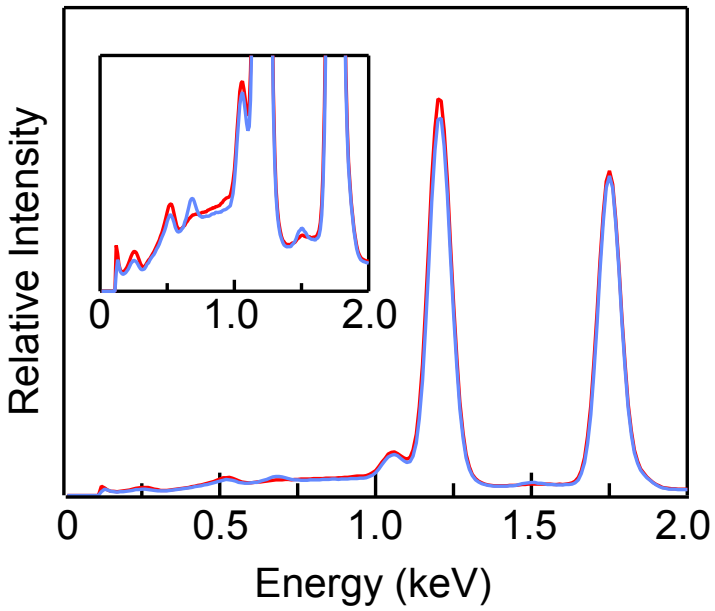


Figure 2.13. EDS spectrum for H_2 plasma-enhanced reduction of a Ge pattern, before (red) and after (blue) PECVD. Peaks correspond to O K-edge (K 0.53 keV), F K-edge (0.68 keV), Na K-edge (1.04 keV), Ge L-edge (1.19 keV), Al K-edge (1.49 keV), and Si K-edge (1.74 keV).

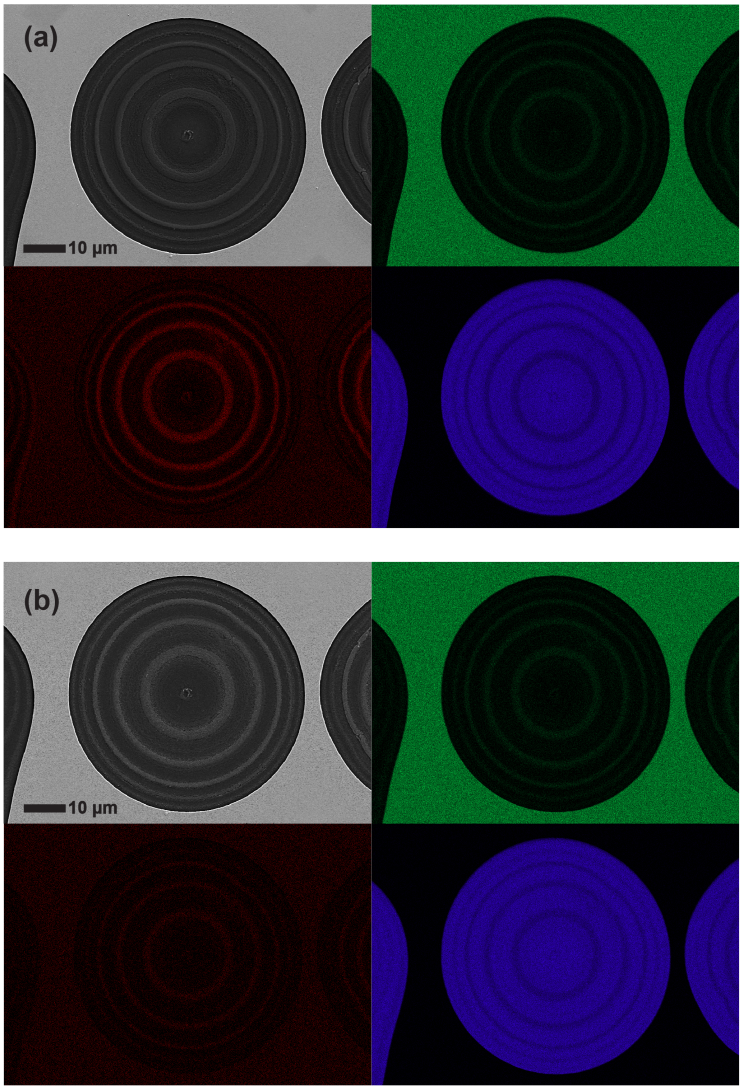


Figure 2.14. H_2 plasma-enhanced reduction of a Co pattern, (a) before and (b) after PECVD. SEM micrograph (grey) and EDS elemental maps for cobalt (green), oxygen (red), and silicon (blue).

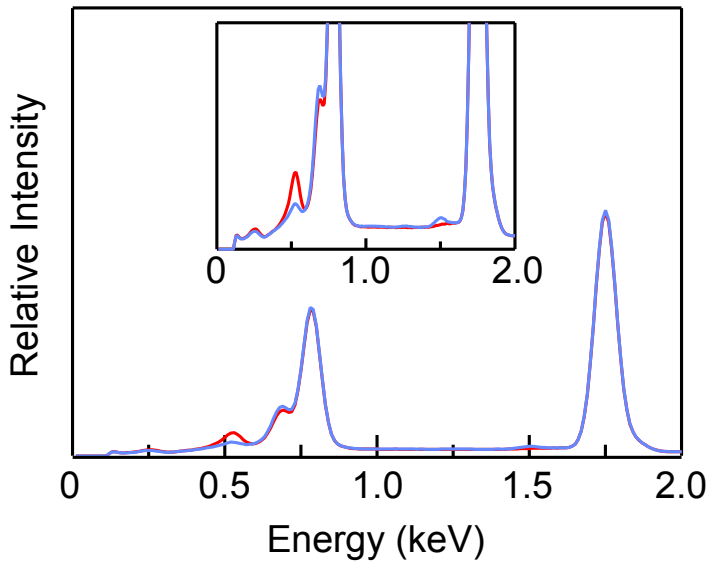


Figure 2.15. EDS spectrum for H_2 plasma-enhanced reduction of a Co pattern, before (red) and after (blue) PECVD. Peaks correspond to O K-edge (K 0.53 keV), F K-edge (0.68 keV), Co K-edge (0.78 keV), Al K-edge (1.49 keV), and Si K-edge (1.74 keV).

The SEM images and EDS elemental maps of the e-beam deposited Co sample after RIPPLE clearly depict a series of rings patterned into the Co film (Figure 2.2a). The EDS elemental maps indicate the rings contain Co and O, suggesting that the rings are discrete ridges of Co oxide and separated by regions were Co metal was etched away (where the Si signature is strongest). This assignment of the rings as discrete ridges of oxide is in agreement with the AFM height map of the pattern, which shows that the rings are 100 nm tall compared to the region between the rings.

Given that Co and Ge exhibit similar patterns after applying RIPPLE, it is conceivable that the patterns form in both materials by the same mechanism. Nevertheless, there are some important differences. The rings of Co oxide are wider than those produced in Ge, but their height to width ratio is about the same (1:20) despite the initial film thickness being the same. There is also an island in the center of the Co pattern, which is observed in Ge patterns. The island is believed to be an artifact caused by the lithography process. Since it contains both Co and O, as apparent from EDS elemental maps (Figure 2.2), it could either be Co oxide (EDS is capable of penetrating surface features.), or residual resist, with Co being protected underneath. The number of rings formed in Co correspond to the number of cycles, which produces one more ring per cycle than Ge. While the oxide rings of Ge patterns are an order of magnitude smaller than the spacing between the rings, the patterns produced in Co have oxide ring widths that are comparable to the spacing widths, but both the spacing and the ring widths become progressively smaller as a function of their radius. In addition, unlike Ge, pH does not change the pattern in Co from rings to steps. This property of Co could be advantageous as an option for fabricating oxide rings onto substrates that cannot be exposed to acidic conditions.

The strategy for optimizing patterning conditions begins with examining the Pourbaix diagram for the material of interest. The Pourbaix diagram allows one to predict the electrochemical conditions required to produce a stable phase of a material. The Pourbaix diagram for Co is shown below (Figure 2.16).

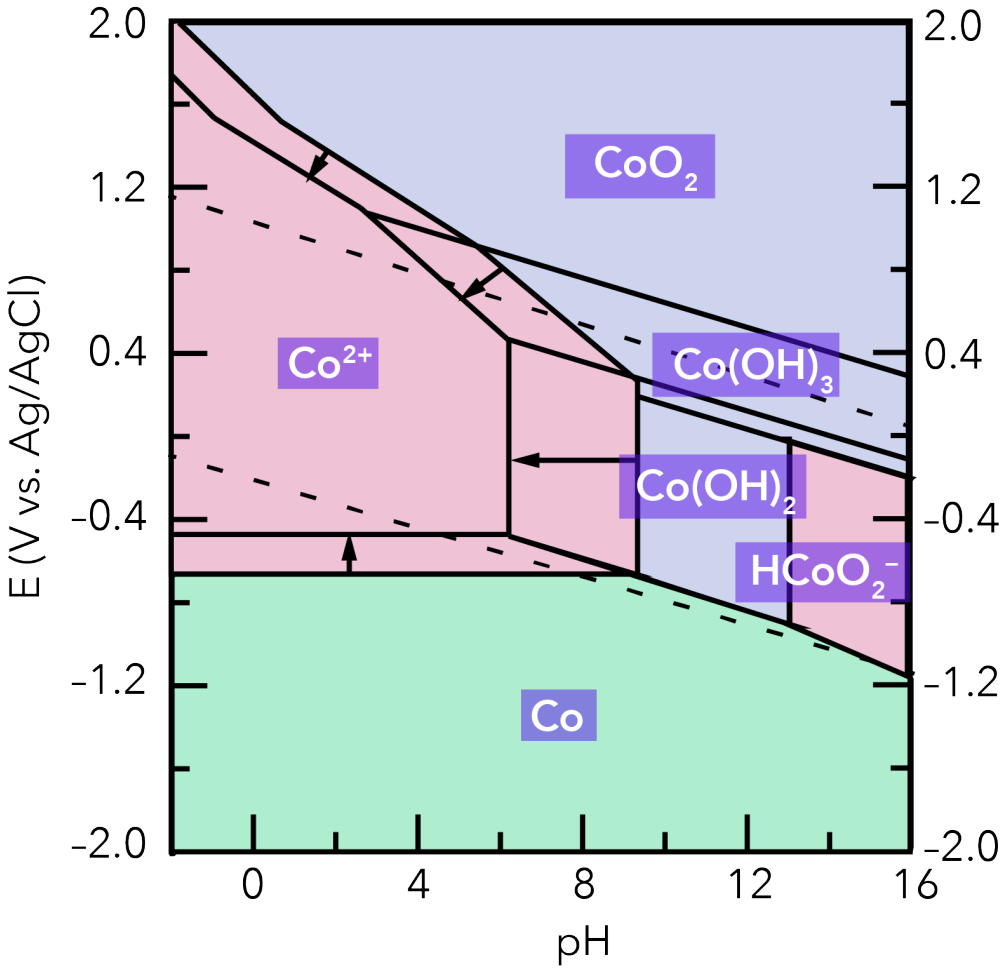


Figure 2.16. Pourbaix diagram for Co in water, 25 °C. Not all species considered. Colors denote theoretical conditions for metallic Co (green), corrosion (red), and passive oxide formation (blue). Arrows represent equilibria shifting as $[Co^{2+}]$ increases from 10 nM to 1 M. Dashed lines mark H_2/H^+ equilibrium (bottom) and H_2O/O_2 (top). Data from Reference 9.

RIPPLE is believed to rely on the conversion of a material from an elemental or neutral state to an oxidized state. This is evident both from the electrochemical procedure used to generate RIPPLE patterns in Ge, which relies exclusively on potentials that are more anodic than the open circuit potential of the metal, and by the identification of the pattern material as an oxide of Ge. It is also likely that the anodic dissolution of the metal is involved in the patterns formation. Thus, to make a Co pattern by RIPPLE, we can select a linear region in the Co Pourbaix diagram that crossed through both dissolved and oxidized Co. The solution was chosen as 0.1 M H_2SO_4 because that is what was used for Ge, but 0.1 M K_2SO_4 was also used because Co metal and Co oxide is known to dissolve under acidic conditions.[9] Under these conditions (pH 1 and 8, respectively), the Pourbaix diagram implies that –0.4 V and 1.6 V would be a sufficient range; however, scanning between these potentials destroys the substrate architecture, presumably due to OER beneath the resist. Decreasing the potentials would seem like a useful strategy, but lower potentials might also drive oxidation too slowly to create any noticeable change in the sample, and in the case of using 0.1 M H_2SO_4, the prolonged exposure to solution causes uncontrolled corrosion. The potentials must therefore be carefully optimized by systematically decreasing and increasing each potential limit to yield the preferred result. After this has been accomplished, a sufficient degree of etching and oxide formation yields a well-defined pattern without incurring gas evolution (Figure 2.2). The success of achieving patterns in Co by RIPPLE not only provides a procedure for making patterns in Co, but also establishes a generic strategy for developing new RIPPLE methods.

2.3.2 Patterning in the presence of chloride

Like Co, RIPPLE patterns of Ni were of interest because of the possibility of being able to pattern Ni-OEC. A challenge in patterning Ni is the formation of a dense passivation layer that prevents dissolution of the metal.[9–11] As can be seen by the Pourbaix diagram for Ni, the passivation causes corrosion to be inhibited, especially at more anodic potentials (Figure 2.17).

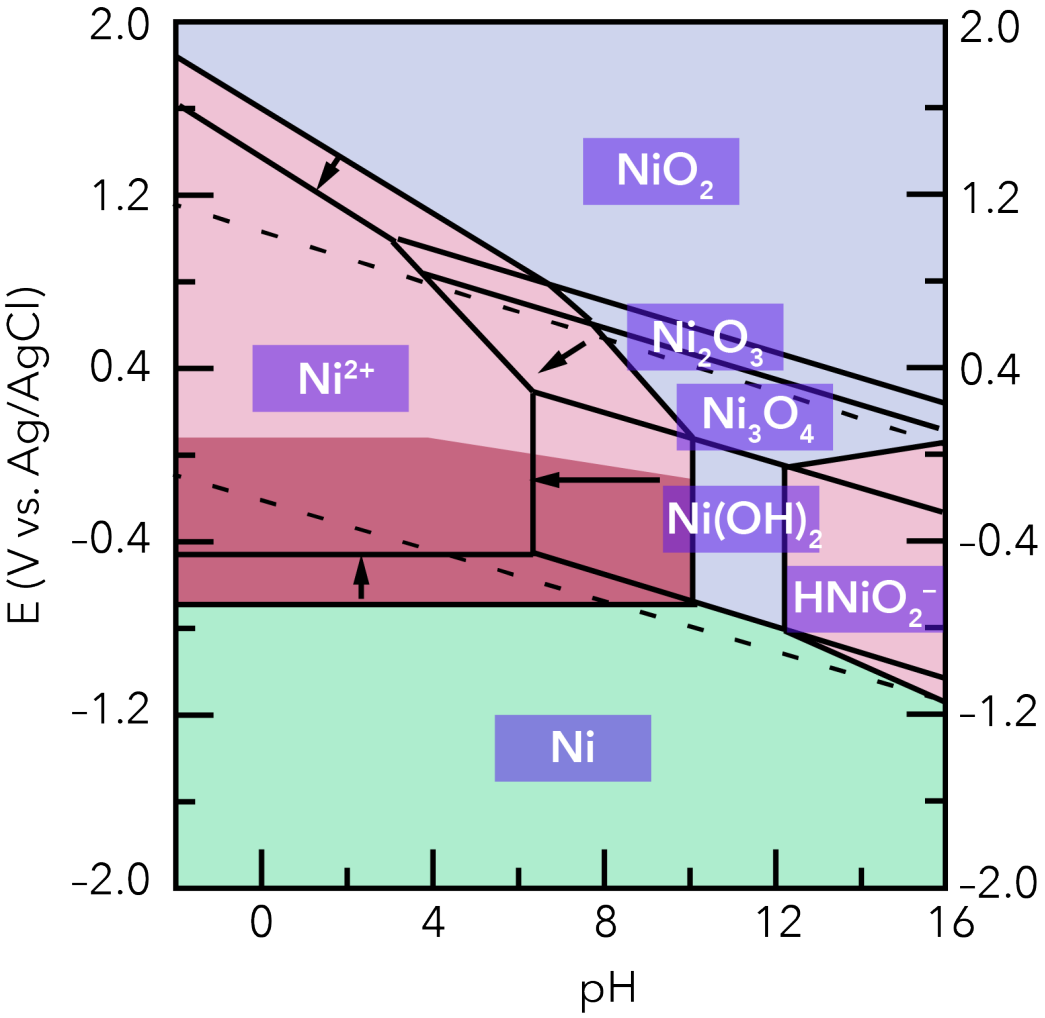


Figure 2.17. Pourbaix diagram for Ni in water, 25 °C. Not all species considered. Colors indicate theoretical conditions for metallic Ni (green), corrosion (red), and passive oxide formation (blue). Dark red region is probable experimental conditions of corrosion in solutions not containing chloride. Arrows represent equilibria shifting as $[Ni^{2+}]$ increases from 10 nm to 1 M. Dashed lines mark H_2/H^+ equilibrium (bottom) and H_2O/O_2 (top). Data from Reference 9.

This behavior of Ni explains the inability to pattern films of Ni metal under the same conditions used to pattern Co, despite Ni having a Pourbaix diagram similar to that of Co (Figure 2.16).

We decided to add chloride, which is a well-known "aggressive ion" towards oxides in corrosion literature.[9–13] The ability of chloride to disrupt the passive oxide layer of Ni is probably due to its single valency, which would preclude an extended structure afforded by the double valency of O^{2-}, although other theories on the mechanism have been discussed in the literature.[11,14–16] Thus, the presence of chloride effectively extends the electrochemical range where dissolution can occur (Figure 2.18).[10]

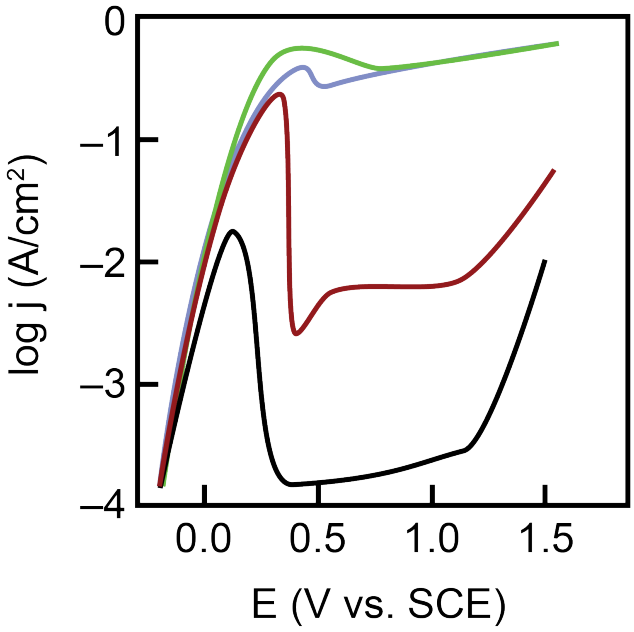


Figure 2.18 The effect of increasing the concentration of chloride for Ni in 0.5 M H_2SO_4 with no chloride (black), 0.1% NaCl (red), 0.5% NaCl (blue), and 3.5% NaCl (green). Data from Reference 10.

Indeed, Ni metal can be dissolved easily in the presence Cl^-, as seen in Figure 2.3. Since Cl^- inhibits the formation of oxide, the oxide rings of the pattern are poorly defined. Attempting to modulate the Cl^- concentration to yield better rings is not an effective strategy, probably be-

cause the occurrence of any appreciable oxide significantly inhibits dissolution of the metal. The Ni film cannot be etched in neutral pH, even with chloride, which indicates that an acid is necessary for oxide dissolution.

To confirm the action of Cl^- on the rings as a general ability of Cl^- to facilitate oxide dissolution, we attempted to pattern Co in 0.5 M KCl. Figure 2.3 shows that Co oxide formation is also prevented by Cl^-, as expected. This observation confirms that Cl^- is not specific towards Ni dissolution, but instead indiscriminately prevents oxides from forming.

2.3.3 Patterning Co films on FTO

The applicability of RIPPLE on rough samples is of interest because of the possibility of applying RIPPLE to inexpensive materials, which may have rough surfaces due to imprecise fabrication methods. Patterning films on FTO and other rough substrates compared to Si wafers allows us to test the tolerance of RIPPLE for imperfections in the substrate's surface. Figure 2.5b exhibits a distinct pattern in the Co-coated FTO after employing RIPPLE, but there is a substantial loss of the fidelity as compared to Co-coated Si. Therefore, RIPPLE is best suited for smooth substrates with a sub-nanometer R_{RMS} when patterning thin (nanoscale) films.

Incidentally, the transparent FTO also reveals the extent to which the film is inadvertently etched. The extent of etching is apparent by the absence of metal visible in Figure 2.5a. The etching that occurs away from the lithographically-created 9 × 9 arrays in each sample is likely due to flaws in the resist that allow solution to access the film. It could also be due to resist deformation during the oxidation process.

2.3.4 Patterning electroplated Co

The electroplated Co system represents a scalable substrate architecture, considering that the electroplating of Co metal is a low-cost and simple process that has been well established for over two centuries. This system is also significantly disordered, with a high R_{RMS} underlying substrate (FTO) and a polycrystalline structure in the metal (Figure 2.6). Interestingly, using the same procedure that was used to fabricate the e-beam evaporated samples, it was possible to pattern electroplate Co (Figure 2.7). Moreover, the patterns formed by RIPPLE in electroplated Co have similar aspect ratios as those formed in e-beam evaporated films, despite a difference in film thickness by a factor of four. We thus surmise that thick films are better suited for making patterns over coarse substrates.

A remarkable feature of the electroplated Co pattern is the preservation of platelet structure in the oxide rings (Figure 2.7). If the rings were formed by deposition of the dissolved metal, we would expect the rings to be amorphous and lose their polycrystalline structure. The oxidized platelets imply that deposition is not important to the patterns' formation, thereby providing some insight into the mechanism of pattern formation. The mechanism of pattern formation will be further discussed in Part 3.

FIB cross sections of this sample show that a layer of Co oxide up to 100 nm thick remains between the oxide rings (Figure 2.8). This is not ideal because the rings are not isolated, which limits the use of RIPPLE with regard to fabrication purposes. On the other hand, the remaining Co oxide might be due to the excessive thickness of the electroplated Co film, which may be corrected for by adjusting the film thickness.

2.3.5 Oxygen evolution on RIPPLE patterns

The ability to pattern large substrate areas with metal and oxidic structures suggests the potential for integrating inorganic catalysts with semiconductors for energy conversion applications. We therefore turn our attention to patterning Si substrates, such as those used for PVs, with the efficient Co oxide water splitting catalyst, Co-OEC.[7]

The drop in current during anodization at 0.85 V was interpreted as the complete oxidation of the Co film (Figure 2.9a). (This is probably not the case, and will be revisited in Part 6.) SEM and EDS show that anodization after 30 min at this potential does not alter the pattern (Figure 2.9b), and the CV is evidence that Co-OEC is present (Figure 2.9c). These results signal that the patterned substrate is capable of OER catalysis. As anticipated for Co-OEC, an oxygen probe experiment carried out over 10 hr using the patterned substrate verified the functionality of this catalyst toward O_2 generation from water with a quantitative Faradaic efficiency (Figure 2.10a).

Over the course of electrolysis at 1.0 V for 24 hr, the pattern undergoes a significant change, with a film identified as Co oxide (from EDS) forming over the pattern (Figure 2.11). Cracks in this film, probably caused by the vacuum in the SEM chamber and dehydration of the oxide, show that rings are still intact below the film. We speculate that the thin film of Co oxide is due to migration of Co oxide during electrolysis. The question of how and if Co-OEC can migrate during OER is relevant to devices in general that seek to pattern OER over an electrode. We will revisit the question of Co-OEC mobility in Part 6.

2.3.6 Reducing Ge and Co patterns.

A shortcoming of the RIPPLE method is that it is only capable of directly generating rings of oxide. The capability of generating rings of elemental Ge, for instance, would be useful because we could then consider applications for patterned semi-conductor light absorbers. To overcome this limitation, we have attempted to reduce oxides in the presence of H_2. We initially employed a tube furnace with the aim of thermally reducing the oxide rings of a pattern in Ge. However, this caused the oxide rings to break apart and ultimately deteriorated the pattern, perhaps due to the elevated temperature. As a gentler approach, we propose a post-processing strategy that reduces the oxide rings using the H_2 plasma generated by PECVD. Ge and Co patterns were successfully reduced by PECVD, as evident by a decrease in O signal relative to total O counts as compared to the decrease in Ge and Co signal relative to the total counts for each element (Figures 2.13 and 2.15). The removal of O from the rings is also readily apparent from the EDS maps in Figures 2.12 and 2.14. SEM images of the patterns after PECVD display rings that are fully intact (Figures 2.12 and 2.14). An increase in F is attributed to octafluorocyclobutane, which is used as a thermal conductor to ensure the sample remained at 200 °C. Apparently, the thermal carrier infused into the porous rings.

The ability to reduce the oxide while maintaining the structure of the ring is attributed to lower temperature (200 °C) used in PECVD as compared to thermal reduction (>600 °C). While we now possess the ability to pattern rings of Ge and Co metal, there are still two disadvantages to this technique. For one, the entire process now demands PECVD, which increases the overall cost and complexity of fabrication. In addition to this drawback, the reduced rings

also appear by SEM to lack the crystallinity of the original materials, so the semi-conductor qualities are not anticipated to be usable for light absorption applications.

2.4 Conclusion

We have established a procedure to pattern other materials beyond Ge by RIPPLE. The results above validate that patterns containing concentric rings of oxide can be generated in films of Co and Ni metal. We have also provided a general strategy for developing procedures for patterning novel materials by RIPPLE. Patterning Co also allowed us to test RIPPLE as a means of patterning OER catalysts. Anodized Co patterns appear to behave as Co-OEC during electrolysis, which confirms that oxide OECs can be patterned directly by RIPPLE.

While we were able to form rings in Ni films, a Cl^- concentration of not less than 0.5 M was required, which in turn eroded the features of the pattern. The role of Cl^- in the patterning of Ni is to penetrate an oxide passivation layer, which likewise causes the passivated oxide rings of the Co pattern to also diminish in the presence of Cl^-.

The roughness of the substrate was shown to affect the fidelity of RIPPLE patterns, particularly for thin films. A thicker electroplated film of Co, however, exhibited surprisingly distinct rings of oxide that retain the structure of the original electroplated metal. Patterning electroplated materials will allow RIPPLE to be applicable to metal films that are deposited by an inexpensive method.

Lastly, PECVD afforded a means of reducing the oxide rings while retaining their geometries. Patterning materials in this fashion, however, would be impractical due to the loss in crystallinity of the post-processed metal and also due to the elaborate nature of the entire process.

2.5 Experimental Methods

2.5.1 Substrate preparation

Samples prepared on Si substrates were fabricated by etching 4" p-type Si wafers (B-doped, <100>, 1-10 Ω-cm, Nova Electronic Materials) in 7:1 buffered oxide etch (BOE, J.T. Baker) and rinsing with Type I water water 30 s immediately before use. A 300 nm layer of Pt was deposited by electron-beam evaporation onto a p-Si chip to protect the surface from oxidation using an automated instrumented to determine voltage and current parameters for a 2 Å/s deposition rate. Co and Ni thin films (100-500 nm) were grown by loading a recently-etched p-type Si 4" wafer and a crucible of Co or Ni metal pellets (⅛" × ⅛" dia., 99.95%, Kurt J. Lesker) into the chamber of a Sharon electron beam vapor deposition system. The chamber was evacuated to 1 μTorr. The crucible was gradually heated over 1 h by slowly increasing the current until it reached 60 mA at 10 kV for Co or 100 mA at 11.48 kV for Ni. A shutter was opened to allow growth of a desired film thickness on the p-Si, while monitoring film growth with a piezoelectric quartz crystal. (At first, a protective layer of Pt was coated onto the Si before Co to ensure conductivity under oxidizing conditions, but this step ultimately proved to be unnecessary.) Films of Co were also deposited into FTO substrates following this method.

Ge films (p-doped) were prepared on Si substrates for the PECVD experiments. The substrates were etched for 10 s in buffered hydrogen fluoride and then inserted into a home-built chemical vapor deposition (CVD) reactor, which was evacuated to a base pressure of 5.4 mTorr. A poly-crystalline p-type Ge film was grown initially at 360 ℃ for 3 min and then at 330 ℃ for another 30 min. The growth pressure was 28 Torr with flow rates of 10, 14 and 100 standard cubic centimeters per minute (sccm) for germane (GeH_4), diborane (B_2H_6, 100 ppm

in He) and hydrogen (H_2, Semiconductor Grade), respectively. The film growth rate under these conditions was ~7.5 nm min^{-1} for a total film thickness of ~250 nm.

Electroplated Co was deposited potentiostatically –1 V from baths containing 0.29 M potassium citrate and 0.36 M $CoSO_4$ (pH 5.0).[3] A total 120 C/cm^2 was necessary to deposit a film approximately 1 μm thick, as determined from SEM of a FIB cross-section and AFM. The film was deposited under high stirring to remove hydrogen form the electrode, while alternating the potential from open circuit to –1 V with a –0.6 V preelectrolysis step every 10 C/cm^2.

The surface was masked by spin-coating 950PMMA C4 resist (MicroChem) over the Co film at 4000 rpm for 4 min and then heating the substrate to 185 °C over 4 min. An electron-beam writer (JOEL-7000) was used to define a square 9 × 9 array of 2 μm × 2 μm square openings in the PMMA. The openings were spaced 80 μm from the nearest neighbor. The PMMA was developed for 45 s in 1:3 MIBK:IPA developer (MicroChem) and soaked in IPA (99.5%, Sigma Aldrich) for 45 s. Resist thickness and opening dimensions were confirmed by AFM. The back of the sample (p-Si) and the sample edges were then coated with stop off lacquer (MICCRO Products). Resist and lacquer were removed post-patterning by immersing the sample in acetone (99%, Sigma Aldrich) for 2 min, then IPA for 1 min.

2.5.2 Electrochemical methods

A two-compartment (50 mL compartments separated by a glass frit of medium porosity) electrochemical cell was filled with 0.1 M H_2SO_4 or 0.1 M K_2SO_4 (99.0% min, Alfa Aesar) and the sample was suspended vertically in one compartment. Type I water (EMD Millipore, 18.2 MΩ-cm) was used to prepare solutions. The pH of 0.1 M K_2SO_4 solution was unadjusted

(measured as pH 8.4). Standard three-electrode cyclic voltammetry experiments were conducted using a Ag/AgCl reference electrode (BASI), a Pt mesh counter electrode, and potentiostat (760D series, CH Instruments Inc.). After concluding the cyclic voltammetry, the resists and lacquer were removed by soaking in acetone for ~1 min followed by a 10 s rinse in isopropanol. For Ge patterning, scans were initiated at the open circuit potential, which was 0.1 V. For the data shown in Supplementary Figure 3, a 0.1 M sodium sulfate solution was used. All electrolytes were prepared from reagent grade chemicals and type I water (18 MΩ resistivity).

2.5.3 Catalyst Preparation and Characterization.

The patterned cobalt was oxidized to the CoP_i catalyst at 0.95 V for 30 min in 0.1 M KPO4 (pH 7.0), at which point steady-state was observed. Faradaic efficiency was calculated using a fluorescent oxygen sensor (Ocean Optics) in a gas-tight electrochemical cell. The solution and headspace were purged with N_2 for an hour and the sensor was placed in the headspace. Electrolysis was performed at 1.0 V (vs. Ag/AgCl) in 0.1 M KPO4 (pH 7.0) for 10 h.

2.5.4 Plasma reduction.

Patterns formed using RIPPLE on films of e-beam evaporated Co and Ge were loaded into a STS parallel plate electrode plasma enhanced chemical vapor deposition (PECVD) system. A stable plasma was achieved by setting the Ar flow rate to 150 cm^3/min and the H_2 flow rate to 250 cm^3/min. The high frequency plate was set to 13.56 MHz and the low frequency plate was set to 380 kHz. The sample was exposed to direct-ion bombardment for 3 hrs. The sample temperature was cooled to 200 °C using octafluorocyclobutane.

2.5.5 Microscopy.

SEM micrographs were acquired using the InLens and SE2 detectors on a Zeiss Supra55VP (Carl Zeiss AG) operating at 3 kV. EDS maps were acquired on an SEM operating at 14 kV with 60 μm aperture size and WD = 8.5 mm. Topographic maps were acquired using an MFP-3D AFM (Asylum Research) with an Al coated Si AFM tip (f ~ 300 kHz, AC160TS). Data were acquired in AC mode. Using the Asylum software package, a 1^{st} order Flatten procedure was applied to the raw data to correct for a mild distortion of the substrate plane. For the AFM maps in Figure 1e, a N×N median filter (size = 1) was applied as was the "Mocha" color table for the z- axis data (Asylum software).

The FIB axial cross-sections cross-section of the electroplated Co pattern was prepared by Ga^{+} focused ion-beam milling (Zeiss NVision 40, Carl Zeiss AG). To protect against subsequent FIB damage, the sample was first coated with a ~50 nm thick carbon film inside the FIB under SEM mode followed by ~550 nm of Pt under FIB mode. FIB milling was used to excise a wedge from the substrate and was followed by FIB welding of the wedge to a nano-manipulator needle with tungsten. The wedge was subsequently transferred and welded to a specialty Cu TEM grid.

2.6 References

(1) Badawy, W. A.; Al-Kharafi, F. M.; Al-Ajmi, J. R. *J. App. Electrochem.* **2000,** *30,* 693–704.

(2) Degarmo, E. Paul; Black, J.; Kohser, Ronald A. *Materials and Processes in Manufacturing* 2012, 11th ed., Wiley: Hoboken, NJ.

(3) Abd El Rehim, S. S.; Abd El Wahaab, S. M.; Ibrahim, M. A. M.; Dankeria, M. M. *J. Chem. Technol. Biotechnol.* **1998,** *73,* 369–376.

(4) Gomez, E.; Valles, E. *J. App. Electrochem.* **2002,** *32,* 693–700.

(5) Li, N. C.; Lindenbaum, A.; White, J. M. *J. Inorg. Nucl. Chem.* **1959,** *12,* 122–128.

(6) Young, E. R.; Nocera, D. G.; Bulovic, V. Energy Environ. Sci. **2010,** *3,* 1726.

(7) Kanan, M. W.; Nocera, D. G. *Science* **2008,** *321,* 1072.

(8) EDAX Interactive Periodic Table of Elements. http://www.edax.com/periodic-table/index.aspx (accessed on May 8, 2017).

(9) Pourbaix, M. *Atlas of Electrochemical Equilibria in Aqueous Solutions;* Pergamon Press: Oxford, 1966.

(10) Gileadi, E. *Electrode Kinetics for Chemists, Chemical Engineers, and Materials Scientists;* VCH: New York, 1993; p 513 – 519.

(11) Hoar, T. P. *Corr. Sci.* **1967,** *7,* 341–355.

(12) Jung, H.; Alfantazi, A. *Electrochim. Acta* **2010,** *55,* 865–869.

(13) Abd El Rehim, A. A.; El Basosi, A. A.; Osman, M. M. *J. Electroanal. Chem* **1993,** *348,* 99–106.

(14) Barbosa, M. R.; Bastos, J. A.; García-Jareño, Vicente, F. *Electrochim. Acta* **1998,** *44,* 957–965.

(15) Hsu, Y. S.; Wu, J. K. *J. Mat. Sci. Letters* **1987,** *6,* 1246–1250.

(16) Chevalet, J.; Žutić, V. *Electroanal. Chem. Inter. Electrochem.* **1973,** *44,* 411–423.

Part 3. Development and mechanistic studies of a binary potential step patterning method

Portions of this chapter have been published:
Jones, E. C.; Liu, Q.; Suo, Z.; Nocera, D. G. *ACS Nano*, **2016,** *10,* 5321–5325.

3.1 Introduction

RIPPLE, as it is described in our first publication, relies on CV to generate patterns of concentric rings. In using CV and linearly scanning across a voltage window, we induce varying fluxes and also potentially introduce unnecessary processes or intermediates within each scan. These complexities, which present challenges in defining the mechanism of RIPPLE, are mitigated by toggling between the potential limits of the CV experiment using a binary potential step method. The binary potential step patterning method proposed is essentially a square wave function in series with a lower potential, as compared to the triangular function of a CV.[1,2]

There are several benefits that arise from using a binary potential step function. For one, by distilling the patterning process into just two steps, we can alter the radius and width of each ring in the pattern by changing the durations of the potential steps. Therefore, the pattern geometry is effectively programmable. Using such a voltage profile also allows us to provide robust initial conditions for a scaling analysis. Comparison of observed patterns to those predicted by the scaling analysis furnishes insight into the mechanism of patterning by RIPPLE. Understanding how the bull's-eye patterns are formed will be useful for developing our ability to distribute oxides over substrates using electrochemistry. With these advancements, we hope to gain the ability to refine the patterns as plasmonic waveguides[3,4] or adjust the distribution of Co-OEC over a substrate to optimize the performance of a PEC.[5,6]

3.2 Results

3.2.1 Patterning Co by a binary potential step method

A binary-potential step method, depicted in Figure 3.1a, was used to generate patterns from Co metal overlaid on Si by alternating between two discrete potentials. These experiments were conducted with p-doped Si substrates coated with a 250 nm Co film, which was masked by

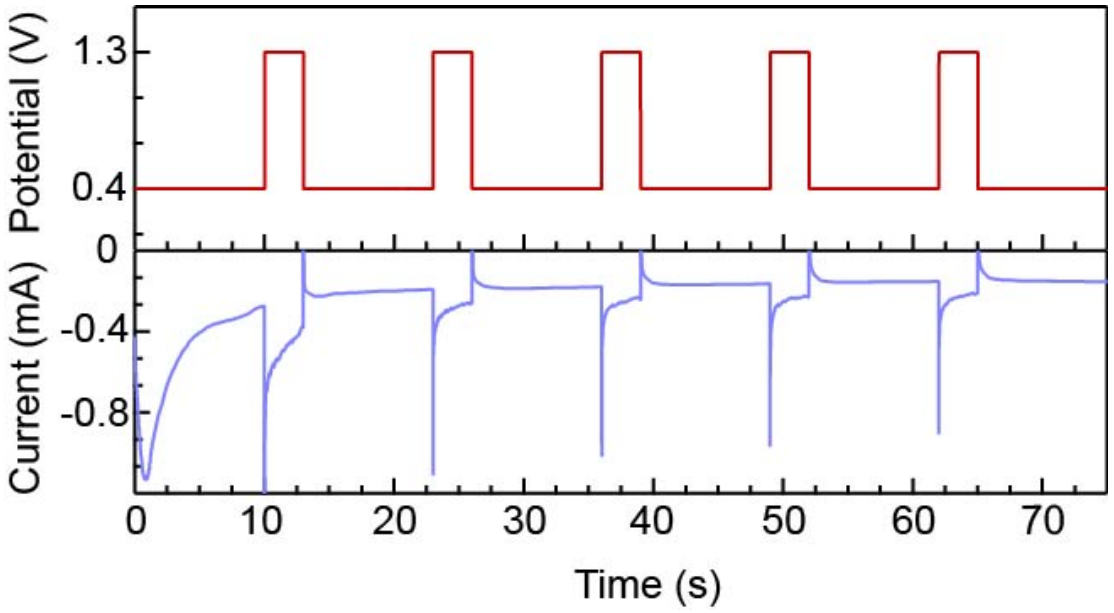


Figure 3.1. (top) Potential–time view and (bottom) corresponding current-time view of a binary-potential step method for patterning cobalt in 0.1 M K2SO4.

poly(methyl methacrylate) (PMMA) e-beam resist, as previously described.[6] The mask contains a 9 × 9 array of 4 μm^2 square openings. The sample was suspended in 0.1 M K_2SO_4 and subjected to 10 potential steps (all potentials are reported vs Ag/AgCl) of 0.4 V (applied for 10 s) and 1.3 V (applied for 3 s), which correspond to the CV scan limits previously used to pattern Si with Co oxide by RIPPLE.[6] As shown in Figure 3.2, concentric rings are produced. AFM shows that the ridges are 1.4 μm wide and 130 nm tall. EDS elemental maps indicate that the ridges are

composed of Co and O. The gaps between the rings and ring thicknesses are attenuated as a function of distance from the pattern's center. By modulating the durations of the 0.4 V and 1.3 V steps, the spacing between rings and the ring widths were adjusted, respectively (Figure 3.3). In addition, the duration of each potential was proportional to the width of the feature.

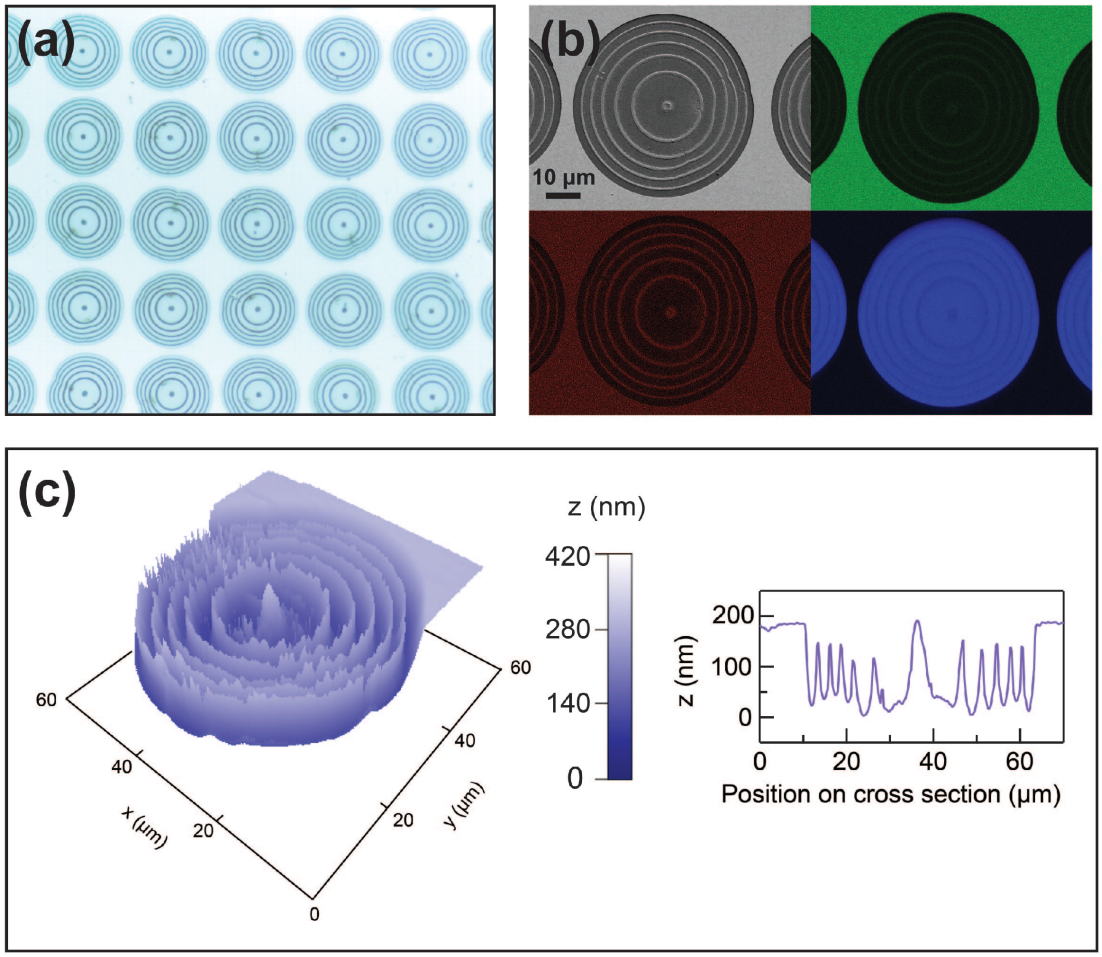


Figure 3.2. Patterns formed in a Co film by alternating between 0.4 V (10 s) and 1.3 V (3 s) 10 times in 0.1 M K_2SO_4. (a) Optical microscope images at 50× magnification. (b) SEM image (top left) and EDS elemental maps of cobalt (green), oxygen (red), and silicon (blue). (c) AFM map with height-profile of a diametric cross section (inset on right).

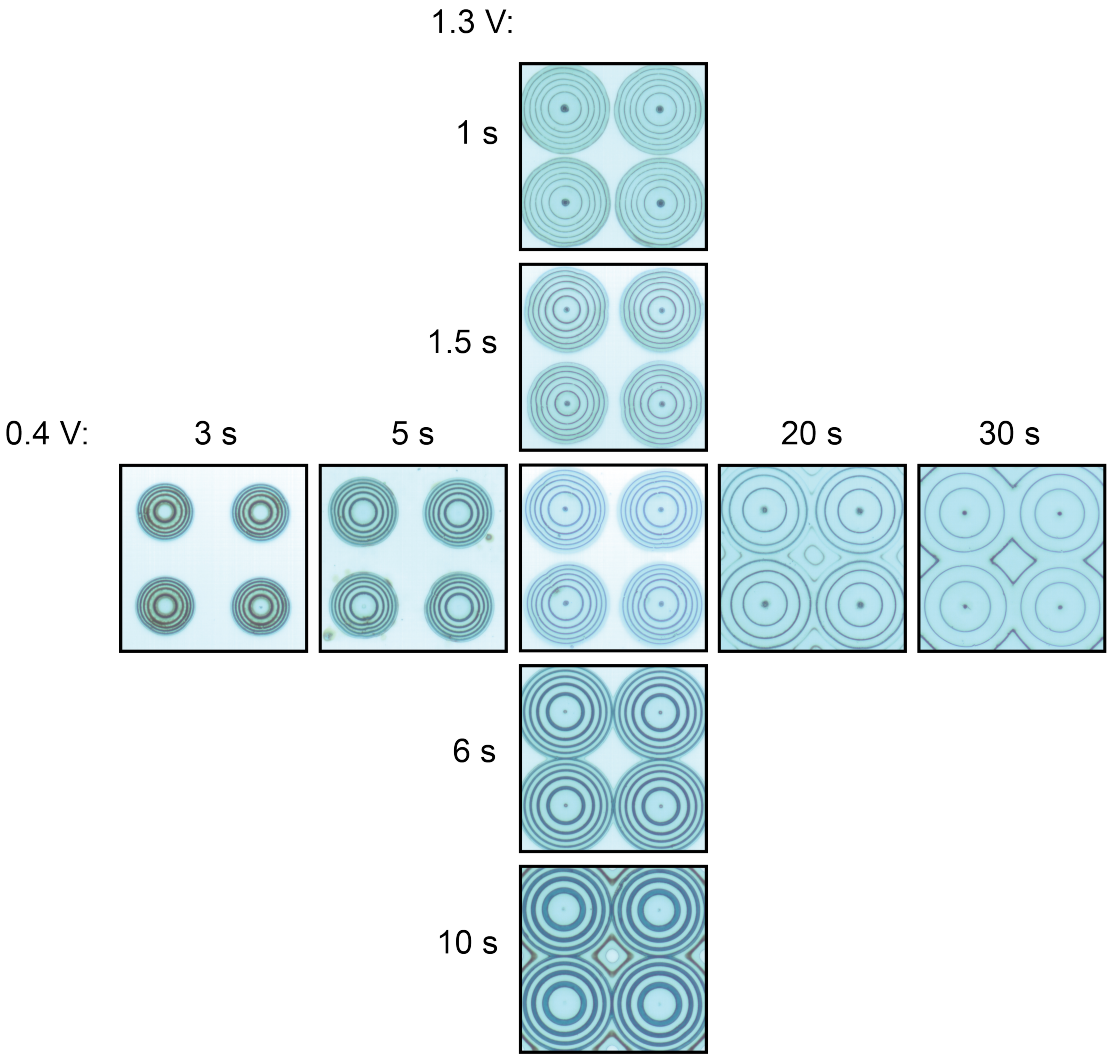


Figure 3.3. Dependence of Co pattern geometry on potential duration for five applications of the two-potential sequence, 0.4 V and 1.3 V, followed by one application of 0.4 V. To determine the effect of the duration of 0.4 V, 1.3 V was held for 3 s for each application and 0.4 V was held for the specified time indicated over each image (horizontal row). Similarly, 0.4 V was held at 10 s each application and 1.3 V was held for the time identified at the left of each image (vertical column). The center image shows both potentials held for 3 s. Samples imaged at 50× magnification.

By exploiting the dependence of the pattern geometry on the duration of the potential steps, we formed patterns with uniformed gap and ring dimensions by sequentially increasing the duration of each step to compensate for the decreasing spacing between rings. Patterns containing rings 3.0 μm in width and with 3.8 μm spacing, shown in Figure 3.4, were generated for binary potential steps held for 5, 7, 9, 12, and 15 s.

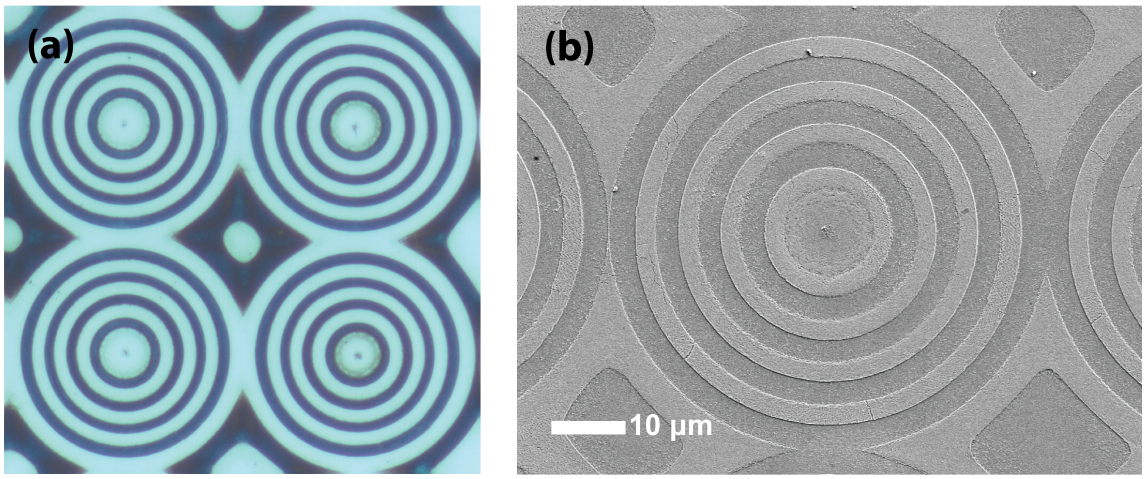


Figure 3.4. Patterns in Co with conserved radial dimensions formed by sequentially increasing potential step durations in 0.1 M K_2SO_4. Images from (a) optical microscope with 50× objective and (b) SEM.

3.2.2 Correlating applied potential to pattern evolution

The potential binary step method was applied to a film of Co and surveyed by *in situ* optical microscopy. A video recording of the pattern formation by alternating between 0.4 V (10 s) and 1.3 V (3 s) 10 times was synchronized to the applied potential and current so that the evolution of a pattern could be observed through optical microscopy (Figure 3.5). A bright-contrasted circle expands from the opening for the first 10 s, followed by 3 s upon which a dark ring propagates into the surrounding film.

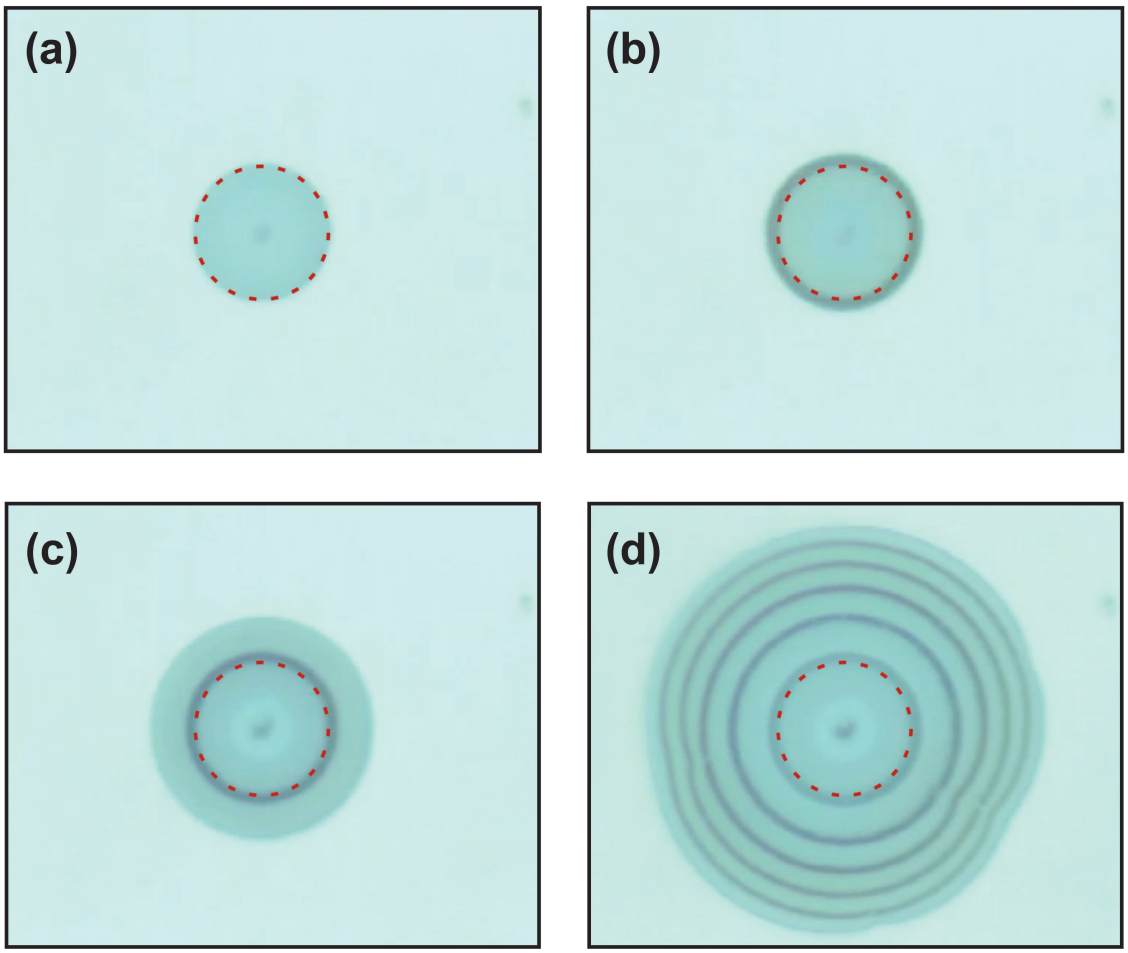


Figure 3.5. Evolution of the same Co pattern generated by alternating between 0.4 V (10 s) and 1.3 V (3 s) ten times (graphically described by Figure S1). (a) After 10 s, (b) 13 s (c) 23 s, and (d) the final pattern (75 s). Red dashed-circle corresponds to the etch front after applying 0.4 V for 10 s. Sample imaged at 63× magnification using water immersion objective.

3.2.3 Patterning Ge by a binary potential step method

Figure 3.6a shows a binary potential step method consisting of five repetitions of 0.4 V (20 s) followed by 1.1 V (20 s). The EDS map for O reveal a circle of O at the center of a pattern with four rings containing O surrounding it (Figure 3.6b). Reversing the order of low and high potentials resulted in five discrete rings akin to the pattern generated in Co in Figure 3.2, with the last ring at the perimeter of the pattern (Figure 3.6c,d).

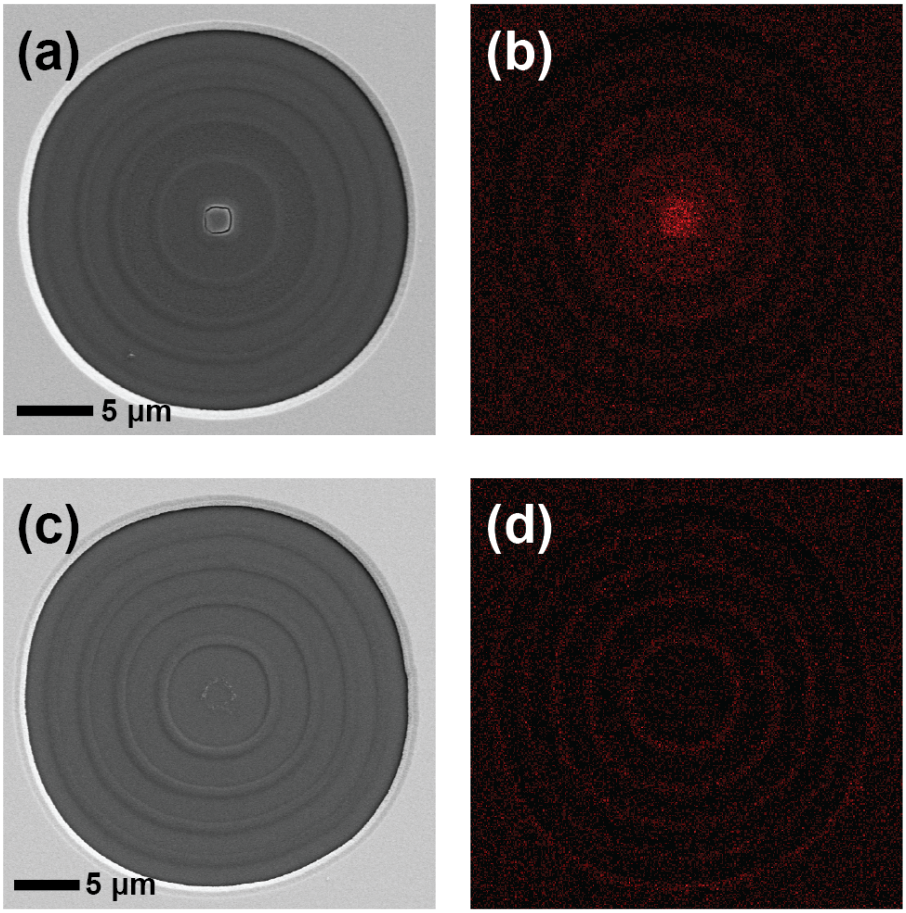


Figure 3.6. Patterns formed in a Ge film by altering between 0.4 V and 1.1 V in 0.1 M K_2SO_4. (a) SEM micrograph of a pattern after five repetitions of the sequence 0.4 V (20 s) followed by 1.1 V (20 s). (b) EDS map for O of (a). (c) SEM micrograph of a pattern after five repetitions of the sequence 1.1 V (20 s) followed by 0.4 V (20 s) (reverse of (a)). (d) EDS map for O of (c).

We then examined the dependence of Ge patterns on the duration of the low and high potentials (Figure 3.7). Increasing the 0.4 V steps causes the dark rings to thicken, while increasing 1.1 V steps causes the spacing between the dark rings to widen.

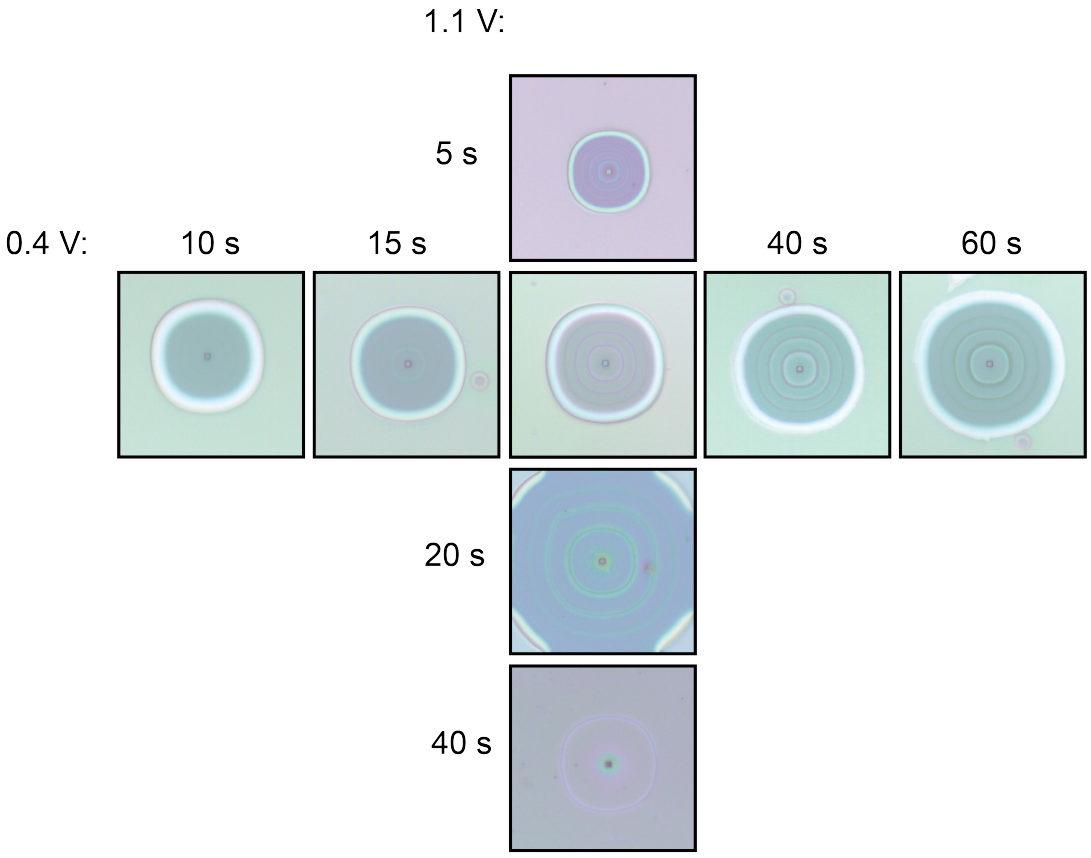


Figure 3.7. Dependence of Ge pattern geometry on potential duration for five applications of the two-potential sequence, 1.1 V and 0.4 V, followed by one application of 1.1 V. To determine the effect of the duration of 0.4 V, 1.1 V was held for 20 s for each application and 0.4 V was held for the specified time indicated over each image (horizontal row). Similarly, 0.4 V was held at 20 s each application and 1.1 V was held for the time identified at the left of each image (vertical column). The center image shows both potentials held for 30 s. Samples imaged at 50× magnification.

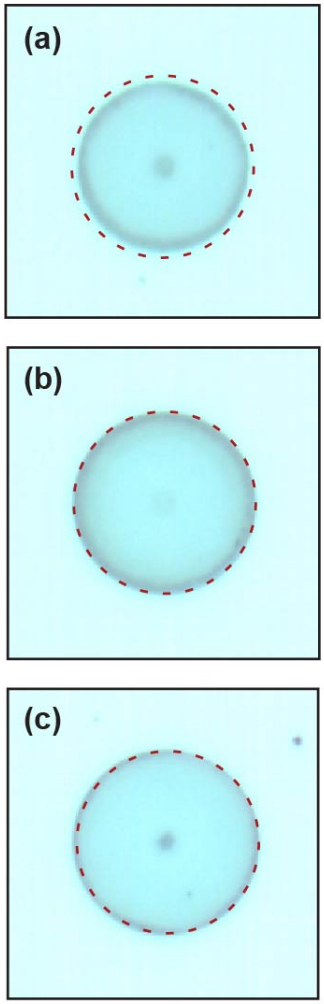


Figure 3.8. Application of (a) 0.2 V, (b) 0.3 V, and (c) 0.4 V for 10 s. Red dashed-circle corresponds to the etch front after applying 0.4 V for 10 s. Sample imaged at 50× magnification.

3.2.4 Investigating the influence of Co^{2+} under the resist

To determine whether the etch front is kinetically or activation limited, we tested the effect of potential on the etching rate of Co. Etch fronts, which form at the openings of masked Co films during the binary potential step patterning method, were reproduced by applying a 10 s step of 0.2 V, 0.3 V, or 0.4 V to masked Co films suspended in 0.1 M K_2SO_4 (Figure 3.8). The etch fronts were similar in diameter for all three potentials.

We also examined how diffusion affects the oxide rings. First, etch fronts were generated at Co films by way of a 30 s step of 0.4 V. A 20 s step of 1.3 V was then applied immediately after the 0.4 V step (Figure 3.9, left column) and after a 30 min delay following the 0.4 V step (Figure 3.9, right column). SEM and EDS show that identical layers containing Ge and O are formed at

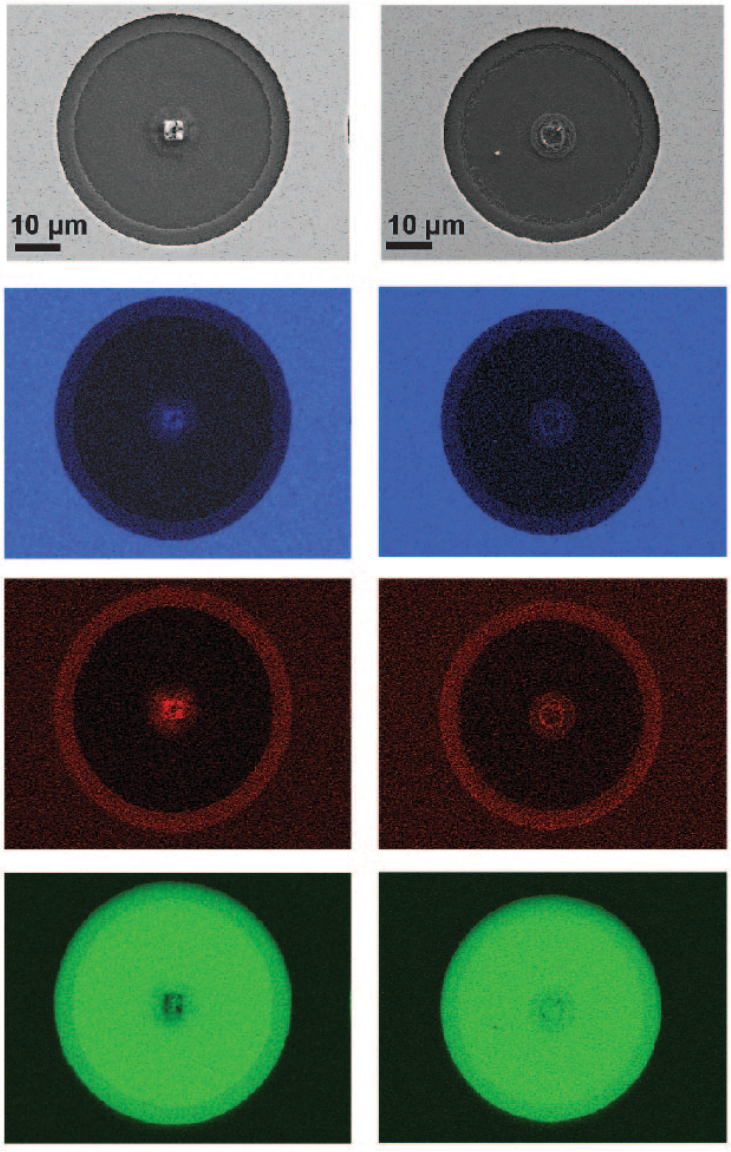


Figure 3.9. Applying 0.4 V over 30 s, followed by 1.3 V over 20 s successively (left column) and after a 30 min delay at open circuit (right column). SEM images (grey) and EDS maps for cobalt (blue), oxygen (red), and silicon (green).

the parameter of the etch front regardless of whether there is a 30 min delay before the application of 1.3 V.

3.2.5 Modeling Co diffusion and ring spacing

An axisymmetric cross section of an etch front, depicted in Figure 3.10a, was modeled by a finite element simulation using COMSOL software. Figure 3.10b shows that the concentration of Co^{2+} at the opening is about an order of magnitude lower than its concentration at the etching front. It also predicts that the concentration of K^+ is very low so that the concentration of SO_4^{2-} roughly equals the concentration of Co^{2+}. Note that the concentration of Co^{2+} at the open-

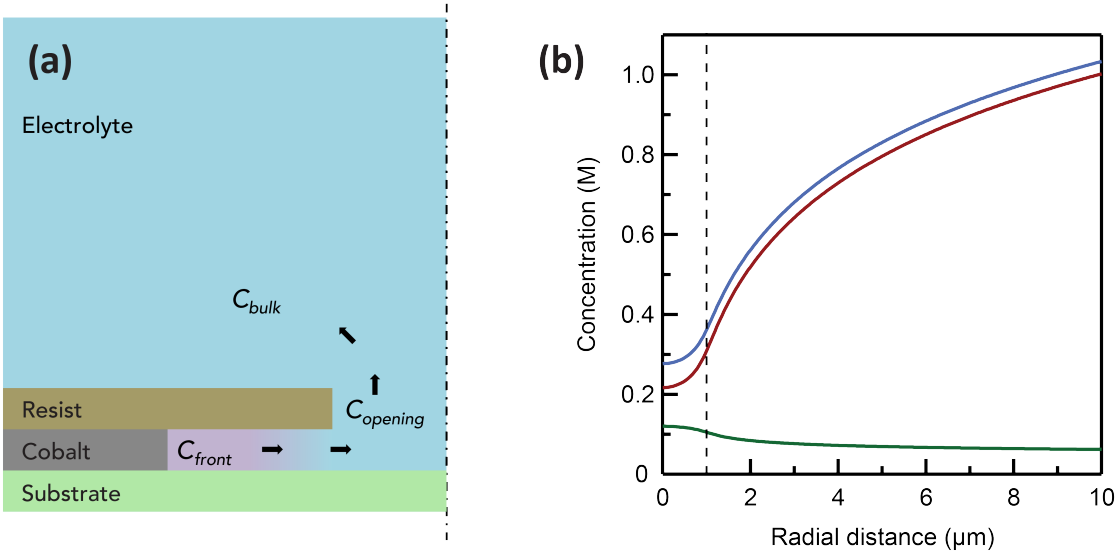


Figure 3.10. (a) A schematic showing the diffusion from the etching front to the bulk electrolyte. Arrows schematically indicate the diffusion flux of Co^{2+}. Cross section is axisymmetric around the dash-dotted line. (b) Finite element simulation for the steady state concentration distribution of Co^{2+} (—), $SO4^{2-}$ (—), and K^+ (—) under the resist. Dashed black line marked the edge of the opening.

ing is about an order of magnitude lower than its concentration at the etching front. The concentration of K^+ is very low so that the concentration of SO_4^{2-} roughly equals the concentration of Co^{2+}.

A finite elemental simulation was then calculated for the ring spacing in a pattern generated in a masked Co film using a binary potential step method (see discussion for details). The model predicts the spacing between the oxide rings to decrease as a function of ring radius (Figure 3.11). This ring arrangement is also observed in the pattern of Figure 3.2.

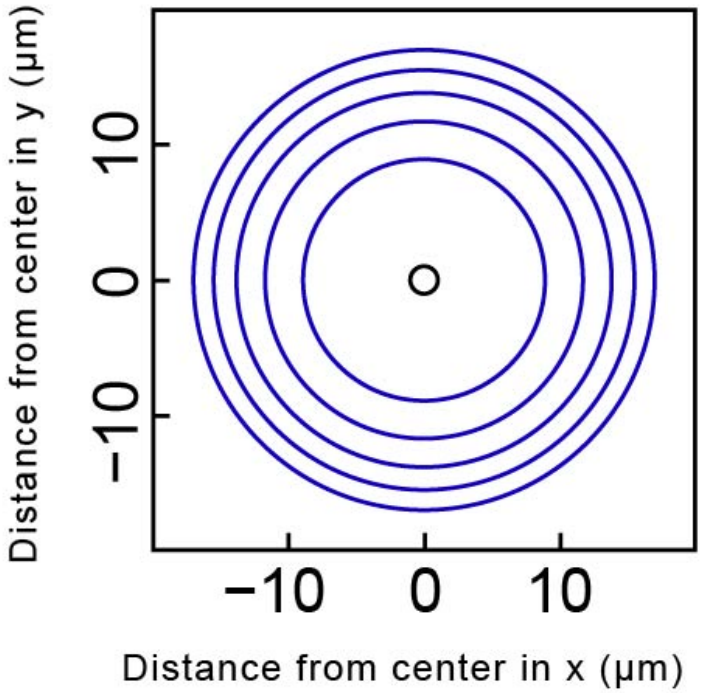


Figure 3.11. Predicted ring spacing from finite-element simulations. Ring positions (blue) relative to a 1 μm-diameter circular opening (black). Note ring spacing decreases with increasing distance from the opening.

3.3 Discussion

3.3.1 Developing a binary potential step method for RIPPLE-like patterning of Co

The current profile of the binary potential step method contains spikes at the beginning of each step (negative-facing for 0.4 V steps and positive facing for 1.3 V steps), which are likely due to double-layer charging (Figure 3.1b). These spikes then decrease to a constant value over the duration of the step, as is expected for an electrochemical process approaching steady state. The patterns generated by the binary-potential step are comparable to those generate by the CV-based RIPPLE method with regard to both ring definition and spacing (Figure 2.2). This validates the use of the binary potential step method as an alternative to the CV approach used in RIPPLE. Substituting the CV step of RIPPLE with a binary potential step method reduces the electrochemical conditions from an large indefinite number (as many potentials between the bounds of the CV as the resolution of the potentiostat permits) to two conditions, which are chosen as the lower and upper limits of the RIPPLE CV method.

The correlation between ring spacings and ring widths with the duration of the low or high potential steps, illustrated in Figure 3.3, implies that at 0.4 V, the etching of Co metal occurs, while at 1.3 V, an oxide layer is formed. This result is an important insight into the mechanism of pattern formation, and also shows that potential steps could be programmed to control the geometries of the Co oxide pattern. To demonstrate this correlation, patterns with uniformed gap and ring dimensions were formed by sequentially increasing the duration of each step (Figure 3.4). While our demonstration is used to create rings with consistent aspect ratios, it is possible to generate any permutation of ring widths and spacings, opening up pattern designs that require rings of varying specific dimensions. If constant durations are used for the

steps, however, the normal progression of the pattern will attenuate the ring spacing, as observed in the CV method.

3.3.2 Co redox behavior under patterning conditions

To delineate the correlation between applied potentials and the patterning process, the pattern was surveyed by *in situ* optical microscopy (Figure 3.5). The AFM height and EDS maps in Figure 3.2 indicated that the bright-contrasted circle and surrounding bright-contrast rings correspond to regions where Co was removed and the dark-contrasted rings correspond to Co oxide. These results are in agreement with the assignment to an etching process at 0.4 V and metal oxide formation at 1.3 V. With consideration to the Pourbaix diagram of Co, the reaction during etching at 0.4 V in 0.1 M K_2SO_4 corresponds to the two-electron oxidation of Co^0 to a soluble Co^{2+} ion or $CoO(OH)^-$ (Figure 2.16).[7]

3.3.3 Comparing patterns formed in Co and Ge

We chose to extend the redox-induced rational for patterning to Ge, which was the material that was first used to discover RIPPLE, in order to test the generality of the Co patterning mechanism described in the foregoing section (3.3.2).

We started by developing a binary potential step method for patterning Ge. Figure 3.6a shows the binary potential step method that was used to create a clean pattern in Ge. Like the method used to generate a pattern in Co, we first applied a low potential followed by a high voltage (previously the limits of the CV used to pattern Ge by RIPPLE), and then repeated this sequence five times. The EDS map shows that the respective locations of depleted material and oxide rings were inverted from the Co patterns with regard to the low and high potentials (Fig-

ure 3.6b). We then reversed the order of the low potential steps (0.4 V) and the high potential steps (1.1 V) in a second method for pattering Ge (Figure 3.6c,d). The reversed method generated a pattern analogous to the Co pattern, with five discrete oxide bands emanating from a circle that is vacant of material. This result led to the conclusion that the process that etches Ge occurs at the higher potential step, whereas the process that forms Ge oxide occurs at the lower potential step.

We reference the Pourbaix diagram of Ge to examine the behavior of Ge under patterning conditions (Figure 3.12). In comparison with the Co Pourbaix diagram (Figure 2.16), the areas that correspond to corrosion and passivation, which were believed to respectively cause etching and oxide ring for Co, are reversed on the potential axis for the Ge Pourbaix diagram. The predicted behavior of Ge is therefore in agreement with our results above.

We next sought to utilize the control previously exhibited in Figure 3.3 for Co patterns formed by binary potential step patterning. We were able to generate patterns with varying ring spacings and widths depending on the durations of the 1.1 V and 0.4 V steps, respectively. Having isolated the Ge patterning conditions, we confirm a reliable approach to generating rings of Ge oxide in films of Ge using the simple binary-potential step method. We expect that this method can be applied to other materials directly by referencing the material's Pourbaix diagram, without the need for CV as prescribed in RIPPLE. We also confirm that the patterning mechanism is a consequence of a material's redox properties, which is comprehensive across different systems.

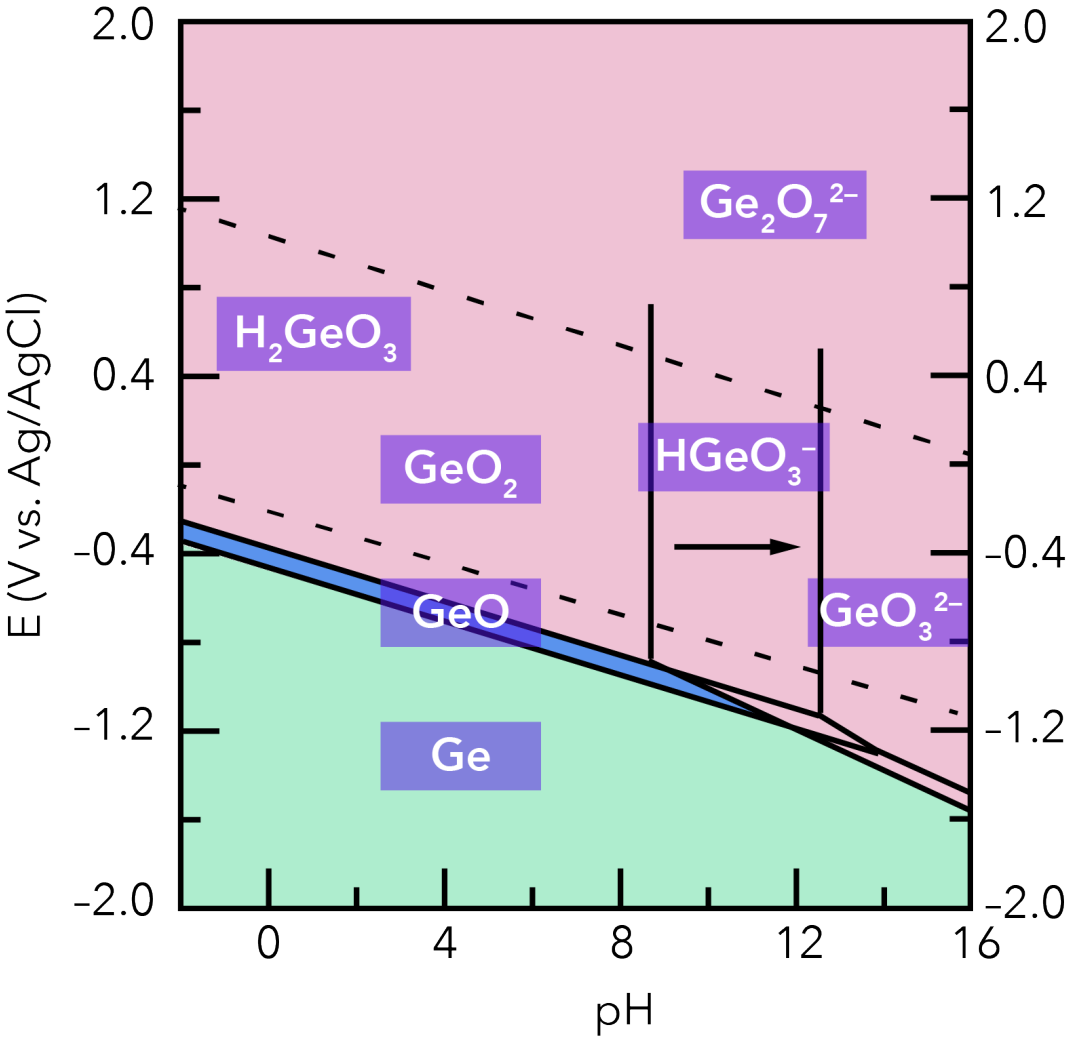


Figure 3.12. Pourbaix diagram for Ge in water, 25 °C. Not all species considered. Colors indicate theoretical conditions for metallic Ge (green), corrosion (red), and passive oxide formation (blue). Arrow represents equilibrium shifting as $[HGeO_3^-]$ increases from 0.1 mM to 1 M. Dashed lines mark H_2/H^+ equilibrium (bottom) and H_2O/O_2 (top). Data from Reference 7.

3.3.4 Dependence of pattern formation on Co^{2+}

We now move from how the redox properties of a material affect patterns to the role of the soluble species formed under patterning conditions. As mentioned above, Co is etched to Co^{2+} upon application of 0.4 V. Here, we resolve the influence of Co^{2+} on the pattern.

Similar diameters of the etch fronts after stepping the potential to 0.2 V, 0.3 V and 0.4 V for 10 s (Figure 3.8) indicate that the etching rate is not limited by the applied voltage. This is compelling evidence that the etch front at 0.4 V is kinetically limited by the diffusion of Co^{2+}, since 0.4 V was the highest potential applied. In contrast, if the etch front was thermodynamically controlled, moving to lower potentials should induce slower etch fronts (smaller diameters). Since the binary potential step method we use for patterning Co films uses a lower potential step of 0.4 V, the etching rate of the patterns must be limited by the diffusion of Co^{2+}.

The role of Co^{2+} in the ring formation was also investigated. After allowing a delay between the formation of the etch front and the application of 1.3 V, an identical oxide ring was formed at the parameter of the etch front. Since 30 min delay was sufficient for the Co^{2+} to diffuse out of the cavity through the opening of the resist, the oxide formation process is independent of diffusion and the concentration of Co^{2+}, suggesting that the primary pathway for oxide formation is the direct conversion of Co metal to Co oxide This is consistent with the observation that the oxide layer extends into the Co^{0} film during application of 1.3 V (Figure 3.5). If Co^{2+} were to deposit as the oxide ring, we would expect the dark oxide ring of Figure 3.5b to form on the inside of the etch front (red circle). Also in support of this finding is the observation of preserved platelets in the RIPPLE pattern generated in electroplated Co (Figure 2.3).

Co is thus etched away at 0.4 V and the metallic front at the boundary of the etching front is converted into the oxide ridge at 1.3 V by the reaction of Co metal with water under this anodic potential. The next ring is then formed upon cobalt etching from the backside of the Co oxide ring. The Co^{2+} ions produced during etching diffuse over the top of rings to the opening in the mask.

3.3.5 Developing and evaluating the Co pattern model

The kinetics process of Co^{2+} diffusion from the etch front is explored with finite element simulations. Defining c as the concentration and J as the flux of Co^{2+}, the conservation of Co^{2+} requires that

$$\frac{\partial c}{\partial t} = -\nabla \cdot \mathbf{J} \quad (1)$$

The simplest case is for **J** to obey Fick's law,

$$\mathbf{J} = -D\,\nabla c \quad (2)$$

Dimensional analysis of eqs 1 and 2 furnishes a relaxation time,

$$t \sim \frac{L^2}{D} \quad (3)$$

where t is the relaxation time, L is the distance from the etching front to the opening, which should be on the order of 10 μm, and D is the diffusivity. Co^{2+} ions are expected to have a diffusion coefficient close to the self-diffusivity of water, on order of 10^{-9} m^2/s.[8,9] Equation 3 furnishes a relaxation time on the order of 0.1 s, which is much shorter than the time scale of operation at 0.4 V (10 s). Consequently, diffusion is taken to be at steady state during etching and the left-hand side of eq 1 is equal to zero. Under these assumptions, the etching rate at any time can be calculated.

At the etch front, we assume the concentration of the Co^{2+} is limited by a saturated value c_{sat}, which gives one boundary condition,

$$c\big|_{\text{front}} = c_{\text{sat}} \quad (4)$$

The concentration of Co^{2+} is assumed to be 0 M at the opening, which gives the other boundary condition,

$$c\big|_{\text{opening}} = 0 \quad (5)$$

Equations 1, 2, 4, and 5, under the steady state assumption, constitute a complete boundary value problem that uniquely determines the concentration distribution once the size of the opening and the position of the etching front are prescribed. The etching front moves as metallic Co is etched. The normal velocity of the etching front is

$$v_n = J\Omega \tag{6}$$

where Ω is the molar volume of the metallic Co and J is the magnitude of the diffusion flux, which is always perpendicular to the etch front due to eq 4. In the axisymmetric case, an analytical solution for eqs 1, 2, 4, and 5 exists,

$$c(r) = c_{sat}\frac{\ln r - \ln r_0}{\ln r_f - \ln r_0} \tag{7}$$

where r_0 and r_f denote the position of the edge of the opening and the etching front. Correspondingly, if we combine eqs 2 and 6 and compute ∇c from eq 7, the velocity of the etch front is

$$v_n = \frac{Dc_{sat}\Omega}{\ln r_f - \ln r_0}\frac{1}{r_f} \tag{8}$$

By definition, $v_n = dr_f/dt$. The time evolution of r_f can be numerically integrated based on eq 8. This allows for calculation of Figure 3.11. The blue rings shown in Figure 3.11 correspond to the position of oxide rings observed in experiments.

In this simulation, we assume that the thickness of the oxide rings is much smaller than the distance between the rings and that the rings do not markedly affect the kinetics of diffusion. With regard to the latter, the diffusion is not significantly affected if the spacing over the top of the ring is more than ~1/10 the height of the film thickness (i.e., the spacing between the Si substrate and the mask overlayer). Figure 3.4 shows that this condition is met. The average ring height is 123 nm vs a film thickness of 173 nm, and thus, the average difference in ring height

from film thickness is 50 nm, or approximately 30% of the film thickness. In addition, the Co oxide ring is porous and fluid may flow through the oxide ring. Hence, the presence of rings does not greatly perturb diffusion for the purposes of this model. In the calculation of Figure 3.11, the opening size is chosen as $r_0 = 1$ μm. The molar volume of metallic Co is $\Omega = 6.6$ mL/mol, and we take $c_{sat} = 1$ M, which is approximately the solubility of saturated $CoSO_4$ solution. The initial condition ($t = 0$) for the calculation is $r_f = r_0 + 0.1$ μm.

Whereas the concentration of Co^{2+} at the opening was set to 0 M in furnishing the results of Figure 3.11, a nonvanishing concentration is required to drive the diffusion from the opening to the bulk electrolyte (Figure 3.10a). The space under the resist is highly confined compared to the space outside the opening, and therefore, we expect a much steeper concentration gradient from the etch front to the opening as compared to from the opening to the bulk electrolyte. Consequently, no matter what the concentration at the opening may be, it will always be small compared to the concentration at the etch front. Thus, setting $c|_{opening} = 0$ M as a boundary condition does not significantly change the diffusion rate. We note that $c|_{front} = 1$ M is much higher than the concentration of the supporting electrolyte, 0.1 M. The complete expression of flux should thus account for the contribution from migration due to this difference in ionic strength,

$$\mathbf{J} = -D\nabla c - \frac{ze}{kT} Dc\nabla\phi \tag{8}$$

where z is the valence of Co^{2+} and φ is the electric potential. The fluxes of the other two ions, SO_4^{2+} and K^+, satisfy similar relations, with their own concentrations and diffusivities. Outside the double layer from the boundary, the solution is electrically neutral. Consequently, the electric potential satisfies the Laplace equation,

$$\nabla^2 \phi = 0 \qquad (9)$$

Figure 3.10b serves to validate the above approximations to yield eqs 5 and 11. In this simulation, which calculates a steady state concentration distribution of Co^{2+}, a geometry like Figure 3.10a is constructed with r_0 = 1 μm, r_f = 10 μm, a metal layer 0.25 μm thick, and a resist 0.4 μm thick. A cylindrical volume of the electrolyte with radius of 20 μm and height of 30 μm is simulated. The concentrations at the top boundary are set to the concentration of the initial electrolyte (that is, 0.1 M K_2SO_4 with no Co^{2+}). The electric potential is set to 0 V at the top boundary. At the etching front, the electric current is set to match the etching rate. The flux of Co^{2+} is specified to a value that makes its concentration at the etching front 1 M.

The proposed model for pattern formation consists of etching metallic Co at low anodic potentials followed by oxidation of the metal to Co oxide when the potential is stepped to a more positive anodic potential. Upon returning the potential, Co oxide formation ceases, and etching begins on the backside of the Co oxide ring, extending away from the center of the ring. This is a departure from our original hypothesis that capillary flow was involved in ring deposition.[5] Our analysis indicates that the etching process is dictated by Co ion diffusion upon etching. The analysis illustrates that as the etch front of metallic Co progresses from the opening, the mass transport of Co^{2+} away from the etch front is deterred because the distance for diffusion into bulk electrolyte increases. Since the concentration at the etching front is limited by the saturated concentration of Co^{2+} and the concentration at the opening is effectively zero, the increase in distance results in a decrease in concentration gradient, which results in a lower diffusion flux. The lower diffusion flux corresponds to slower etching further from the center of the pattern, which accounts for the decreasing ring spacing in the experimental results observed Figure 3.2 It

should also be mentioned that for the simulation of the pattern, we only consider the spacing between the rings. The presence of oxide rings is expected to further narrow the spacing by constricting the diffusion path. However, the geometries of the rings are not critical for observing the trend in the ring spacing. This trend in ring spacing is verified experimentally (Figure 3.2).

Our experimental results supported by analysis show that the mechanism of pattern formation by RIPPLE establishes that the ring position depends on the distance of cobalt ion diffusion into bulk electrolyte, with the kinetics limited by the diffusion of Co^{2+} from the etching front to the opening.

3.4 Conclusion

Radial patterns of Co oxide are formed in 0.1 M K_2SO_4 by first oxidizing Co^0 to Co^{2+} at 0.4 V, which results in etching from the opening in the mask to the inner radius of the first ring. The resulting metal perimeter is then directly oxidized to Co oxide at 1.3 V to form the ring. Ring spacings and widths may be adjusted by modulating the duration of the 0.4 V and 1.3 V potential steps, respectively. By partitioning the patterning process into two discrete potential steps, we achieve improved control of pattern geometry and boundary conditions for the patterning process. With the use of the scaling analysis, a mechanism for producing the observed pattern geometry is correlated to the sequence of electrochemical steps involved in the formation of the submicrometer structures, thus allowing for precise control of the pattern geometry. The ability to pattern large areas of silicon periodically with submicrometer inorganic oxides affords a facile method for electrochemically integrating materials with silicon.

3.5 Experimental Methods

3.5.1 Working electrode fabrication

The working electrode to be patterned was fabricated by etching 4" p-type Si wafers (B-doped, <100>, 1-10 Ω-cm, Nova Electronic Materials) in 7:1 buffered oxide etch (BOE, J.T. Baker) and rinsing with Type I water (EMD Millipore, 18.2 MΩ·cm) 30 s immediately before use. A 300 nm layer of Pt was deposited by electron-beam evaporation onto a p-Si chip to protect the surface from oxidation using an automated instrumented to determine voltage and current parameters for a 2 Å/s deposition rate. Co and Ni thin films (100-500 nm) were grown by loading a recently-etched p-type Si 4" wafer and a crucible of Co metal pellets (⅛" × ⅛" dia., 99.95%, Kurt J. Lesker) into the chamber of a Sharon electron beam vapor deposition system. The chamber was evacuated to 1 μTorr. The crucible was gradually heated over 1 h by slowly increasing the current until it reached 60 mA at 10 kV. A shutter was opened to allow growth of a desired film thickness on the p-Si, while monitoring film growth with a piezoelectric quartz crystal.

Ge films (p-doped) were prepared on Si substrates for the PECVD experiments. The substrates were etched for 10 s in buffered hydrogen fluoride and then inserted into a home-built chemical vapor deposition (CVD) reactor, which was evacuated to a base pressure of 5.4 mTorr. A poly-crystalline p-type Ge film was grown initially at 360 ℃ for 3 min and then at 330 ℃ for another 30 min. The growth pressure was 28 Torr with flow rates of 10, 14 and 100 standard cubic centimeters per minute (sccm) for germane (GeH_4), diborane (B_2H_6, 100 ppm in He) and hydrogen (H_2, Semiconductor Grade), respectively. The film growth rate under these conditions was ~7.5 nm min^{-1} for a total film thickness of ~250 nm.

The electrode surface was masked by spin-coating 950PMMA C4 (MicroChem) resist

over the Co film at 4000 rpm for 45 s and then heating the substrate to 185 °C over 4 min. An electron-beam writer (JEOL-7000) was used to define a square 9 × 9 array of 2 μm × 2 μm square openings in the PMMA. The openings were spaced 80 μm from the nearest neighbor. The PMMA was developed for 45 s in 1:3 MIBK/ IPA developer and soaked in IPA for 45 s. Resist thickness and opening dimensions were confirmed by AFM. The back of the sample (p-Si) and the sample edges were coated with stop-off lacquer (MICCRO Products).

3.5.2 General electrochemical methods

All electrochemical experiments were conducted using a CH Instruments 760D bipotentiostat, a Pt-mesh counter electrode, and a BASi Ag/AgCl reference electrode (stored in saturated KCl), except for in situ microscopy, which utilized either a microreference electrode (none-leak interface, Innovative Instruments) or a BASi Ag/AgCl reference electrode encased in a Luggin capillary tube fabricated by stretching a glass pipet over a flame. All electrochemical experiments were performed with a three-electrode setup within a plastic beaker, except for the in situ recording, where the working electrode was laid horizontal and 0.1 M K_2SO_4 (99.0% min, Alfa Aesar) was dropped onto the surface. A microreference electrode and Pt wire were inserted into the drop, which was contained on the electrode by surface tension. All procedures were performed at ambient temperature (23 ± 1 °C). The microreference electrode contained 3.4 M KCl and was corrected to match the saturated KCl solution using E(Ag/AgCl sat. KCl) = E(Ag/AgCl 3.4 M KCl) + 0.035 V (measured). All potentials mentioned are referenced to Ag/AgCl (saturated KCl).

Consistently wide rings and gaps were generated with the following potential steps in

their respective order: 0.4 V (5 s), 1.3 V (5 s), 0.4 V (7 s), 1.3 V (7 s), 0.4 V (9 s), 1.3 V (9 s), 0.4 V (12 s), 1.3 V (12 s), 0.4 V (15 s), 1.3 V (15 s), 0.4 V (20 s).

3.5.3 Microscopy

Optical microscopy was performed using an Axio Scope.A1 microscope in conjunction with 20× and 50× objectives, a 63× water immersion objective, and an AxioCam ICc 5 (all components Carl Zeiss Microscopy).

Field emission SEM was performed with a Zeiss Supra55VP. The SEM was operated at 3 kV at a working distance of ca. 8 mm with a 30 μm aperture and used the secondary electron (SE2) detector. EDS was performed with an EDAX detector at an electron-beam voltage of 14 kV. The EDS maps were acquired with a dwell time of 200 ms, a resolution of 1024 × 800, and at a working distance of 8.5 mm.

AFM was conducted with AC mode using an MFP-3D system (Asylum Research) with a 300 kHz Al-coated Si AFM tip (Asylum Research) with a scan rate of 0.3 or 0.6 kHz. The AFM maps were masked, flattened, filtered, and line erased for clarity. The "Dull Yellow" color scheme was applied and set to inverted and negative color.

3.6 References

(1) Gileadi, E. *Electrode Kinetics for Chemists, Chemical Engineers, and Materials Scientists;* VCH: New York, 1993.

(2) von Seggern, D. *CRC Standard Curves and Surfaces,* 1993, Boca Raton, FL: CRC Press.

(3) Kempa, T. J.; Bediako, D. K.; Kim, S.-K; Park, H.-G. Nocera, D. G. *PNAS* **2015,** *112,*

5309–5313.

(4) Nagpal, P.; Lindquist, N. C.; Oh, S.-H.; Norris, D. J. *Science,* **2009,** *325,* 594–597.

(5) Kempa, T. J.; Bediako, D. K.; Jones, E. C.; Lieber, C. M.; Nocera, D. G. *J. Am. Chem. Soc.* **2015,** *137,* 3739–3742.

(6) Chen, Y.; Audesirk, H.; Xiang, C.; Lewis, N. S.; *Ener. Env. Sci.* **2015,** *8,* 1736–1747.

(7) Pourbaix, M. *Atlas of Electrochemical Equilibria in Aqueous Solutions,* Pergamon Press: Oxford, 1966; pp 322–329.

(8) Bard, A. J.; Faulkner, L. R. *Electrochemical Methods: Fundamentals and Applications,* 2nd ed; John Wiley and Sons: New York, 2001; Chapter 4.

(9) Ribeiro, A. C. F.; Lobo, V. M. M.; Natividade, J. J. S. *J. Chem. Eng. Data.* **2002,** *47,* 539–541.

Part 4. Studying resist behavior and developing a method for lithography-free electrochemical patterning

Manuscript in preparation.

4.1 Introduction

Lithography is the preferred method for the fabrication of practically all modern miniaturized electronics.[1,2] The conventional photo- and electron-beam lithography techniques that have delivered this revolution in electronic devices remains challenged by scalability, processing time, and most notably, the cost of lithographic writers and the facilities needed to house the instrumentation.[3,4] These challenges have provided an imperative for the development of self-assembly and other benchtop chemical strategies that furnish highly organized architectures while meeting the constraints of simplicity, affordability, and precision.[2,3,5–11]

In Part 3, RIPPLE was modified to use binary potential steps, which allows control of the dimensions of the electrochemically generated pattern.[12] We now examine the role and influence of the resist overlayer on the uniformity of pattern formation. The resist on top of the redox active layer is used to confine etching and oxide pattern formation to a lateral space under the resist, thereby defining a moving boundary for the oxidative process to proceed.[13] This approach allows for precise control of the extent of oxidation and consequently control over the resulting oxide structures. An opening in the resist allows the initial oxidation process to occur; if a hole is produced in the resist, then a ring pattern is generated. As the ring patterns evolve, the resist detaches and lifts away from the underlying metal or semi-metal film.[14] The detachment of the resist appears to be involved in pattern formation, as the resist is directly involved with solution access to the redox-active layer beneath.

The most labor-intensive step of RIPPLE is the lithographic generation of holes in the resist to enable etching to be initiated. In RIPPLE, the ring spacing decreases as the pattern extends further away from the lithographically-defined opening. This tightening of rings is

attributed to an increased concentration of dissolved film material near the edge of where the redox-active film is being etched (the etch front) due to diffusion constraints inherent in the etch front's expansion from the opening.[13] When trying to fabricate large patterns containing many rings from a single opening, this tightening of gaps between rings becomes detrimental to pattern formation (Figure 4.1). The decrease in ring spacing may be remedied by increasing the duration of each successive potential step.[13] However, this strategy adds time to the electrochemical procedure and the ideal durations are empirically difficult to assess. With the goal of simplifying the overall process of patterning in this fashion, we assess the influence of resist properties on pattern formation and the implications of altering the resist. From this information, a lithography-free approach to generating identical patterns is achieved with simple resists such as that furnished from a lacquer-water emulsion, thus greatly simplifying the fabrication of RIPPLE patterns.

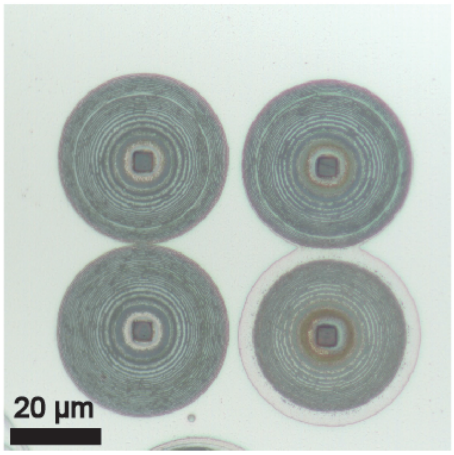


Figure 4.1. Optical micrographs of patterns formed under 950 PMMA C4 spin-coated at 4000 rpm. Patterns were generated by alternating between 0.4 V (10 s steps) and 1.3 V (3 s steps) 25 times in 0.1 M K_2SO_4. Note, rings become less defined and coalesce as the pattern moves further from the opening in the resist.

4.2 Results

4.2.1 AFM analysis of resist

To understand the role of the resist in pattern formation, the properties of the resist were varied. A Co metal film was spin-coated with 950 PMMA C4 e-beam resist (all spin-coating speeds held for 45 s), identical to those previously used in RIPPLE.[12] Holes in the resist are created using photolithography. The resist overlayer was examined by atomic force imaging in solution (liquid AFM) immediately after patterning with the resist still intact (Figure 4.2a). The resist was kept immersed in solution to maintain pressure under the resist and prevent it from collapsing. Using the hole as a reference point, the AFM height map of the resist was compared to the height map of a pattern of the same sample acquired later without solution or resist (Figure 4.2b). The AFM height map indicates that the surface z-height of the resist increases over the patterned area. The height of the resist is highest toward the center of the pattern and gradually declines towards the perimeter of the pattern.

4.2.2 Modulating resist thickness

A S1800 photoresist series was next employed because it offers a wide range of available thicknesses for the same polymer constituent (Table 4.1). Thickness was the first parameter changed because the flexural modulus (i.e., the ability of the resist to lift away from the substrate) is inversely proportional to the thickness of the resist. Figure 1 shows patterns formed under resists of varying thicknesses. Resist thicknesses confirmed by AFM are tabulated as a function of spin

speed in Table 4.1. The resist-coated substrates were suspended in 0.1 M K_2SO_4 and steps of 0.4 V and 1.3 V were each applied ten times in 3 s intervals. For thicker resists, the spacing between rings tightened rapidly, similar to what was observed for 950 PMMA C4 spun at 4000 rpm. In contrast, thinner resists yielded consistent ring spacing up to the perimeter of the pattern (top panel of Figure 4.3).

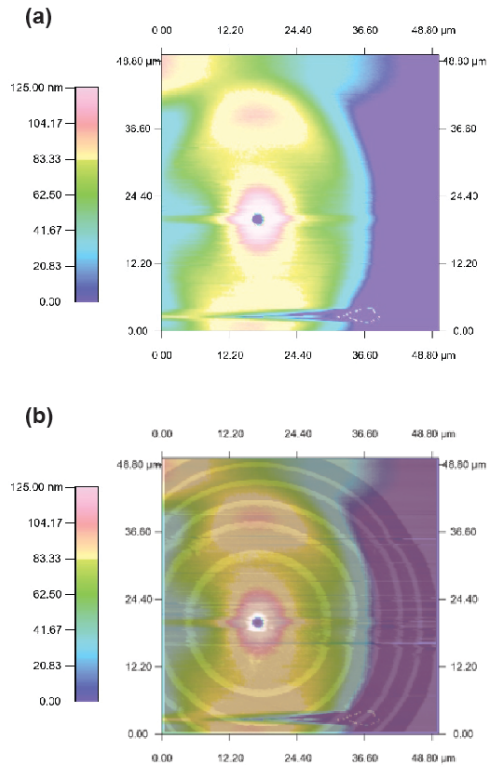


Figure 4.2. (a) AFM height data of 950 PMMA C4 spun at 4000 rpm after cycling between 0.4 V and 1.3 V. Unsymmetrical increase in surface height in respect to the opening in the resist is an artifact caused by scanning parallel to the x-axis. (b) Composite of image in panel (a) overlaid on an AFM height map of a pattern (mapped without solution or resist) generated on the same sample.

The correlation between the resist thickness and its ability to detach and deform away from the metal film was examined. Patterns with ~20 μm diameters were achieved by adjusting the number of 3 s potential steps, so as to normalize the areas patterned under the different resists

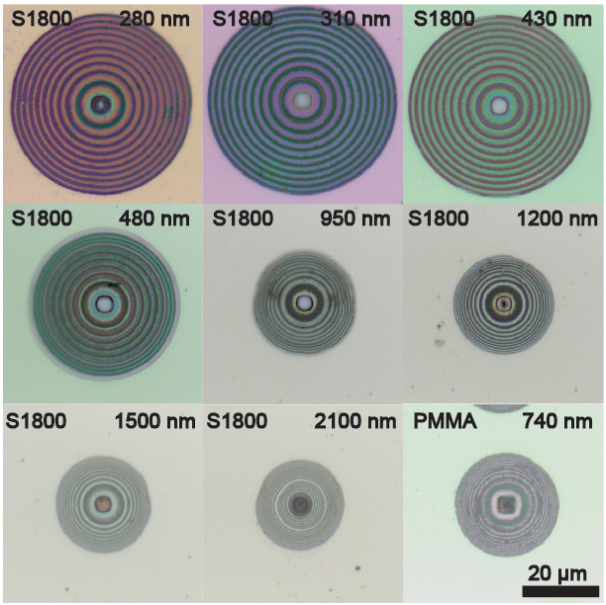


Figure 4.3. Patterns formed by applying 0.4 V (3 s) followed by 1.3 V (3 s) ten times in 0.1 M K_2SO_4. Resist type (S1800 series photoresist or PMMA e-beam resist) denoted at top left. Film thickness at top right. Optical microscope 50× objective.

Table 4.1. Resist thickness values from commercial datasheets and measured values.

Photoresist	Spin speed (rpm)	Datasheet thickness (nm)[a]	Measured value (nm)[b]
PMMA	4000	400	740
S1805	7000	360	280
S1805	4000	460	310
S1805	3000	540	430
S1805	2000	650	480
S1813	7000	1000	950
S1813	4000	1300	1200
S1818	7000	1400	1500
S1818	3000	2200	2100

[a] PMMA thickness data from MicroChem datasheet; S1800 series from Rohm and Hass Electronic Materials datasheet. [b] Measured values from AFM height maps, using the height difference of the bottom of lithographic features from the surface of the resist.

(Figure 4.4). While maintaining the samples in 0.1 M K_2SO_4 solution, the z-heights of the resist over the patterns were mapped by liquid AFM. The results show that for thicker resists of the same material, slight deformation of the resist over the pattern is observed, while thinner resists lift away significantly more from the underlying substrate (Figure 4.5).

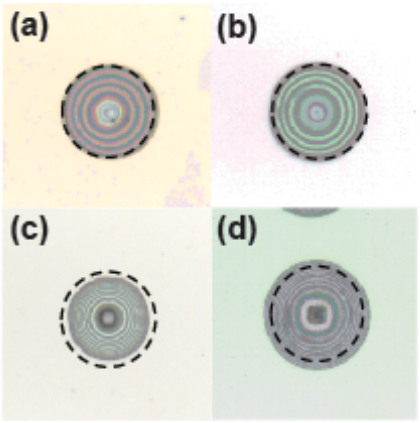


Figure 4.4. Patterns beneath resists examined by solution AFM. (a) S1805 spin-coated at 7000, (b) S1805 spin-coated at 2000 rpm, (c) S1818 spin-coated at 3000 rpm and (d) 950 PMMA C4 spin-coated at 4000 rpm. The electrochemical methods to generate the patterns are as follows: application of 0.4 V (3 s steps) followed by 1.3 V (3 s steps) 4 times for patterns in panels (a) and (b), 10 times for patterns in (c) and (d). Black dashed circles are 20 μm in diameter.

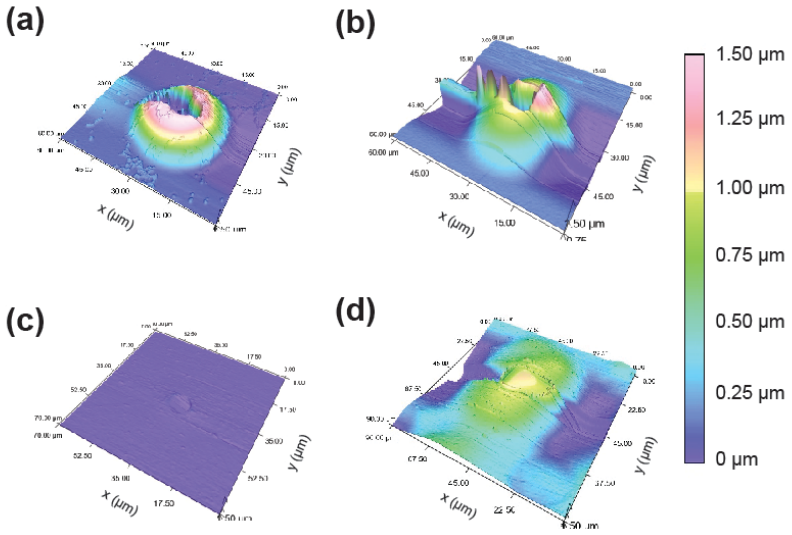


Figure 4.5. AFM height maps of select resist surfaces after patterning. (a) S1805 spin-coated at 7000 (280 nm), (b) S1805 spin-coated at 2000 rpm (480 nm), (c) S1818 spin-coated at 3000 rpm (2100 nm), and (d) 950 PMMA C4 spin-coated at 4000 rpm (740 nm). Unsymmetrical increase in surface height in respect to the opening in the resist is an artifact caused by scanning in the x-direction. (a) and (b) exhibit tears near the opening caused by the AFM tip.

4.2.3 Electrochemical patterning with lacquer beads

A solution of commercial stop-off lacquer and dichloromethane was added to water to yield a two-phase mixture. The mixture was briefly shaken by hand to form an emulsion (Figure 4.6a). The emulsion was drop-cast onto a 250 nm-thick layer of cobalt and allowed to dry, resulting in beads of lacquer ranging from 10 µm to 100 µm in diameter (Figure 4.6b). When this assembly was suspended in 0.1 M K_2SO_4 and 3 s steps of 0.4 V and 1.3 V were applied to the Co metal film 15 times, patterns were observed at the sites of lacquer beads (Figures 4.6c and 4.6d), while the metal between the patterns was removed.

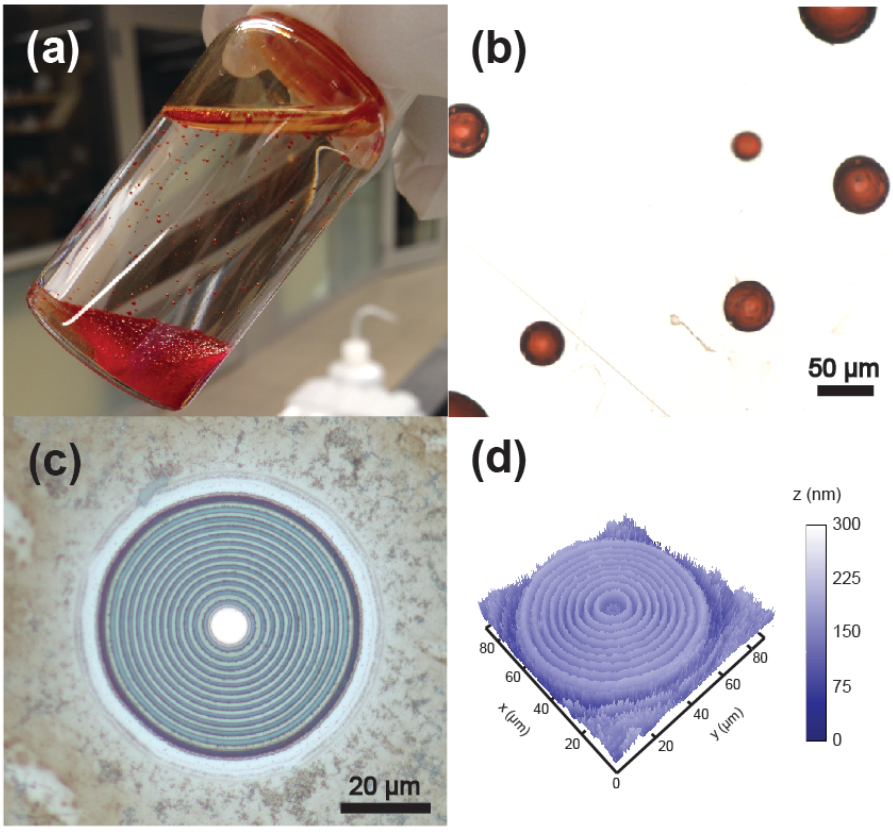


Figure 4.6. Patterning by a lithography-free approach using lacquer beads as a mask. (a) Lacquer-water emulsion. (b) Beads of lacquer drop-casted onto cobalt. (c) Patterns formed under lacquer beads by applying 3 s steps of 0.4 V followed by 1.3 V 15 times in 0.1 M K_2SO_4. (d) AFM height map of a pattern formed by the procedure used in (c).

4.3 Discussion

4.3.1 Resist behavior under patterning conditions

The AFM height map indicates that the surface z-height of the resist increases toward the center of the pattern. This shape of the deformed resist after patterning is consistent with a resist attached only at the perimeter of the pattern, while being allowed to detach and separate

over the patterned area. In other words, the resists is detached completely and allowed to deform away from the substrate, with solution between the substrate and the resist. The bulge forms because the resist is anchored to the edge of the pattern, forming a pocket of electrolyte.

4.3.2 Influence of the resist's properties on underlying pattern geometry

Observing ring spacing as a function of resist thickness establishes that for thin resists, rings toward the outside of a pattern have larger spacing and are well defined as compared to patterns formed under thicker resists. The ability of the resist to deform implies a correlation with the available space for diffusion underneath the resist and thus the ability for Co^{2+} to diffuse away from the etch front and exit through the opening of the resist is enhanced. Since the ability for diffusion of ions away from the etch front is dependent on this volume under the resist, and the velocity of the etch front is an inverse function of local Co^{2+} concentration,[13] it follows that the ability of the resist to deform influences the ring spacing by setting the upper boundary that confines lateral diffusion from the etch front. This contention is consistent with the trend in the degree of ring spacing attenuation observed in Figure 1 and also is in agreement with previously simulated results[13] for an etch front progressing in a narrow space under a rigid resist.

4.3.3 Electrochemical patterning with emulsions as a lithography-free approach

The results from our survey of resist thicknesses imply that a resist should be chosen to allow appropriate diffusion from the etch front in order to obtain uniform patterns. However, the diffusion of ions from the etch front is impeded when etching outward from an opening because of the increasing distance between the etch front and the opening in the resist (to bulk solution), as well as the increasing area of the etch front. This problem is circumvented by

patterning "inward" under a discrete mask. For instance, under a circular mask, the concentration of ions at the etch front will diffuse radially outward, and will not be constricted as the front progresses, resulting in more uniform patterns.

We illustrate this by utilizing the lacquer emulsion above. The patterns contain 13 discrete rings, presumably because the first four steps oxidize the metal around the lacquer bead before a discrete boundary can be formed under the bead. As expected for a configuration with uninhibited outward diffusion of metal ions from the etch front, the ring spacing and widths of the pattern are uniform. Thus, a simple, lithography-free method delivers organized and narrow cobalt oxide structures patterned on silicon.

4.4 Conclusion

The results reported herein show that the nature of the resist has a profound effect on the fidelity of the pattern, especially as the patterned surface area increases. A lithography-free approach to generating patterns may be achieved by replacing a resist overlayer containing lithographically patterned holes with droplets from an emulsion. Patterning under such discrete masks (lithographically patterned polymers versus emulsions) demonstrates the versatility of electrochemical patterning, providing an inexpensive, accessible, and robust technique for patterning surfaces with a well-defined rings of oxide catalysts. In addition, since patterning only requires a consistent moving boundary over the electrode and ample diffusion of metal ion away from the etch front to maintain uniformity, we anticipate the lithographic-free patterning approach to be applicable for a multitude of other systems and especially useful for optimizing integrated Si-catalyst assemblies in integrated PEC architectures[15, 16] for solar energy conversion.

4.5 Experimental Methods

4.5.1 Working electrode fabrication

The working electrode to be patterned was fabricated by loading a recently-etched (buffer oxidizing etching solution, 7:1 buffered oxide etch (BOE, J.T. Baker) and rinsed with water 30 s immediately before use) p-type Si 4″ wafer and a crucible of Co metal pellets into the chamber of a Sharon electron beam vapor deposition system. The chamber was evacuated to 1 μTorr. The crucible was gradually heated over 1 h by slowly increasing the current until it reached 60 mA at 10 kV. A shutter was manually opened to allow the growth of a 250 nm Co film on the p-Si, while monitoring film growth with a piezoelectric quartz crystal.

The electrode surface was masked by spin-coating a positive resist over the Co film. For 950 PMMA C4 e-beam resist, the sample was spun at 500 rpm for 5 s and 4000 rpm for 45 s, followed by baking at 185 °C for 4 min. An electron-beam writer (JOEL-7000) was used to define a square 2 × 2 array of 8 μm × 8 μm square openings in the PMMA. The openings were spaced 72 μm from the nearest neighbor. The PMMA was developed for 45 s in 1:3 MIBK:IPA developer and soaked in IPA for 45 s.

For the S1800 series photoresists, S1805, S1811, S1813, and S1818 were spin-coated over Co films. To control resist thickness, the resists are spin-coated onto samples at 500 rpm for 5 s followed by 2000, 4000, 3000, or 7000 rpm for 45 s (samples are referred to using only the latter spin speed). Samples were baked at 115 °C for 2 min. 5 μm × 5 μm square openings were exposed over the surface with 200 μm spacing between the squares using a Heidelberg μPG501 photowriter. Samples were developed in CD-26 for 3 min and washed thoroughly with

water. Resist thicknesses and opening dimensions were confirmed by AFM. The backs and edges of all samples (p-Si) were then coated with stop-off lacquer.

To prepare films for lithography-free patterning, stop-off lacquer thinned with DCM in a 1:1 ratio. The lacquer solution was then added to water and shaken by hand, which resulted in a stable emulsion. This emulsion was drop-casted onto a 250 nm-thick film of cobalt overlayer on p-Si and allowed to dry.

4.5.2 General electrochemical methods

All electrochemical experiments were conducted using a CH Instruments 760D bipotentiostat, a Pt-mesh counter electrode, and a BASi Ag/AgCl reference electrode (stored in saturated KCl), except for samples prepared for atomic force microscopy (AFM), which utilized a non-leak micro-reference electrode (Innovative Instruments). All electrochemical experiments were performed with a three-electrode setup within a polypropylene beaker, except for samples prepared for AFM, where the working electrode was laid horizontal and 0.1 M K_2SO_4 was dropped onto the surface. A micro-reference electrode and Pt wire were inserted into the drop, which was contained on the electrode by surface tension. All procedures were performed at ambient temperature (23 ± 1 °C). The micro reference electrode contained 3.4 M KCl and was corrected to match the saturated KCl solution. All potentials mentioned are referenced to Ag/AgCl (saturated KCl).

For AFM samples, S1805 spun at 7000 rpm and 2000 rpm was patterned with applications of four 3 s steps 0.4 V and 1.3 V steps to yield a pattern with a diameter of 20 μm. Similarly, for S1818 spun at 3000 rpm and 950 PMMA C4 spun at 4000 rpm, applications of ten 3 s steps 0.4 V and 1.3 V steps to yield a pattern with a diameter of 20 μm.

4.5.3 Microscopy

Optical microscopy was performed using an Axio Scope.A1 microscope in conjunction with 20× and 50× objectives and an AxioCam ICc 5 (all components Carl Zeiss Microscopy). In-solution AFM was conducted with AC mode using an MFP-3D system (Asylum Research) with a 300 kHz Al-coated Si AFM tip (Asylum Research). The AFM maps were plane fit and line erased for clarity. For Figure 2, "Dull Yellow" color scheme was applied and set to inverted and negative color. The color scheme "PastelMaps" was applied to all AFM height maps of resists. For the pattern height map used in Figure S2b, the color scheme "Mocha" was applied for contrast.

4.6 References

(1) Hines, D. R.; Siwak, N. P.; Mosher, L. A.; Ghodssi, R. *MEMS Lithography and Micromachining Techniques.* In *MEMS Materials and Processes;* Ghodssi, R.; Lin, P., Eds.; Springer: New York, NY, 2011; Chapter 9.

(2) Xia, Y.; Whitesides, G. M. *Annu. Rev. Mater. Sci.* **1998,** *28,* 153–184.

(3) Qin, D.; Xia, Y.; Whitesides, G. M. *Nat. Protoc.* **2015,** *5,* 491–502.

(4) Lu, W.; Lieber, C. M. *Nat. Mater.,* **2007,** *6,* 841–850.

(5) Guiton, B. S.; Davies, P. K. *J. J. Am. Chem. Soc.* **2008,** *130,* 17168–17173.

(6) Brinker, C. J.; Lu, Y.; Sellinger, A.; Fan, H. *Adv. Mater.* **1999,** *11,* 579–585.

(7) Lee, W. Ji, R.; Grösele, U.; Nielsch, K. *Nat. Mater.* **2006,** *5,* 741–747.

(8) Fan, H.; Lu, Y.; Stump, A.; Reed, S. T.; Baer, T.; Schunk, R.; Perez-Luna, V.; López, G.

P.; Brinker, C. J. Nature **2000,** *405,* 56–60.

(9) Mukhopadhyay, R.; Al-Hanbali, O.; Pillai, S.; Hemmersam, A. G.; Meyer, R. L.; Hunter, A. C.; Rutt, K. J.; Besenbacher, F.; Moghimi, S. M.; Kingshott, P. *J. Am. Chem. Soc.* **2007,** *129,* 13390–13391.

(10) Cremer, P. S. *J. Am. Chem. Soc.* **2010,** *133,* 167–169.

(11) Kaplan, C. N.; Noorduin, W. L.; Li, L.; Sadza, R.; Folkertsma, L.; Aizenberg, J.; Mahadevan, L. *Science,* **2017,** *355,* 1395–1399.

(12) Kempa, T. J.; Bediako, D. K.; Jones, E. C.; Lieber, C. M.; Nocera, D. G. *J. Am. Chem. Soc.* **2015,** *137,* 3739–3742.

(13) Jones, E. J.; Liu, Q.; Suo, Z.; Nocera, D. G. *ACS Nano* **2016,** *10,* 5321–5325.

(14) Brandes, R. G.; Dudley, R. H. *Solid State Tech.* **1973,** *120,* 140–141.

(15) Nocera, D. G. *Acc. Chem. Res.* **2012,** *45,* 767–776.

(16) Nocera, D. G. *Acc. Chem. Res.* **2017**, *50,* 616–619.

Part 5. Patterning at a triple-phase boundary

5.1 Introduction

Part 3 describes how a moving boundary can be used to engender electrochemical patterning. We then used various materials and geometries in Part 4 to define a moving boundary, which allows us to pattern using a binary potential step method. These experiments demonstrated that discrete islands were better suited for the diffusion requirements of RIPPLE-like patterning. Utilizing a lacquer emulsion afforded a facile electrochemical method for making concentric circles of oxide. Thus, the previous sections have sought to understand the process of RIPPLE, making adjustments along the way to simplify the setup.

The aforementioned studies have been limited to patterning under solid-state masks. A gaseous phase, however, could analogously be used to define a moving boundary needed for patterning. A gaseous phase "mask," such as a gas bubble on an electrode, has the advantage of being generated by gas-evolving electrochemical reactions, thus transforming a thin film of metal into a self-patterning surface. This chapter explores the possibility of exploiting gas bubbles, as well as the triple-phase interface formed by a partially submerged substrate, for generating submicron oxide structures. The parallel, ridge-like oxide structures produced by a dip-coating method described herein are relevant to PEC design and construction and Co nanostructure applications, such as nano-structured battery anodes.[1–4] As an energy-focused group, we take particular interest in the PEC application, where Co-OEC placement or patterning could improve device performance.[5] In addition, flat-laying parallel structures with large aspect ratios have found applications in electronics.[6,7] Furthermore, the scaffolds used in cellular growth guides, especially for neurons, employ surface ridges with approximately the same widths as the oxide ridges generated by the dip-coating method.[8,9]

5.2 Results

5.2.1 Electrochemically-generated air-liquid interfaces

An electrode consisting of a Co metal-coated p-Si substrate was suspended parallel to the top of an electrochemical H-cell, with the Co-side facing downward. The cell was filled with 0.1 M K_2SO_4 electrolyte so that the solution level filled the cell compartment completely, making contact with the Co-side of the electrode. The electrode was poised at –1.4 V, upon which H_2 gas bubble formation was observed. No changes were observed to electrodes held at this potential. The H_2 bubbles were used as a mask for subsequent patterning (Figure 5.1a). A binary potential step procedure was employed, consisting of 1 s steps of 0.4 V and 1.3 V. Rings were observed by optical microscopy (Figure 5.1b and c).

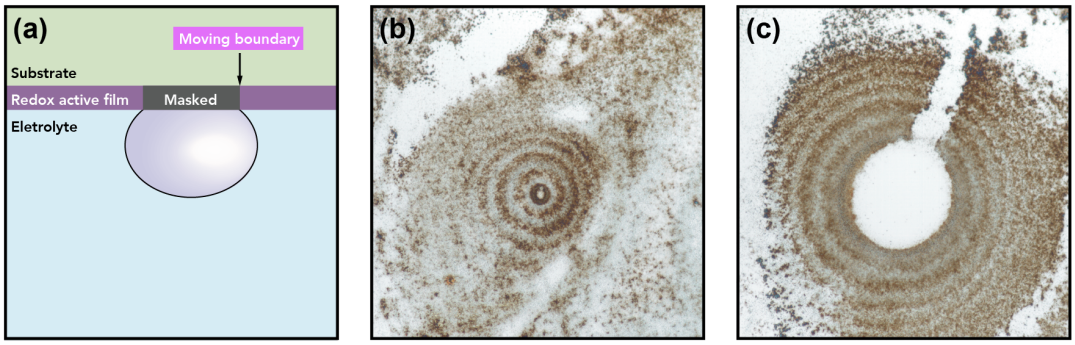


Figure 5.1. (a) Schematic of system used for patterning using an electrochemically generated gas bubbles. A moving boundary is defined as metal is etched from under the bubble. (b) and (c) Optical micrographs of rings made after applying 1-s step potentials of 0.4 V and 1.3 V. 20× magnification.

5.2.2 Patterning in a vertical configuration at a triple phase boundary

Substrates patterned using the emulsion method described in Part 4 are depicted in Figure 5.2 at the contact line of solution. Bands, presumed to be Co oxide, were observed in this region (Figure 5.3a), which become disordered towards the area unexposed by solution (Figure 5.3b). In order to gain more control over the process that formed these surface features, we

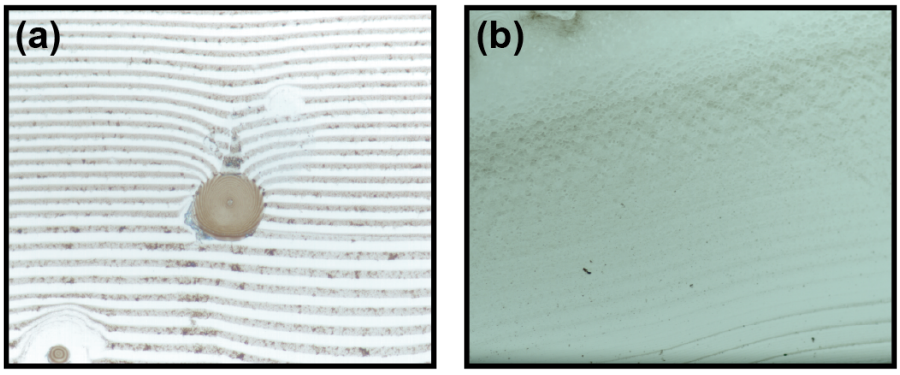


Figure 5.2. Patterning at the solution-air interface. (a) A samples patterned using the lacquer emulsion method in Part 4. Round pattern in center is due to a lacquer bead. (b) Toward the upper limit of patterning in the sample shown in (a). Pattern gradually becomes less defined. 20× magnification.

moved to a configuration where the velocity of the solution contact line could be precisely controlled. Towards these ends, a Co-coated (250 nm) FTO substrate was mounted to the arm of a dip coater, as depicted by the schematic in Figure 5.3. The sample was immersed at various rates, although 6 mm/min (1 μm/s) was found to produce the most well-defined patterns. Potential steps of 0.4 V and 1.3 V were applied as the sample was immersed. The area of the substrate exposed to water became transparent, indicating the oxidation of Co (Figure 5.4b).

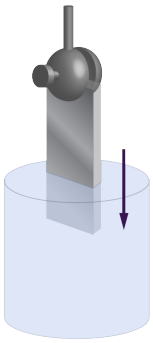


Figure 5.3. Schematic illustrating operation of dip coater as utilized for electrochemically patterning oxide over the surface of a substrate.

Optical microscopy revealed parallel ridges of oxide running orthogonal to the direction of immersion (Figure 5.4c). Figure 5.4c shows that the ridges are grouped in sets, forming bands that are sometimes linked by one to two ridges running diagonally between them. The ridges

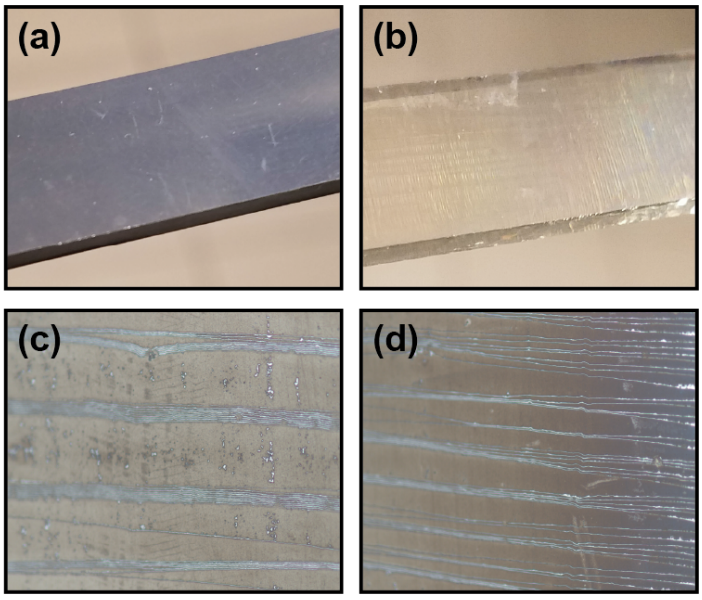


Figure 5.4. Co-coated FTO (a) before and (b) after being electrochemically patterned using immersion to generate a moving boundary. Optical micrographs (20×) of the patterned surface (c) at the center and (d) at the edge of the sample.

become homogeneously spaced towards the edges of the sample (Figure 5.4d). This pattern is consistent across the 4 cm length of the sample. SEM and EDS elemental maps inform that the ridges are on the order of 1 μm-wide and are composed of Co and O (Figure 5.5 and Figure 5.6). Co was removed between the ridges. Figure 5.6 informs that the bands are sets of approximately 10 ridges.

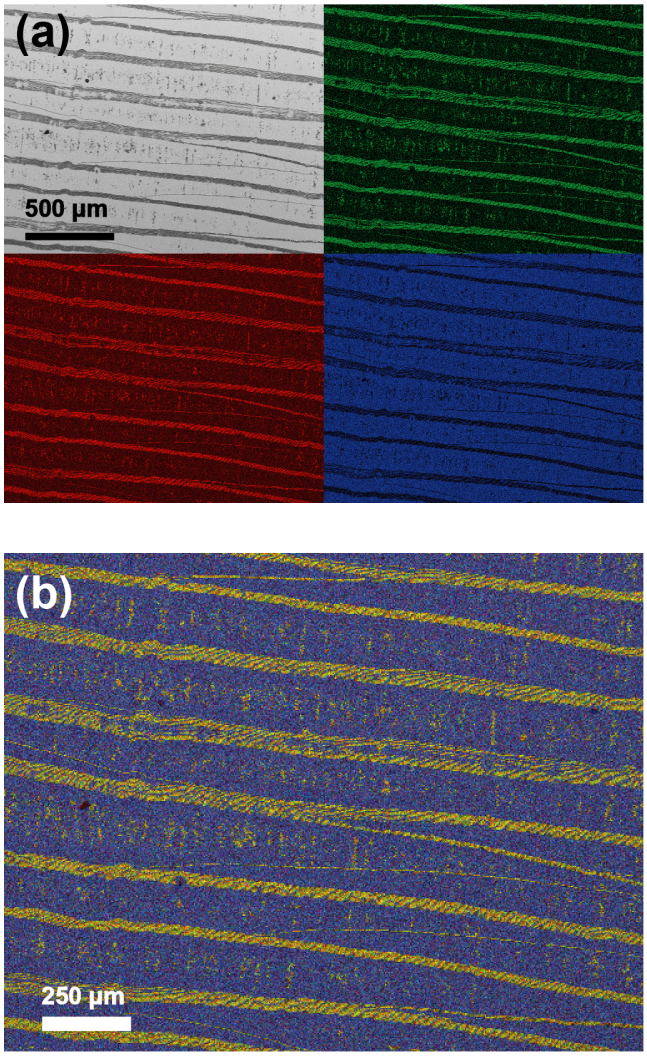


Figure 5.5. Ridges on patterned sample from Figure 5.3. (a) SEM of oxide ridges (grey), with corresponding EDS elemental maps for Co (green), O (red), and Sn (blue). (b) Linear addition of elemental EDS maps shown in (a).

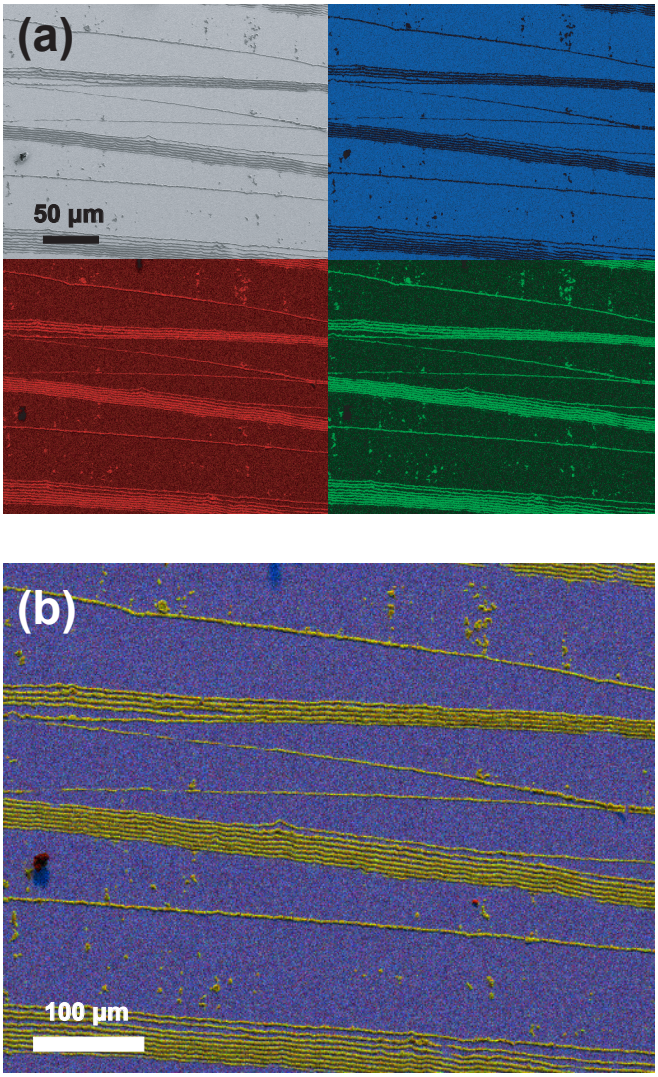


Figure 5.6. SEM micrograph from Figure 5.4 magnified 2.25 to show local ridge distribution. (a) SEM of oxide ridges (grey), with corresponding EDS elemental maps for Co (green), O (red), and Sn (blue). (b) Linear addition of elemental EDS maps shown in (a).

5.2.3 Optical and electrochemical characterization of the patterned samples

The transmittance and reflectance spectra of a sample electrochemically patterned by immersion were measured using an integrating sphere compared to films of Co-OEC (Figure

5.6). The patterned film has a similar transmission profile to that of a Co-OEC film formed by passing 30 mC/cm^2 (Figure 5.7). However, the patterned sample has lower reflectance in the

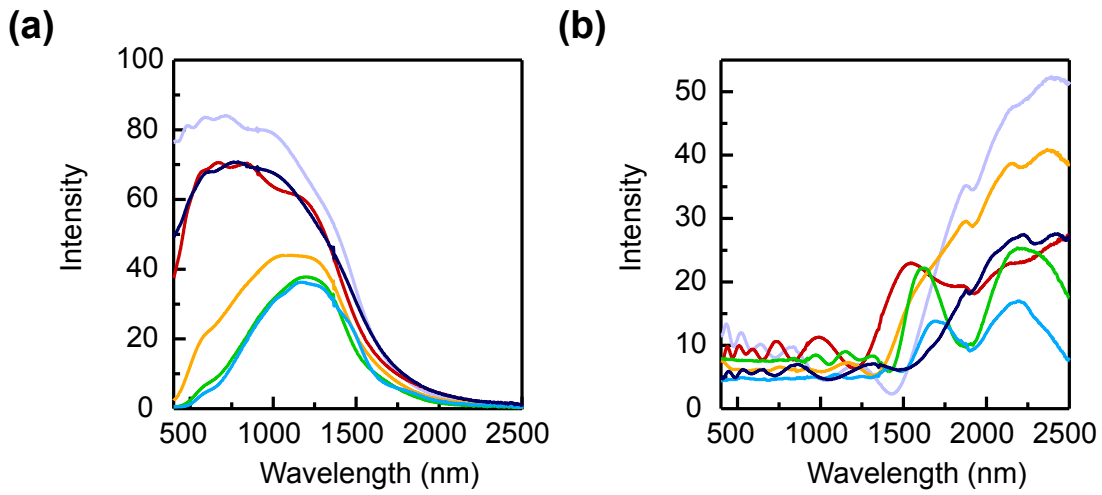


Figure 5.7. Integrating sphere (a) transmittance and (b) reflectance spectra for Co-OEC on FTO and patterned electrochemically Co on FTO. FTO (—), 30 mC/cm^2 CoPi (—), 150 mC/cm^2 CoPi (—), 250 mC/cm^2 CoPi (—), 400 mC/cm^2 CoPi (—), and patterned sample (—) after anodization in KP_i at 1 V (30 min).

visible than the 30 mC/cm^2 Co-OEC film (Figure 5.7a). The reflectance spectra of the films and the patterned sample exhibit oscillations indicative of thin film interference (Figure 5.7b).

The electrochemical behavior of the patterned sample was compared to the 30 mC/cm^2 film of Co-OEC over the same surface area (1 cm^2). The samples were held at 1 V. The 30 mC/cm^2 Co-OEC achieved a current density of 0.10 mA, while the patterned sample reached steady state at 0.05 mA. After 20 hours of electrolysis, the sample was examined by optical microscopy. No change was observed to the oxide ridges.

5.2.4 Determining cell potential

The voltage of the cell during patterning was determined by measuring the open circuit potential between the working electrode (Co-coated FTO) and Pt-mesh counter electrode (Figure 5.9). All cell voltages were generally constant during each 1 s potential step, with deviations on the order of 10 mV. The lower voltage corresponding to the application of 0.4 V vs. Ag/AgCl resulted in a cell voltage of 1.28 V ± 10 mV. This drifted over the application of 200 steps to 1.25 V ± 20 mV. The higher voltage (1.3 V vs. Ag/AgCl) resulted in a cell voltage of 2.21 V ± 9 mV.

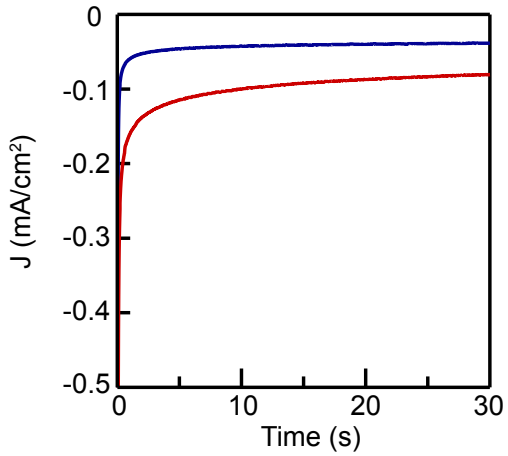


Figure 5.8. Current-time profile for 30 mC/cm^2 Co-OEC (—) and the patterned sample above (—) held at 1.0 V in KP_i, pH 7.

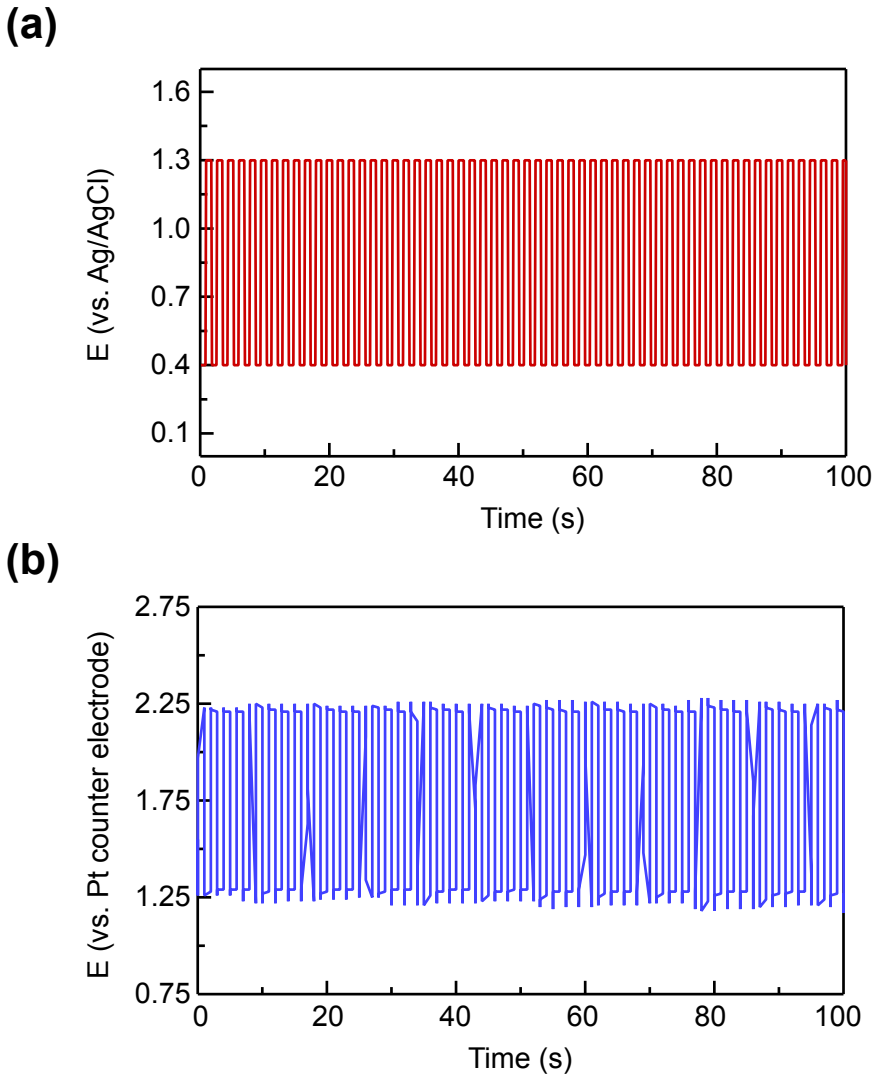


Figure 5.9. Potential-time traces for patterning a Co-coated (100 nm) FTO using a binary-potential step method coupled with immersion (10 μm/s). (a) Applied voltage steps of 0.4 V and 1.3 V vs. Ag/AgCl. (b) OCP-time trace vs. Pt counter electrode resulting from the potential-time trace in (a).

5.3 Discussion

5.3.1 Electrochemically-generated, redox active moving boundaries

The transition from patterning under beads of lacquer to patterning under bubbles was desirable since the patterning process, from metal film deposition to patterning, could be achieved entirely through electrochemical methods. Thus, the fabrication process would be composed of four voltage steps (deposition, gas generation, etching potential, and oxide-forming potential). However, using bubbles as a mask presents multiple complications and resulted in poorly formed patterns.

A bubble of gas on an electrode can define two possible moving boundaries. The first is formed by the oxidation of the metal, as previously observed in the RIPPLE system. Pattern formation is "inward," similar to when patterning under a bead of lacquer, so that a metal's etch front is converging onto a point. The boundary is formed as metal is etched from between the bubble and the substrate. The second moving boundary is the contact line defined by where the gas bubble, electrolyte, and Co metal meet, which may deform as the Co metal is etched, leaving behind a material (Co oxide or p-Si oxide). The new surface is likely to change the adhesion of H_2 to the substrate, and therefore the contact angle of the bubble. Alternatively, solubilized H_2 could be oxidized at the electrode, thereby driving the dissolution of H_2 from the bubble into solution.[10] The latter decreases the volume of the H_2 in the bubble and therefore the footprint of the bubble on the electrode. Ultimately, the velocity of the contact line of the bubble should determine the rate of etching, since metal can be etched in a direction normal to the surface of the substrate once it is exposed to solution. The grainy patterns observed in Figure 5.1 could be a result of the bubble contact line moving faster than the etch front.

5.3.2 Electrochemical patterning using a dip coater method

While patterning substrates using the emulsion method in Part 4, it was observed that at the region of the substrate where etching of metal ceased at approximately the solution-air interface, parallel bands of oxide were formed (Figure 5.2a). These bands were relatively straight and traversed the 1 cm-wide Si chip. We surmise that the bands were formed as solution advanced up the Co-coated Si chip due to capillary action. At the upper limits of the etched area, the bands narrowed, eventually "breaking," resembling breaking waves (Figure 5.2b). At this point, a static capillary surface is formed, where the stress tensor for Newtonian flow is the hydrostatic pressure of the solution at the interface and is equal to the product of gravity and density of the electrolyte plus an integration constant, as described by the Young-Laplace equation. Since the velocity of the contact line is predicted to slow as the static surface forms, the bands of oxide becomes accordingly thinner. In addition, the contact angle of the solution decreases, limiting diffusion of Co from the etch front, resulting in the less-resolved bands in Figure 5.3b as predicted by the diffusion model presented in Part 3.

While the emulsion patterning method is simple, using round particulates, such as droplets of lacquer, to mask the substrate is not ideal for patterning large areas uniformly, as the particles are limited by packing. In addition, discrete masks must either be distributed randomly, self-assembled, or manually manipulated. The contact line of the triple-phase interface formed when a substrate is submerged in a solution is an alternative moving boundary that could be utilized to pattern substrates electrochemically. Toward these ends, we employed a dip coater to better control the velocity of the triple-phase interface to improve patterning.

The dip coating system illustrated in Figure 5.3 presents a multitude of parameters, including immersion speed, electrolyte composition (including the addition of surfactants), elec-

trochemical step durations and potentials, and film thickness. This study only examines the speed of immersion and the electrochemical step durations. While the static capillary surface has been well described,[11] the dynamic capillary surface (moving contact line) is poorly understood. If the contact line velocity is low, however, the boundary conditions of the static surface are preserved. Here, we found an immersion rate of 0.6 mm/min (100 um/s) to produce best results for patterning in terms of oxide ridge aspect ratio, with electrochemical step durations of 1 s. The grouping of ridges observed in Figure 5.6 is speculated to be a result of surface tension. At the peripheral of the substrate, the ridges become evenly spaced (Figure 5.4d). This may be explained by the different wettability of the FTO (Sn oxide) coating and the native Si oxide edges of the substrate, which could cause an arching of the contact line. An arching of the contact line is also predicted near the edges of a vertically oriented cuboid due to surface forces.[12] While the center of the contact line is extended forward, attracted to the high polarity of SnO_2 bonds, the ends of the contact line are pulled forward. The center of the contact line is pinned to the surface due to the adhesion of solution to FTO, and then springs upward against the direction of immersion due to surface tension of the surrounding solution. The discrete motion and arching of the contact line was observed during the experiment, and the upward-arching of oxide ridges is also evident in the ridge shapes of Figure 5.4d.

The solution interface provides an ideal boundary for defining parallel lines. This approach affords a route for patterning large-scale areas with parallel, 1-D features of oxide. Future research could examine how surfactants might improve the diffusion of Co from the substrate by modifying the contact angle of the capillary surface. In addition, it may be of interest to control the velocity of the contact line by controlling the volume of electrolyte using a mechanical syringe driver.

5.3.3 Electrochemical and optical properties of patterned Co

Since the context of this study is improving an integrated PEC device by distributing OER catalyst, it is important to measure the electrochemical and optical properties of the patterned substrate. The results in this section are limited to preliminary measurements and do not represent the full potential of this patterning technique for the purposes of catalyst distribution. Rather, this section serves to outline the key measurements for a more rigorous study with the end purpose of optimizing a strategy of patterning PEC surfaces for enhanced electrochemical and optical properties.

The transmittance spectrum suggests that the patterned sample from 5.2.2 is comparable to 30 mC/cm^2 Co-OEC (Figure 5.7a). However, the activity is only 50% that of the Co-OEC (Figure 5.8). There are multiple possible explanations for this result. The electrochromic effect of Co oxide has been well established,[13–15] and it has been observed that Co oxide slowly bleaches over time. It is possible this is due to water vapor binding to the surface of Co-OEC and inducing a redox reaction in the film. In the integrating sphere study, the patterned sample was anodized within hours of the spectroscopy measurements, while the Co-OEC has been deposited in advance by days. Another possibility is that the Co-OEC generated during the patterning process in 0.1 M K_2SO_4 is distinguishable from the films deposited in 0.1 M KP_i buffer, in either or both its optical properties or its electrochemical properties.

In addition, the initial film was only 250 nm thick. It's unlikely we would see an optical improvement due to the "stacking" of Co at specific regions, namely the oxide ridges. Therefore, this area of research is open to optimizing the dip coating method for patterning thicker films, particularly electrodeposited films of metal. Furthermore, the identity of Co-OEC formed in the presence of sulfate is an interesting question yet to be explored.

5.3.4 Converting from a three-electrode configuration to a two-electrode configuration

Since a reference electrode has been used in the previous work, a three-electrode configuration is necessary in order to repeat any of the procedures mentioned. This limitation precludes simple two-electrode configurations suitable for affordable device manufacture. While laboratory potentiostats are relatively inexpensive in terms of the benchtop setting, it is inefficient to use them where simpler electronics suffice.

In order to convert the three-electrode configuration to a two-electrode configuration, the voltage between the working electrode and the counter electrode can be measured using an open circuit potential-time technique. The resulting OCP-t plot is shown in Figure 5.9. The square wave function is mostly maintained, meaning that a device that generates a square wave function should be capable of patterning using the dip-coating technique.

To signify the affordability of our patterning method, a simple device for such that purpose was designed using virtual circuit elements. The design is based on an inexpensive 555 Timer IC, the most popular integrated circuit in manufacture today. The device was constructed on a breadboard and then constructed into a smaller device. Since the wave height, pulse width, and amplitude can be modulated, this single device could be used to pattern an array of materials, including Co and Ge, although trials have yet to be conducted. Regardless, the inexpensive method for mask-less electrochemical patterning represents a significant advancement from expensive lithographic methods.

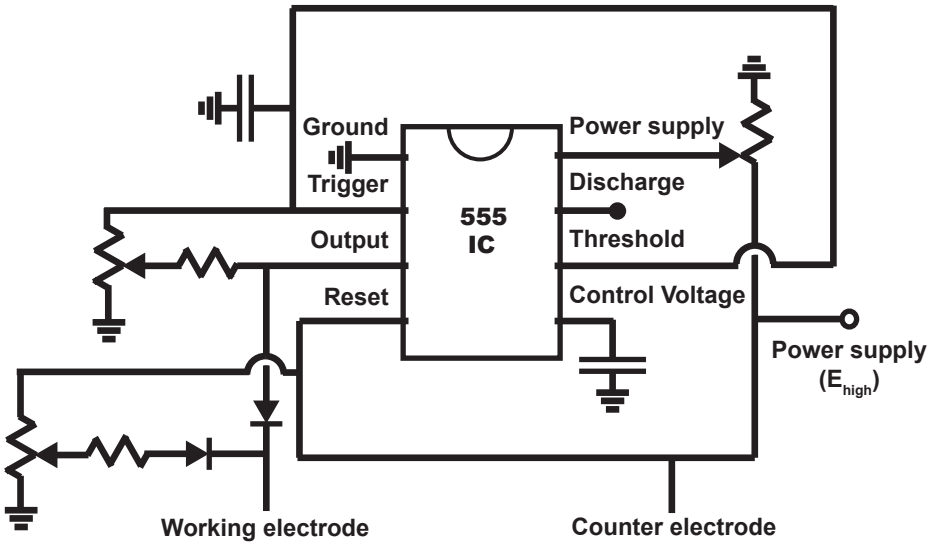


Figure 5.10. Circuit diagram for a device for patterning using the triple-phase interface method. Potentiometers govern wave height (right), pulse width (top left), and amplitude (bottom left). Square wave circuit design elements adapted from Reference 16. Electrical output tested in circuit simulator.[17]

5.4 Conclusion

Removing the resist requirement from the electrochemical patterning methods described in this thesis is a rational strategy for reducing the cost and fabrication demands of patterning by these methods. Substituting the mask with a gaseous boundary has been revealed as useful for obviating lithography, although not without its complications. The bubble method is distinct in that all steps, including film formation, can occur electrochemically. However, the bubble patterning method has proven complicated and resulted in poor structures due to an incompatibility of boundary conditions. In contrast, the dip-coating method offers a simple and scalable method for delivering flat-laying oxide ridges. Our understanding of how the three-phase interface operates provides understanding into the formation of patterns generated using

a binary-potential step method. Optimization is still required, especially for thicker films. Applications, including PEC and electronic fabrication, as well as cellular guidance scaffolds, have yet to be demonstrated.

5.5 Experimental Methods

5.5.1 Substrate preparation

Samples prepared on Si substrates were fabricated by etching 4" p-type Si wafers (B-doped, <100>, 1-10 Ω-cm, Nova Electronic Materials) in 7:1 buffered oxide etch (BOE, J.T. Baker) and rinsing with Type I water water 30 s immediately before use. Co thin films (250 and 100 nm) were grown by loading a recently-etched p-type Si 4" wafer and a crucible of Co metal pellets (⅛" × ⅛" dia., 99.95%, Kurt J. Lesker) into the chamber of a Sharon electron beam vapor deposition system. The chamber was evacuated to 1 μTorr. The crucible was gradually heated over 1 h by slowly increasing the current until it reached 60 mA at 10 kV Co. A shutter was opened to allow growth of a desired film thickness on the p-Si, while monitoring film growth with a piezoelectric quartz crystal. Films of Co were also deposited into FTO (TEC) substrates following this method.

5.5.2 General electrochemical methods

All electrochemical experiments were conducted using a CH Instruments 760D potentiostat, a Pt-mesh counter electrode, and a BASi Ag/AgCl reference electrode (stored in saturated KCl). All electrochemical experiments were performed with a three-electrode setup within a glass H-cell, except for samples prepared by dip coating, which used a 500 mL flask. All proce-

dures were performed at ambient temperature (23 ± 1 °C). All potentials mentioned are referenced to Ag/AgCl (saturated KCl). The electrolyte in all experiments was 0.1 M K_2SO_4 (99.0% min, Alfa Aesar) prepared using Type I water (EMD Millipore, 18.2 MΩ-cm). For measuring the OCP-t, a secondary potentiostat was used to reference the working electrode to the Pt counter electrode.

5.5.3 Patterning under H_2 bubbles

A Co-coated (250 nm) Si substrate was placed on top of an H-cell, with the Co-coated surface facing downward into the H-cell. The H-cell was filled with electrolyte until the Co-coated surface was in contact with solution over the entire opening of the H-Cell, except for a small opening at the side where the reference and counter electrode were situated. Care was taken to arrange the setup so that the substrate was leveled and to ensure the counter electro was not located directed below the substrate. A voltage of –1.4 V was then applied to the substrate to induce HER. After 20 s, the electrode was patterned by application of a binary-potential step method composed of 200 steps of 0.4 V (1 s) and 1.3 V (1 s). The substrate was then removed from solution and rinsed with Type 1 water.

5.5.4 Patterning at the solution-air interface

Co-coated (250 nm) 5×1 cm^2 FTO substrate was mounted to the arm of a dip coater (QPI-168, Qualtech Products Industry) so that the 5 cm^2, wrapping Parafilm around the top 1 cm portion of the substrate to insulate the Co from the arm clamp. The substrate was situated over a 500 mL flask filled with 0.1 M K_2SO_4. A reference electrode and Pt mesh counter electrode were placed in the solution, away from the path of the substrate. The working electrode

was then fastened to the Co side through a hole made in the Parafilm. The sample was lowered at various immersion rates until 4 cm had been immersed in solution. Potential steps of 0.4 V and 1.3 V were concurrently applied during the immersion process.

5.5.5 Microscopy

Optical microscopy was performed using an Axio Scope.A1 microscope in conjunction with 20× and 50× objectives and an AxioCam ICc 5 (all components Carl Zeiss Microscopy). SEM micrographs were acquired using the InLens and SE2 detectors on a Zeiss Supra55VP (Carl Zeiss AG) operating at 3 kV. EDS maps were acquired on an SEM operating at 14 kV with 60 μm aperture size and WD = 8.5 mm.

5.5.6 Integrating sphere spectroscopy

Integrating sphere spectrums were collected using a U-4100 spectrophotometer equipped with an integrating sphere. The wavelength scan started at 2500 nm and ended at 400 nm at a scan speed of 300 nm/min and a sampling interval of 1 nm, except for the near IR (850 nm), which was scanned at 750 nm/min.

5.6 References

(1) Ryu, J.; Kim, S.-W.; Kang, K.; Park, C. B. *ACSNano* **2010,** *4,* 159–164.

(2) Yang, J.; Liu, H.; Martens, W. N.; Frost, R. L. *J. Phys. Chem. C* **2010,** *114,* 11–119.

(3) Hekmat, F.; Sohrabi, B.; Rahmanifar, M. S., A. *J. Nanostruct. Chem.* **2014,** *4,* 1–4.

(4) Jung, K.-N.; Hwang, S. M.; Park, M.-S.; Kim, K.J.; Kim, J.-G.; Dou, S. X.; Kim, J. H. Lee,

J.-W. *Sci. Rep.* **2015,** *5,* 1-10.

(5) Chen, Y.; Audesirk, H.; Xiang, C.; Lewis, N. S.; *Ener. Env. Sci.* **2015,** *8,* 1736–1747.

(6) Alameri, D.; Ocola, L. E.; Kuljanshvili, I. *Adv. Mater. Int.* **2017,** *4,* 1–10.

(7) Zhang, M.; Zuo, G.; Zong, Z.; Chen, H.; He, Z.; Yang, C.; Zou, G. *Small* **2006,** *2,* 727–731.

(8) Teixeira, A. I.; Abrams, G. A.; Bertics, P. J.; Murphy, C. J.; Nearley, P. F. *J. Cell Sci.* **2003,** *116,* 1881–1892.

(9) Weigel, S.; Osterwalder, T.; Tobler, U.; Yao, L.; Wiesli, M.; Lehnert, T.; Pandit, A.; Bruinink, A. *PLOS ONE* **2012,** *7,* 1–10.

(10) Chen, Q.; Luo, L.; White, H. S. *Langmuir.* **2005,** *31,* 4573–4581.

(11) Finn, R. *Notices of the AMS* **1999,** *46,* 770–781.

(12) de Wijs, W.-J. A.; Laven, J.; de With, G. *AIChE J.* **2016,** *62,* 4453–4465.

(13) Maruyama, T.; Arai, S. *J. Electrochem. Soc.***1996,** *143,* 1383–1386.

(14) Fonseca, C. N. P.; De Paoli, M.-A.; Gorenstein, A. *Adv. Mater.* **1991,** *3,* 553–555.

(15) Fonseca, C. N. P.; De Paoli, M.-A.; Gorenstein, A. *Sol. Ener. Mat. Sol. Cells* **1994,** *33* 73–81.

(16) How to build an adjustable square wave generator circuit http://learningaboutelectronics.com/Articles/Adjustable-square-wave-generator-circuit-with-a-555-timer.php (accessed May 26, 2017).

(17) Circuit Simulator Aplet. http://www.falstad.com/circuit/ (accessed May 26, 2017).

Part 6. Exploring the dynamics of the pre-catalyst for oxygen evolving catalysts

Manuscripts in preparation.

6.1 Introduction

As discussed in Part 1, there is a prevalent belief that an OER catalyst must possess a triad of properties if it is to be used in a commercially viable energy storage device. Those properties are affordability (scalability), efficiency, and structural stability,[1] with emphasis on structural stability.[2–6] By referring to the "catalyst," the literature is often actually referring to the *precatalyst*. The presumed need for structural stability is translated from a need to access active sites. This is typically achieved by situating a high concentration of precatalyst in close proximity to (directly on) the electrode, thereby effectively decreasing the exchange current density of the system. However, a prolonged steady state current for a given Faradaic process is typically the end objective of in aiming to make a structurally stabile film.

Since thin films of metal oxides can tolerate the conditions of OER in neutral and basic conditions, they are generally asserted as the state-of-the-art technology for OER catalysis. Metal oxides, however, are usually unstable under acidic conditions, particularly while at open circuit. Therefore, when trying to design an acid compatible system, oxide thin films are often precluded by low pH. However, acidic conditions afford several important advantages. Certain PEC and electrolyszer components, including Si photovoltaics and acidic proton exchange membranes, are only stable at low pH.[4,7] In addition, under acidic conditions, precatalysts tend not to form insoluble precipitates. (Conversely, in neutral phosphate buffer, Co-OEC, for example, slowly dissolves while at open circuit and the resulting Co^{2+} precipitates as insoluble $CoPO_4$, which cannot be re-deposited onto the electrode.) Thus, at low pH, even if a precatalyst does diffuse away from the electrode, the catalyst can be retrieved from the precatalyst's stable form without having to further alter the system.

In Part 6, we challenge the notion that a practical precatalyst film must have structural stability that prevents it from dissolving to form a metal aquo or salt complex. We begin by analyzing the dynamics of patterned Co-OEC under catalytic OER conditions. We then induce migration of the precatalyst by operating the catalyst at low-pH regimes, where structural stability of the precatalyst is diminished. Surprisingly, the dissolved precatalysts are still active towards OER. This implies that functional stability is distinct from structural stability, and at low pH, the Co-OEC's functional stability is dependent on geometrical parameters (namely, cell volume and electrode surface area). The observation that a catalyst's ability to perform OER is significantly dependent on the precatalyst's concentration inspires a Fe-based system for high overpotential, high efficiency catalysis. The Fe-system has important characteristics needed to fulfill the role of a competitive energy-capture system. These properties will be discussed below.

The results in Part 6 are of particular importance to this thesis. "Dynamic" catalysts may not be paramount to the field of OER catalysis, which has relied heavily on thin film systems. However, they offer a new view on OER catalysis, which contrasts from the conventional view that high catalytic activity of an oxidized, non-noble metal catalyst is dependent on the stability of a solid film. This is indeed true for systems where the reservoir of the active species is limited in quantity (for instance, because of cost constraints). In OER catalysis, where stable metal oxyhydroxide films have been promoted as competitive catalysts almost exclusively, soluble metal species (the metal's form traditionally associated with catalyst instability and inactivity) have the potential to provide a competitive alternative to thin film OER catalysts, especially under acidic conditions.

6.2 Results

6.2.1 Co-OEC migration

For a Co-OEC deposited in phosphate buffer (CoP_i), we examined dissolution of Co from the electrode to solution over the course of catalysis. CoP_i was deposited on a working electrode (E1). The CoP_i-coated electrode was then held at a potential for 72 hr. Co was extracted from the solution *in situ* using a second working electrode (E2) poised at 0.85 V to ensure formation of Co^{3+} while avoiding labile Co^{2+} species predicted in the CoP_i OER catalytic cycle (Figure 6.1a). After 72 hr, the amount of Co^{3+} was measured using an electrochemical titration method by poising E2 at 1 V (Figure 6.1b). The catalytic current density at 1 V is proportional to the amount of Co on the electrode.

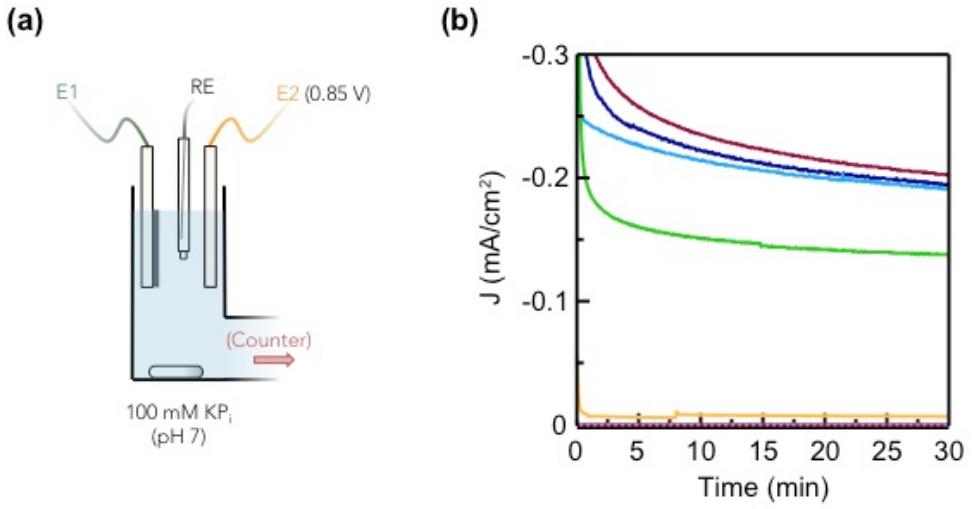


Figure 6.1. (a) Schematic of four-electrode configuration. The first electrode (E1) is 1 cm^2 FTO loaded with 30 mC CoP_i. The second electrode (E2) is 1 cm^2 FTO. E2 is held at 0.85 in both experiments. Electrolysis proceeds for 72 hr. (b) OER currents for E1 and E2. For the experiment where E1 is poised at 1 V: E1 before electrolysis (—), E1 after electrolysis (—), E2 after collection (—). For the experiment where E1 is at open circuit potential: E1 before electrolysis (—), E1 after electrolysis (—), and E2 after collection (—). FTO (dashed —) represents E2 before.

For the control electrode held at 1 V, the steady state current at 1 V after 72 hr electrolysis was 0.1944 mA/cm^2, a slight drop of 4% from the original current of 0.2022 mA/cm^2. The corresponding E2 electrode for this experiment produced a steady state current of 2.112×10^{-8} A/cm^2, only 0.01% of the original current density generated by E1 prior to 72 hr electrolysis. The electrode left at open circuit for 72 hr operated at 0.1376 mA/cm^2, representing a current density loss of 28%.

We next examined local migration across the surface of an electrode. Micro-disks (50 μm dia.) of CoP_i were deposited on masked FTO slides (Figure 6.2). The mask was removed and the electrode was examined before and after 24 hr at 1 V with and without stirring. Samples were then removed, rinsed with Type 1 (18 MΩ) water, and inspected by SEM and EDS (Figure 6.3). No change was observed in disk shape nor was Co detected in the FTO electrode background field. However, in the case of stirring only, a precipitate formed around the perimeter of the circle, which contained a significant amount of P, as evident by EDS. The precipitate did not contain a detectable quantity of Co.

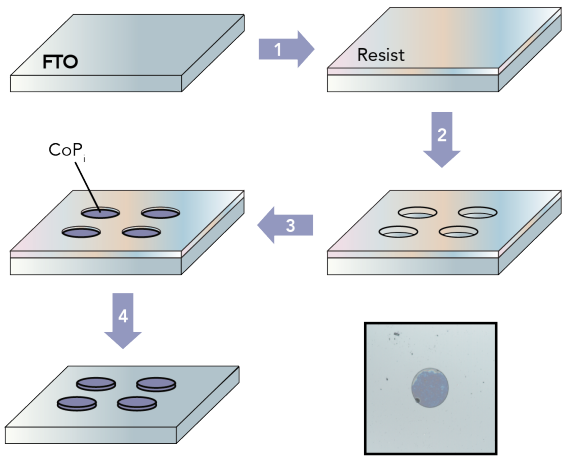


Figure 6.2. Fabrication of CoP_i micro-discs on FTO: 1. Resist is spin-coated over film. 2. Holes (50 μm dia) are made in the resist using lithography. 3. CoP_i is electrochemically deposited into holes in resist. 4. Resist is stripped off. (*bottom left inset*) Optical micrograph of CoP_i micro-disc.

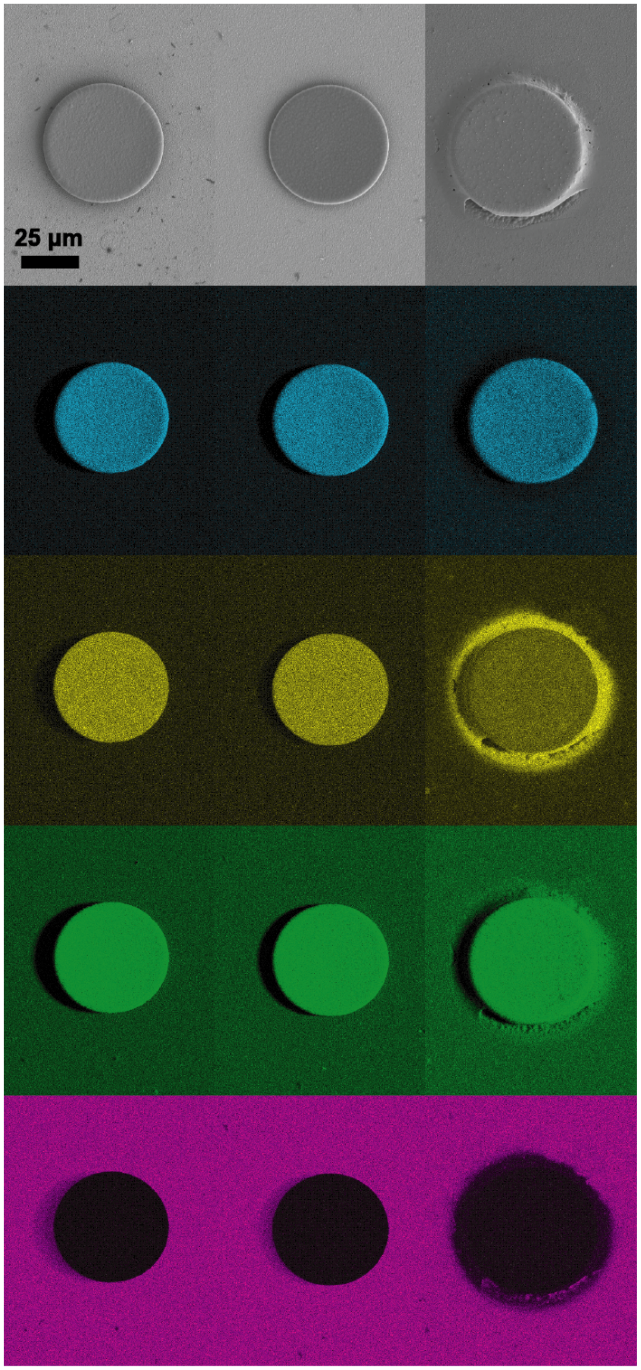


Figure 6.3. Circle of 150 mC/cm^2 CoP_i on 1 cm^2 square section of FTO before (left column) and after, 24 hr electrolysis at 1 V in KP_i buffer (pH 7) without (center column) and with (right column) stirring 24 hr. Rows correspond to SEM (grey), Co (cyan), P (yellow), O (green), and Sn (magenta).

6.2.2 Co-OEC under acidic conditions

Cyclic voltammograms were conducted in various concentrations of Co^{2+} and various pHs using FTO electrodes (Figure 6.4). A catalytic wave is observed at each pH. At higher pH

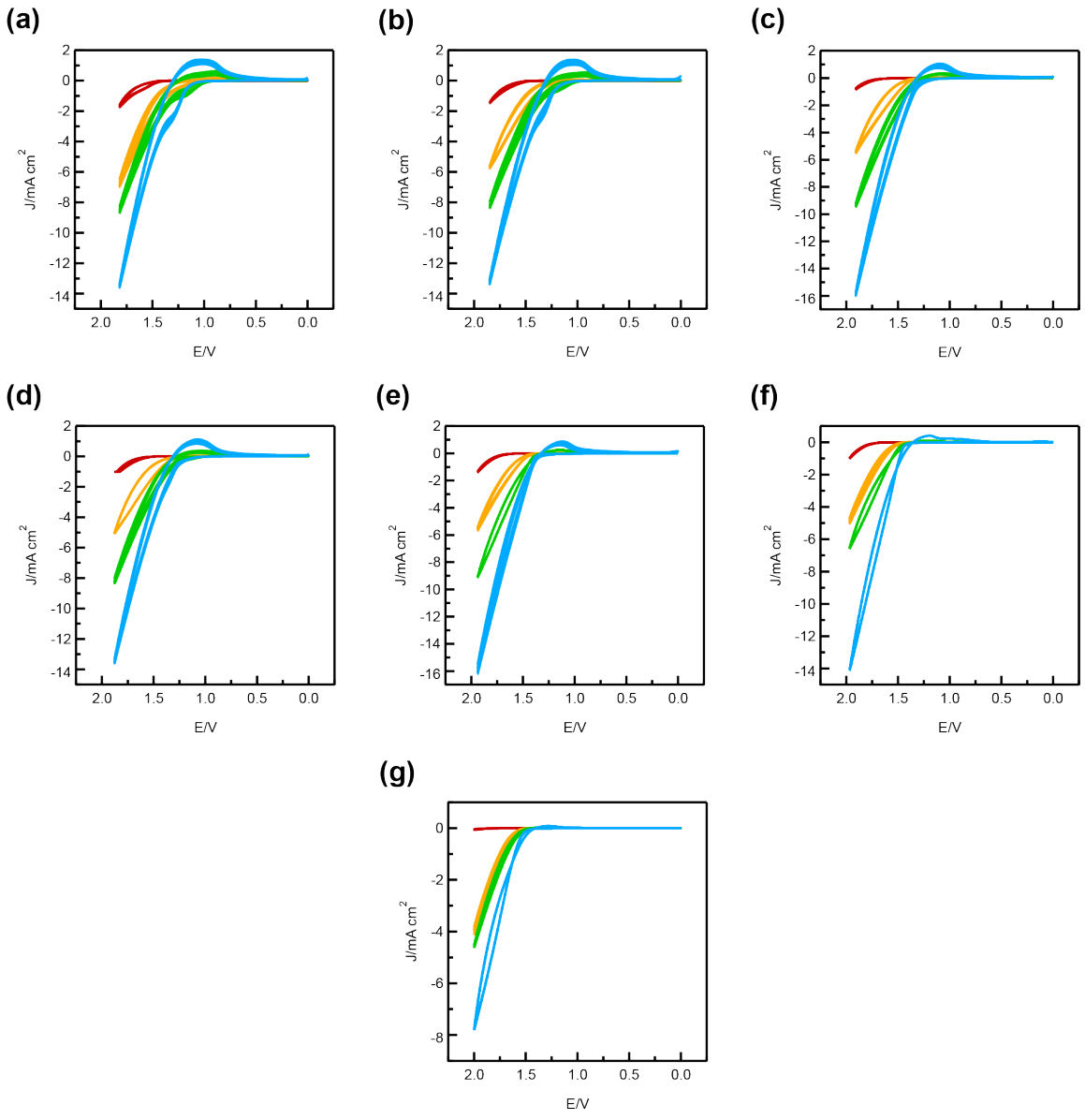


Figure 6.4. CVs at various [Co^{2+}] and pHs using FTO electrodes (1 cm^2). [Co^{2+}]: 0 mM (—), 1 mM (—), 10 mM (—) and 100 mM (—). (a) pH 2.5, (b) pH 3.0, (c) pH 3.5, (d) pH 4.0, (e) pH 4.5, (f) pH 5.0, and (g) pH 5.5.

(5.0-5.5), this wave is preceded by a prewave, which shifts anodically as pH decreases, eventually disappearing below pH 5.0. At each pH, higher concentrations of Co^{2+} correspond with larger currents. The catalytic wave also shifts as pH is decreased. A Pourbaix diagram is plotted for the catalytic wave in Figure 6.5. Two regions are present at pH 2.5–4 and pH 4–5.5 with slopes of 118 mV and 15 mV, respectively.

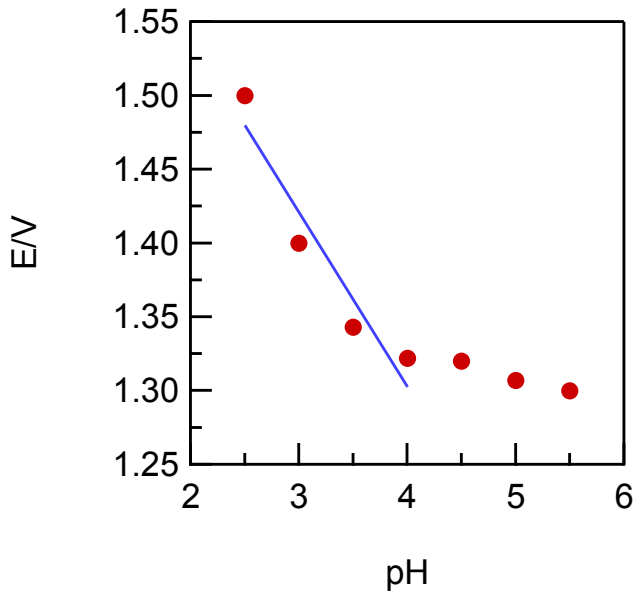


Figure 6.5. Pourbaix diagram for 1 mM Co^{2+}. E corresponds to a current density of 5 mA/cm^2. The blue line is a linear fit for pH 2.5–4 and has a slope of –118 mV/pH.

Upon closer inspection, a "micro-prewave" is observed preceding the catalytic wave and the prewave feature from pH 5.5 (Figure 6.6a). This wave is notably smaller than the typical deposition wave. This wave shifts by ~120 mV/pH (Figure 6.6b). The micro-prewave is dependent on Co^{2+} insomuch as 1 mM is necessary to observe the peak, but beyond 1 mM Co^{2+}, the peak does not shift in potential. The micro-prewave corresponds to a small wave on the FTO background

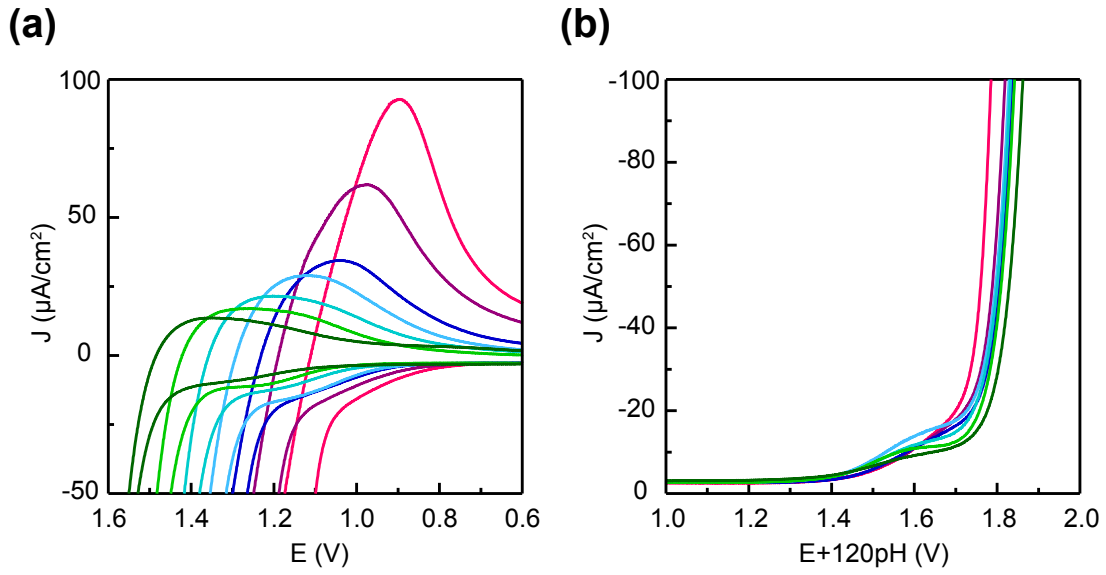


Figure 6.6. Expanded views of micro-prewaves for 1 mM Co^{2+}. pHs: 5.5 (—), 5.0 (—), 10 mM (—) and 100 mM (—).100 mM (—).100 mM (—).100 mM (—). (a) Enlarged current scale of pH composite from Figure 6.4 showing micro-prewave (10 μA/cm²) (b) Forward scans of micro-prewaves shifted by 120pH V to highlight pH dependence. Current and potential scales reversed for clarity of increase. Note prewave (—) rising at left of catalytic waves.

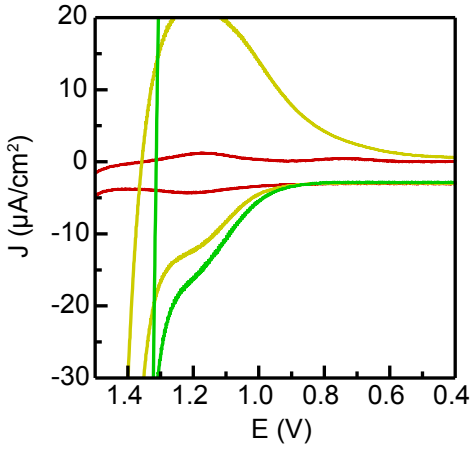


Figure 6.7. Expanded view of Figure 6.3c (pH 3.5) illustrating Co dependence of micro-prewave. [Co^{2+}]: 0 mM (—), 1 mM (—), 10 mM (—).

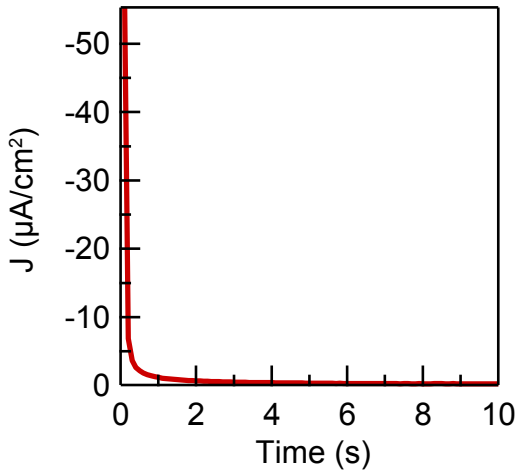


Figure 6.8. Bulk electrolysis with FTO electrode at 1.3 V, KP_i (pH 2.5), 1 mM Co^{2+}.

mM Co^{2+}) trace. Poising the electrode at the micro-prewave (0.78 V – 120 mV × pH) results in a current profile on the order of microamps, immediately following a steep drop that approaches nanoamps within 5 s (Figure 6.7).

6.2.3 Dissolution of CoP_i films in 0.1 M H_3PO_4

Studies were undertaken to explore the relationship between cell geometry and the steady state current of CoP_i under acidic conditions (pH 2.0). Films of 250 mC/cm^2 were set to a potential before being exposed to solution. The working electrodes were then quickly lowered into two solutions with volumes differing by an order of magnitude and allowed to reach steady state (Figure 6.9). The films immediately began to dissolve from the electrodes, as apparent from observation of the FTO. In the current-time trace, three regions of current were observed: i. a sudden decrease in current in the beginning followed by an immediate increase in current with a duration that was inversely proportional to the cell volume, ii. an exponential decrease in

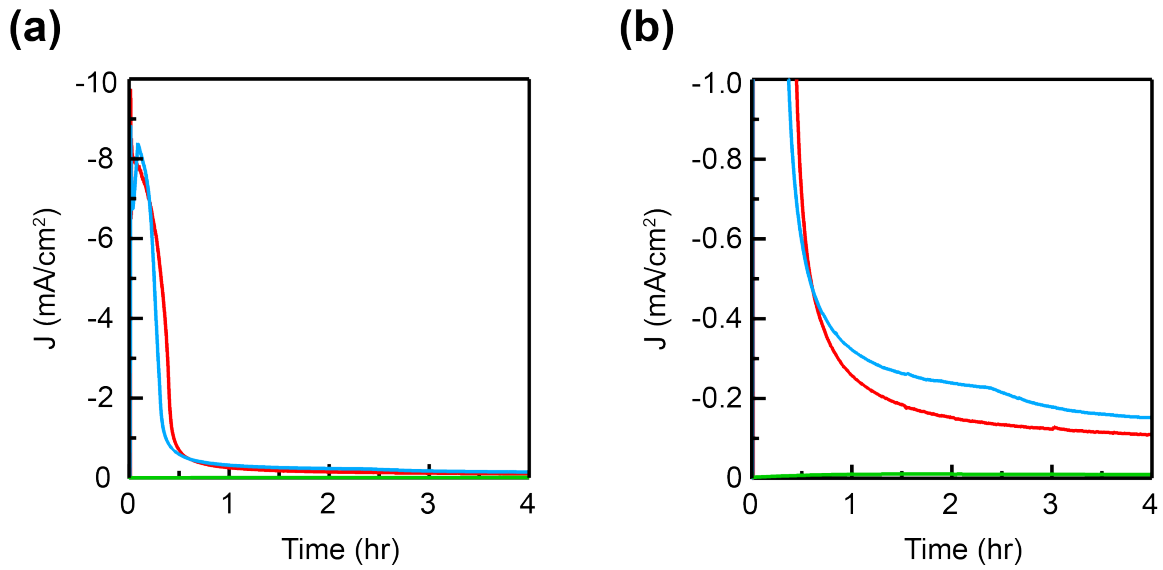


Figure 6.9. (a) Current profile for a 100mC/cm^2 CoP_i film immersed in 0.1 M H_3PO_4 while operating at 1.8 V. Cell volumes compared are 4 mL (—) and 40 mL (—). FTO without CoP_i operating at identical conditions in a 40 mL cell is provided for reference (—). (b) An expanded view of steady state currents observed in (a). No stirring was used. Cells contain two identical compartments separated by a frit.

Table 6.1. Co analysis for CoP_i distribution between the electrode and electrolyte at low pH.

E (V)	pH	Sample description[a]	Amount of Co	Theor. comparison[b]
-	-	Control: 250 mC film	2.59×10^{-6} mol/cm^2	99.9%
1.8	7	Control: 40 mL Wk	2.06×10^{-7} M	
1.8	7	Control: 40 mL Ct	1.12×10^{-7} M	
1.8	2	250 mC film	7.40×10^{-8} mol/cm^2	
1.8	2	40 mL Wk	5.89×10^{-5} M	
1.8	2	40 mL Ct	3.98×10^{-7} M	
1.8	2	Total	2.44×10^{-6} mol	94.3%
1.8	2	250 mC film	6.84×10^{-8} mol/cm^2	
1.8	2	4 mL Wk	5.41×10^{-4} M	
1.8	2	4 mL Ct	4.48×10^{-5} M	
1.8	2	Total	2.41×10^{-6} mol	93.0%
OCP	2	250 mC film	1.81×10^{-7} mol/cm^2	
OCP	2	40 mL Wk	6.67×10^{-5} M	
OCP	2	40 mL Ct	1.46×10^{-6} M	
OCP	2	Total	2.91×10^{-6} mol	111%

[a] Solutions from working and counter compartments denoted by Wk and Ct, respectively. Totals = electrode (film) + Wk + Ct. [b] Theoretical comparison for the control film measurement was calculated from charge passed, C, and the Faraday constant, F, following C/F. Theoretical comparisons of totals are the ratio of summed Co collected to C/F value. A standard deviation of 10.8% was calculated from deviation of the three cell totals.

current as predicted by the Nersnt relationship, and iii. steady state current. The steady state current in the 4 mL cell was larger than the 40 mL cell, although not as large as expected, with the ratio in current density between the 4 mL cell and 40 mL cell being 1.6 at 2 hr and 1.4 at 4 hr.

At the end of the experiments, the electrodes were removed from solution with the potential still being applied. This allowed the electric field to be maintained until the electrode was out of solution, as a measure to maintain the amount of Co on the electrode that was present during electrolysis. The electrode was then washed with concentrated HCl, forming a blue $CoCl_4^{2-}$ species that can be measured accurately by UV-Vis spectrometry.[8] Similarly, solutions from the working compartment and counter compartment were freeze dried and the precipitates were dissolved in concentrated HCl. The results of this experiment are outlined in Table 6.1. Note the standard deviation of 10.8%. Similar to our scaling analysis from Part 4, this analysis does not seek precision results (<10% error), since the cell volume ratios are an order of magnitude different. For quantification at the electrode, the results are more precise since there is less surface area, such as the porous frit in the cell. Ratios of interest for discussion are as follows. First, the electrode from the 40 mL cell, $E_{40\,mL}$, and the electrode from the 4 mL cell, $E_{4\,mL}$, had similar loadings of Co ($E_{4\,mL}/E_{40\,mL}$ = 0.92). Hence, at 1.8 V, the solution of the 40 mL cell ($W_{40\,mL}$) has approximately an order of magnitude lower $[Co^{2+}]$ than the solution of the 4 mL cell ($W_{4\,mL}$). The catalytic current at steady state, however, did not reflect this difference in $[Co^{2+}]$, but were instead comparable. In addition, the electrode held at OCP retained more Co than either of the 1 V electrodes.

The Faradaic efficiency of this experiment was resolved utilizing a fluorescent O_2 probe (Figure 6.10). A trace for evolved O_2 matches the profile of a theoretical amount of O_2 evolved as calculated from charge passed. However, the detection of O_2 is delayed. Furthermore, after

electrolysis was ended at 2.5 hr, there was an immediate increase in O_2. Bubbles were also observed on the electrode, which were detached with stirring. As stirring proceeded, there was a gradual increase in O_2 until reaching a plateau at 6 hr. The O_2 average at the plateau (6-10 hr) implied that OER accounted for the total charge passed (101.0 % ± 4.8 %).

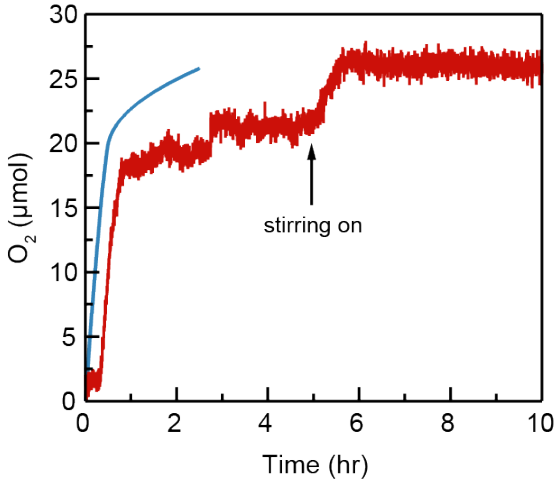


Figure 6.10. O_2 probe data for 250mC/cm^2 CoP_i film immersed in 8 mL 0.1 M H_3PO_4 while operating at 1.8 V. Measured O_2 (—) and theoretical O_2 calculated from charge passed (—).

6.2.4 Exploring Fe acid-stable OER catalysts

6.2.4.1 Iron(III) nitrate

$Fe(NO_3)_3$ was examined as a dynamic OER precatalyst. A solution of was prepared by adding $Fe(NO_3)_3$ to 0.1 M HNO_3. Since the pH scales with concentration of $[Fe^{3+}]$ dissolved (see 6.3.4), $[Fe(NO_3)_3]$ was limited to 0.2 M for pH 3.0. Electrolysis was then performed using an FTO electrode. Tafel analysis revealed three regimes of distinct Tafel behavior (Figure 6.11). At low overpotentials, the Tafel slope is effectively infinite. At 0.6 V, there is a shift to a 56 mV/dec slope, which continues to the third region, where a variable Tafel slope is calculated

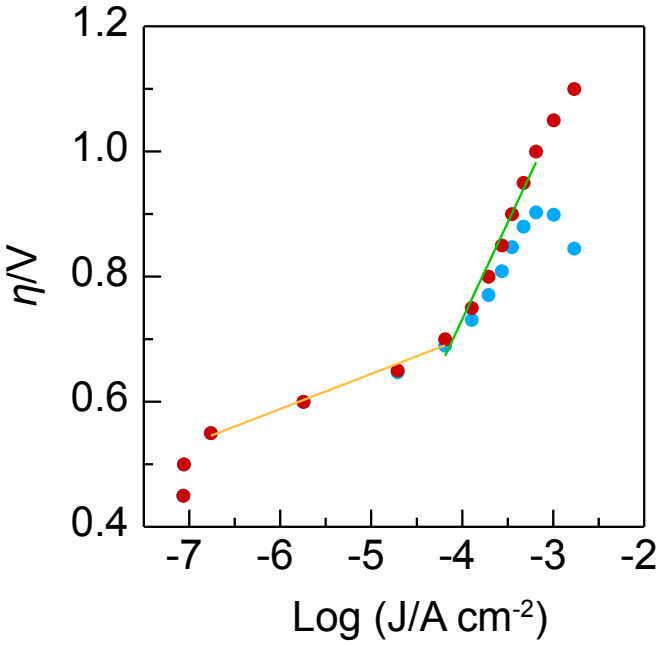


Figure 6.11. Tafel plot for 0.2 M Fe(III)$(NO_3)_3$ (pH 3) with iR subtraction from η (●) and without iR compensation (●). Lines fit to uncompensated data from $10^{-6.8}$–$10^{-4.1}$ A (–) and $10^{-4.1}$–$10^{-3.2}$ A (–) exhibit Tafel slopes of 56 mV/dec and 325 mV/dec. Overpotential scale calculated for OER in pH 3 and referenced to NHE.

depending on the resistance value used for iR compensation. At the limit of the Tafel slope (applied overpotentials >1.1 V), the current drops an order of magnitude (Figure 6.12, not included in Tafel plot). This was accompanied by a pungent odor and an increase in resistance as measured by the potentiostat. Using a multimeter, it was determined that the FTO retained its conductivity (R = ~20 Ω). Likewise, the Pt counter electrode maintained its conductivity. The conductivity across the solution, however, had dropped significantly, as measured across the cell from the working electrode to counter electrode.

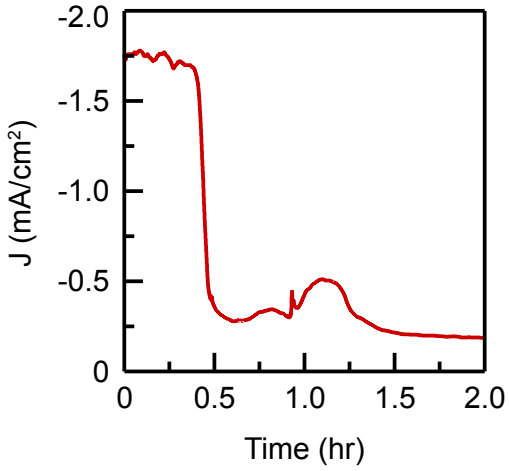


Figure 6.12. Current trace of 0.2 M $Fe(NO_3)_3$ at 2.0 V, corresponding to upper limit of Tafel plot in Figure 6.11.

6.2.4.2 Fe(III) acetate

A solution Fe(III) acetate ($Fe(H_3C_2O_2)_3$) was obtained by saturating 50 mL with 1 g $Fe(H_3C_2O_2)_3$, which produced an opaque, brick-red solution. Filtering the solution through a 0.2 μm filter resulted in a transparent solution that was dark red in color.

$Fe(H_3C_2O_2)_3$, also known as "basic iron," does not decrease the pH significantly when added to water. However, $Fe(H_3C_2O_2)_3$ is limited in solubility to about 0.2 M (as verified by UV-Vis measurements), and therefore, $[Fe^{3+}]$ is not appreciably increased upon saturating the solution with $Fe(H_3C_2O_2)_3$ as compared to the resulting $[Fe^{3+}]$ from $Fe(NO_3)_3$ at pH 3. A Tafel analysis at high overpotentials (>600 mV) was performed (Figure 6.13). During electrolysis, a film was not observed on the FTO electrode, even at potentials exceeding 2 V. The resistance of the FTO was preserved after electrolysis (20 Ω). $Fe(H_3C_2O_2)_3$ displayed a steep (>2.5 V/dec) Tafel slope until the overpotential for OER reached approximately 700 mV. At this point, the

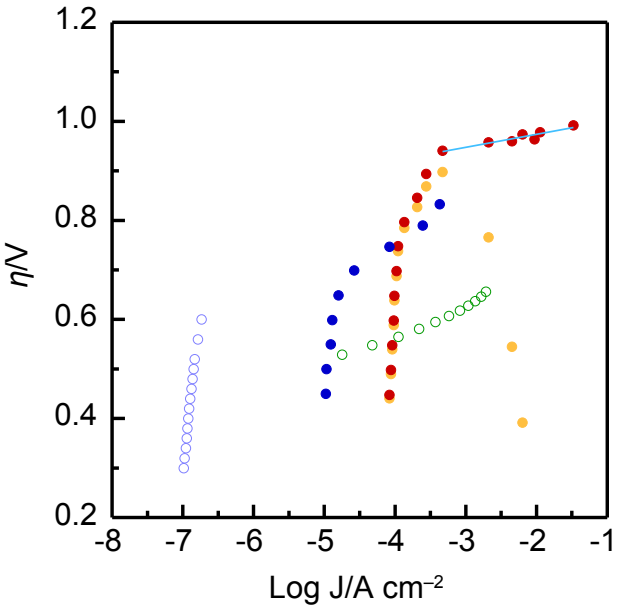


Figure 6.13. Tafel plot for 0.2 M $Fe(H_3C_2O_2)_3$ (pH 3) without stirring and withough iR compensation (●), with stirring and iR compensated for measured resistance ($R_{FTO}+R_{solution}$)(●) and compensated only for FTO (R_{FTO} ~20 Ω) (●). Linear fit for iR uncompensated data from $10^{-3.4}$–$10^{-1.5}$ A (–) exhibits a Tafel slopes of 26 mV/dec. FTO (○) and IrOx (○) data for reference. IrOx data acquired in pH 1 and corrected for pH 3 assuming 60 mV/pH Nerstian shift. Overpotential scale calculated for OER in pH 3 and referenced to NHE. IrOx data from Reference 9.

slope decreased to ~267 mV/dec. At regions beyond 900 mV overpotential, the Tafel slope was highly dependent on the Ohmic drop due to large current density.

Since the Tafel slope is highly dependent on resistance, it was necessary to confirm the measured resistance of the potentiostat. A CV method for achieving resistance was used to verify the instrument's measurement.[10] In this instance, R of the $Fe(H_3C_2O_2)_3$ solution-filled cell was measured as 40.0 Ω. CVs were conducted at a potential range where minimal Faradaic current was observed (Figure 6.14). The compensated resistance, which operates as a positive feedback loop, was gradually increased for consecutive CVs, until the current observed is purely from the double layer capacitance, in which the onset of current sharply increases so that the current profile becomes rectangular. In addition, oscillatory behavior becomes notice as the compensated resistance is increased due to the positive feedback loop of the instrument. Here, this is achieved at 40 Ω. Immediately beyond 40 Ω, the oscillations dramatically increase.

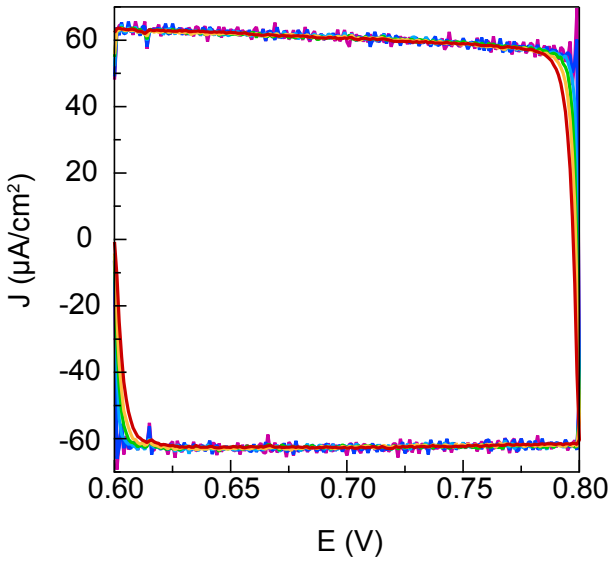


Figure 6.14. CV for 0.2 M $Fe(H_3C_2O_2)_3$ at 10 V/s. iR compensation set to 0 Ω (—), 10 Ω (—), 20 Ω (—), 30 Ω (—), 40 Ω (—), and 41 Ω (—). Note: solution resistance varies with each setup.

The Faradaic efficiency for OER at high overpotentials in $Fe(H_3C_2O_2)_3$ was examined using a fluorescent O_2 probe (Figure 6.15a). The current (~1 mA) was relatively stable over 24 hours, as indicative by the slope of the black line. From the fluorescent probe data, we calculated

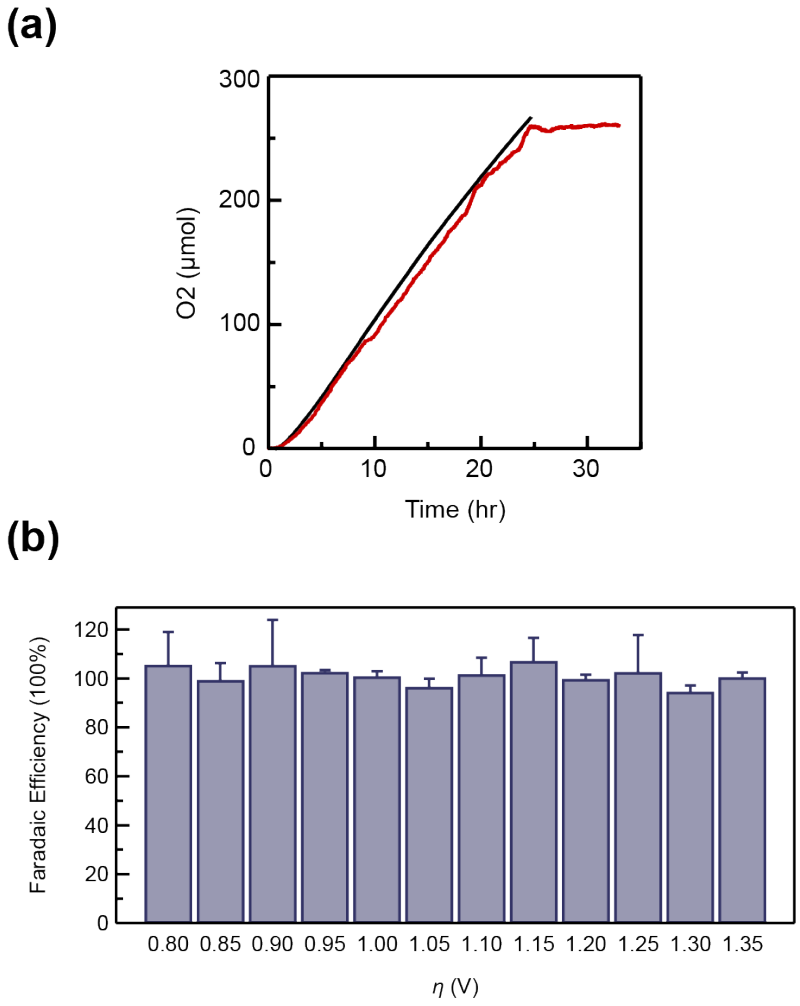


Figure 6.15. OER Faradaic efficiency measurements for $Fe(H_3C_2O_2)_3$ at high current densities. (a) O_2 evolved at 1.75 V as measured by fluorescent probe 1.75 V (—) and O_2 evolved assuming 100% Faradaic efficiency of charge passed (—). (b) Faradaic efficiency measured by gas chromatography.

a yield of 94%. However, measuring O_2 evolution at this current density proved challenging due to a solution shift between compartments caused by a pressure differential across the cell. To remedy the pressure issue, we moved to a previously described gas-flow technique that measures O_2 using gas chromatography (GC).[11] Across the potential range of 0.80–1.35 V, we observed Faradaic efficiencies near unity (Figure 6.15b).

The catalytic species was investigated by using *in situ* UV-Vis spectroscopy (Spec-Echem). The solution was significantly diluted to diminish the $Fe(H_3C_2O_2)_3$ absorbance, which otherwise saturated the spectrometer. In addition, gas evolution caused a shifting of the baseline, but did not appear to cause further distortions. The spectra were corrected by normalizing to a flat region near 700 nm. The electrolysis was performed at 1.8 V over 20 min, with spectra being

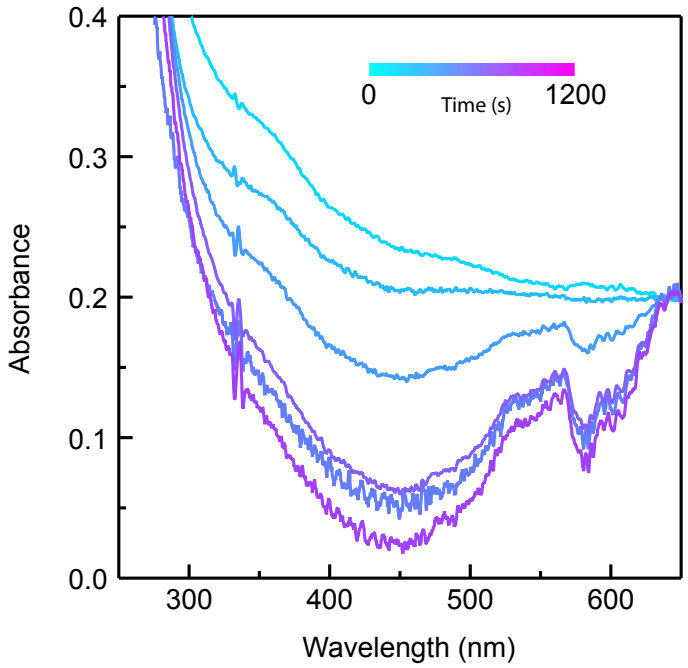


Figure 6.16. *In situ* UV-Vis spectrum for dilute (~0.01 M) $Fe(H_3C_2O_2)_3$ in 0.1 M HNO_3 operating at 1.8 V. Spectra normalized to 700 nm (not shown). Note shoulder at 275–320 nm and feature at 520–560 nm characteristic of FeO_4^{2-}.[12,13]

acquired every 200 s. A general bleaching at 450 nm was observed, while a distinct feature appeared at 520–560 nm. A shoulder also appeared between 275-320 nm.

6.2.4.3 Fe(III) and Fe(II) sulfate

Upon addition of 1 g $Fe_2(SO_4)_3$ to 50 mL 0.1 M H_2SO_4, a milky, pale blue solution was formed, with the majority $Fe_2(SO_4)_3$ remaining undissolved. It was determined that this solution would not be suitable for electrochemistry, since only a small amount of Fe^{3+} was in solution. (As discussed below, an Fe catalyst will only be practical at high concentrations.) An alternative method to generating a soluble $Fe_2(SO_4)_3$ solution was attempted. 1 g of $FeSO_4$ was dissolved in 0.1 M K_2SO_4, which formed a light blue solution. H_2O_2 was then added drop-wise until the solution went from light blue to dark brown, indicative of Fe^{3+}. The $Fe_2(SO_4)_3$ system is under ongoing electrochemical studies.

6.3 Discussion

6.3.1 Evaluating the dynamics of CoP_i under catalytic conditions.

The dynamic motion of Co oxide during electrolysis is pertinent to the preservation of oxide features on the surface of an electrode and is therefore critical to the patterning methods discussed in the foregoing studies. In Part 2, Co patterned by RIPPLE appeared to disperse uniformly across the sample during electrolysis. The sample patterned by the dip coating method in Part 5, however, preserved its features after electrolysis. There remains the question of the degree to which Co-OEC migrates or dissolves during catalysis. In addition, the idea of catalyst movement is also relevant to understanding the stability of a catalyst.[4,14]

As indicated by *in situ* electrochemical titration, CoP_i leaches into solution at detectable levels at neutral pH, but does not dissolve under catalytic conditions (Figure 6.1b). Furthermore, from our micro-disc study, it appears that the CoP_i precatalyst does not migrate across the electrode or distort in shape. Both these results indicate that CoP_i has a static surface during electrolysis, even in the presence of a proximal electric field. Thus, at neutral pH, the CoP_i structure appears to be robust. These deductions imply some interesting ideas that challenge the understanding of self-healing in the field of OER.

In previous studies, Co was believed to constantly dissolve out of the precatalyst film as Co^{2+}, which was assumed to continuously redeposit onto the electrode.[15] This assumption is understandable, given that the proposed mechanism for catalysis invokes a Co^{2+} intermediate, so the catalyst must go through a presumably labile Co^{2+} species with each turnover (Figure 6.17, edge site at top). Consequently, catalytic conditions should accelerate the dissolution of Co^{2+} as compared to open circuit potential, where Co^{2+} leached from a CoP_i film has previously been detected in solution (Figure 6.17 arrow A). However, the likely mechanism for dissolution at open circuit (Co^{3+}-Co^{3+} disproportionation) and the electron transfers that occur as CoP_i cycles through Co^{2+} to the precatalytic Co^{3+} occur at radically different time scales (as evident by the rate of OCP dissolution as compared to the rate/current of catalysis). In addition, multiple protons must be transferred to O atoms surrounding Co to release it from the CoP_i structure, making Co^{2+} dissolution kinetically hindered, except at low pH. These results thus reveal an additional pathway, C, which the precatalyst can take to bypass dissolution. While this distinct option in pathways has previously been recognized and discussed only in a modeling study,[16] it is worth mentioning that the model was originally jointly constructed for the purposes of explain-

ing these results. Hence, the concept of a static CoP_i catalyst is new to the field and a direct result of the efforts of this work.

Though we have gained an understanding through this work regarding the dynamics of CoP_i, the inconsistency still remains regarding the result in Part 2 in which Co oxide formed a homogenous film over the patterned surface under catalytic and neutral (pH 7) conditions (Figure 2.11). We can explain the formation of a homogenous Co oxide film from the dissolution and redeposition of Co from the unpatterened metal, which surrounded the Co RIPPLE patterns. Still, the migration observed here is unexpected, since the dissolution of Co^{2+} for $Co^0 \longrightarrow Co^{2+}$ followed by $Co^{2+} \longrightarrow Co^{3+}$ appears akin to $Co^{4+} \longrightarrow Co^{2+}$ followed by $Co^{2+} \longrightarrow Co^{3+}$. This result may suggest that the key to whether Co^{2+} takes the dissolution path-

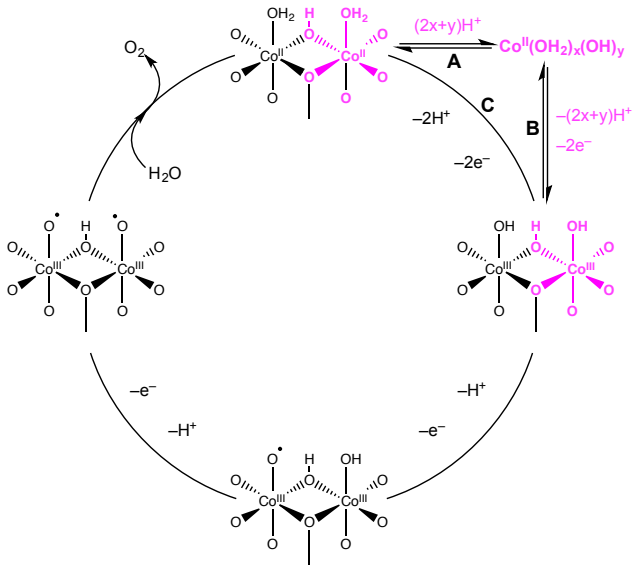


Figure 6.17. Mechanism for CoP_i adapted from Reference 17, with additional pathways A, B, and C.

way or not (A to B vs. C) lies not within the ET rate between Co centers, but rather in the structural environment of Co^{2+}, and in particular, the intricate oxyhydroxide network surrounding each Co^{2+} center in CoP_i. Whereas Co^0 is free to dissolve into solution as a Co^{2+} aquo complex upon oxidation, Co^{2+} in CoP_i is bound to the surface by μ^3–O bonding. The difference in kinetics could be a result in the chemical requirements for hydrolysis of Co^{2+}: for Co^{2+} derived from Co^0, H_2O is readily available to hydrolyze the metal (55 M), whereas for Co^{2+} derived from the oxo-Co^{4+} framework, H^+ concentration is relatively small (10^{-7}). This last detail further challenges established ideas in the field of OER, particularly that self-exchange rates imply that the hole-transfer from Co^{2+} is simply too fast for a Co^{2+} atom to ever leave the surface of an electrode. Since Co^0 is the electrode (extended solid) and the electrode potential determines the driving energy for electron transfer, hole self-exchange for Co^{2+}/Co^0 should occur at the same rate (if not faster, given the lack of reorganizational energy) than Co^{2+}/Co^{3+}.

The static CoP_i mechanism also challenges the idea of self-healing. When the Co-OEC is referred to as "renewing" itself or "a self-healing catalyst," it implies there is an extra repair process, beyond the regeneration cycle that defines all catalysts as *catalytic*, in which the precatalyst is re-deposited onto the electrode. However, from these results, it is apparent that Co-OEC is never separated from the electrode during OER under neutral conditions, nor does it move from its initial point of deposition, even in the presence of a proximal electric field. Hence, the self-healing catalyst does not "continually heal" itself during operation, because there is no need; the film structure remains intact.

6.3.2 Studying CoP_i under dynamic conditions

A truly self-healing catalyst may be achieved during catalysis under acidic conditions. For CoP_i, this process is predicted in part by its Pourbaix diagram (Figure 6.18). The "crossover region," where the deposition potential is predicted to exceed OER, is where the catalyst's

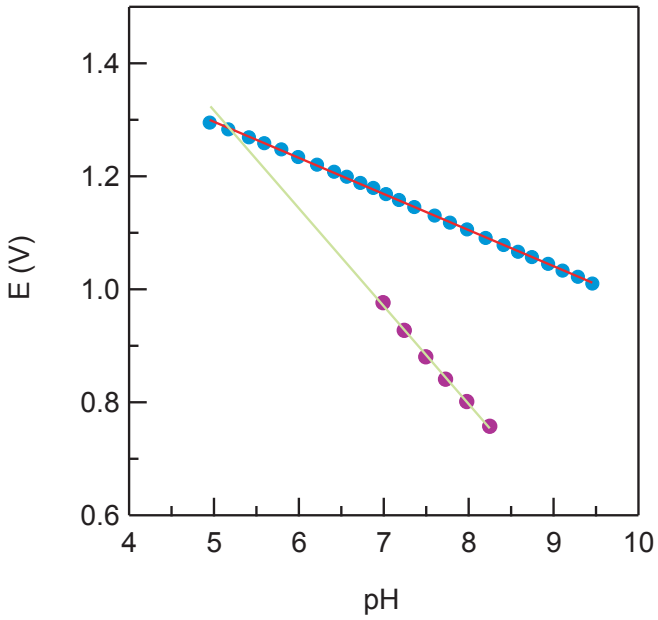


Figure 6.18. Pourbaix diagram for a CoPi film operating at 30 μA, illustrating third and first order proton dependence for deposition (●) and OER (●), respectively. Note the predicted crossover region at pH 5.5, where the red line for OER crosses the green line extrapolated for deposition. Data from References 18 and 22.

environment will have sufficiently more protons available to facilitate Co^{2+} dissolution. Previous studies have explored CoP_i and other OECs in quasi-stable regions of the Pourbaix diagram.[19,20] Stahl *et al.* have investigated this system, finding that Pourbaix behavior governs the stability of catalysis. Here, we present a similar independent study of CoP_i under acidic conditions.

An obvious, but important observation is that OER can indeed be catalyzed by CoP_i even beyond the crossover point (pH 5.5). In fact, the film forms at low pH. This is evident in

work by Stahl *et al.* and in the CVs from Figure 6.4, which show OER being catalyzed by Co-OEC. A common misconception is that OER will proceed before CoP_i deposition can occur, thereby preventing deposition of the precatalyst at low pH. However, the electrokinetic investigation of OER under acidic conditions in the presence of Co^{2+} suggests otherwise; as pH decreases, OER begins to take on the proton dependence of Co–OEC film deposition, implying that the processes now occur concurrently. Thus, the proton dependence of OER is intertwined with that of Co-OEC deposition under acidic conditions. Note that we refer to the catalyst as Co-OEC here and not CoP_i. As the study by Stahl *et al.* points out, the catalyst changes from CoO_2H to CoO_2, which is also predicted by the Pourbaix diagram.[21] The reaction equilibrium for Co^{2+} to CoO_2 involves four protons from two water molecules for every two electrons, resulting in the 118 mV/dec Tafel slope (Figure 6.4). It is unintuitive that as the pH decreases, the Co-OEC structure formed includes fewer protons per CoO_2. The reason is that the Co center takes on a higher oxidation state at the potential necessary to shift the equilibrium away from Co^{2+}.[20] We can anticipate that this catalyst is similar to CoP_i, though, since CoO_2 is analogous to the "unit" of the CoP_i "lattice" (a sheet of cubic edges can be formed with staggered CoO_2 units). As a consequence of the Pourbaix crossover, the dependence of OER on pH is increased by its dependence on film formation, while the dependence of film formation on pH is decreased by changing to a catalyst that is more bonded to the O atoms than Co-OEC at lower potentials. This CoO_2 catalyst can be found across all pHs at higher overpotential, according to the Pourbaix diagram, but its unclear what advantages, if any, a CoO_2 catalyst would have under neutral or basic conditions.

The dependence of Co-OEC activity on $[Co^{2+}]$ at low pH is also predicted by the Pourbaix diagram. This manifests in Figure 6.3 as an increase in current profile with increased $[Co^{2+}]$.

This phenomenon implies two interesting hypotheses. The first is that an active, acid-stable catalyst can be designed by increasing the concentration of the precatalyst. This has been demonstrated by Symes *et al.*[19] and forms the principle basis for the studies discussed in the ensuing sections. The second postulation is the dependence of a catalyst's stability in acid conditions on cell geometry. Thus, an electrochemical cell could be physically engineered to increase the acid stability of a precatalyst film deposited under neutral conditions. The latter is a yet-unexplored concept and is absent from the literature, with the exception of the aforementioned modeling study, which was developed through these investigational efforts.[16]

Towards these ends, we have examined the distributions of Co on electrodes and in solution for CoP_i operated in 0.1 H_3PO_4 (Figure 6.9). As predicted by the CoO_2/Co^{2+} equilibrium, the electrode operated in the smaller 4 mL cell has a higher current density than the equivalent system operated in a 40 mL cell, which demonstrates the notion of engineered stability. Faradaic efficiency measurements indicate that the activity is mostly due to OER (Figure 6.10). However, the current density ratio between the two systems appears to deviate from a first order dependency of Co in solution or on the electrode (Table 6.1). The solution Co concentration in the 4 mL cell, being approximately an order of magnitude greater than in the 40 mL cell, would suggest heterogeneous catalysis. On the other hand, the ratio of measured Co from the electrodes is near unity, which implies that any difference in activity is a result of Co in solution.

In addition, we observed a delay in OER from electrolysis, notably at the onset of hydrodynamic agitation by stirring post-electrolysis. Symes *et al.* has proposed this arises due to O_2 being released by film dissolution and an outgassing process, while the study by Stahl *et al.* in 0.1 M $HClO_4$ suggests the catalytic decomposition of H_2O_2 on Co. A third possibility yet to be explored is the oxidation of water due to Co-OEC dissolution through the disproportionation of

Co^{3+}/Co^{3+}. As Co^{4+} is generated, it can immediately catalyze OER, resulting in Co^{2+} dissolution. In other words, the dissolution of Co^{3+} from the electrode by disproportionation requires an electron source, which is presumably water.

The observation of OER by Co-OEC under acidic conditions also presents the issue of a proton-accepting species. While KP_i does act as buffer at pH 2.2, the proton concentration may be sufficiently large to inhibit proton acceptance from the Co-OEC.[22] An alternative to efficient proton acceptance by KP_i is the Grotthus mechanism, which entails transfer of protons through a hydrogen-bonding network, where the pH is low.[23] The identification of the proton transfer mechanism at low pH, as well as the dependency on Co-OEC on $[Co^{2+}]$ in acid, are potential avenues for future studies.

6.3.3 CoP_i deposition onto an FTO electrode

Our low-pH Co-OEC studies may provide insight into the deposition process of Co-OEC onto an FTO electrode. The detection of a small prewave, referred to in 6.2.2 as the micro-prewave, before the onset of the precatalytic prewave attributed to Co-OEC deposition in pH 5.5, appears to be related to the deposition process of Co onto FTO. Precatalytic features were observed in the work of Stahl *et al.*, though they were excluded as possible surface reactions since they occurred in the presence of Co_3O_4 nanoparticles. While Co_3O_4 particles may serve to catalyze Co-OEC deposition, they may not preclude the deposition of Co uniformly across the electrode at surface sites uncoated by Co_3O_4. Since the micro-prewave exhibits a behavior distinct from Co-to-Co deposition, we desired to further investigate this feature.

The 120 mV shift of the micro-prewave per pH implies a second order dependence on protons, while no shift is observed as $[Co^{2+}]$ increases from 1 mM to 100 mM. However, the

micro-prewave does increases in current as a function of $[Co^{2+}]$ (Figure 6.6), and is not observable in the absence of $[Co^{2+}]$ (Figure 6.8). Therefore, we surmise $[Co^{2+}]$ plays an important ancillary role in the process governing the micro-prewave. The binary dependence on $[Co^{2+}]$, as well as the depletion of a Faradaic process at the micro-prewave's potential (Figure 6.8), leads us to believe the prewave corresponds to a surface deposition process. This is in line with the correlation between the minor feature noticed on FTO in the absence of Co (Figure 6.7), as well as the small current associated with this feature. We propose that the micro-prewave is a surface process with a rate-limited step consisting of the transfer of two protons from hydroxide sites on the FTO's surface. In the presence of Co^{2+}, the hydroxide sites serve as bonding sites to facilitate Co deposition. The second order dependence implies that two surface protons must be removed per Co^{2+}, signifying that Co-OEC has two bonds per Co site to the surface of the electrode. As surface sites are occupied, the wave quickly diminishes. This process thus prepares the electrode surface for the deposition of Co^{2+}, thereby catalyzing and determining the structure of subsequent Co-OEC formation.

6.3.4 Assessing materials as dynamic precatalysts for an acid-stable electrolysis system

This section will elaborate on how we arrive at the Fe precatalysts in Sections 6.2.4–6.2.6. This work, as well as the work of others,[19,20] suggests that stable precatalysts can be formed in acidic conditions under adequate conditions, specifically a sufficient electrode potential and favorable equilibrium. Thus, while decreasing the volume of the cell stabilizes a dynamic catalyst, so does increasing the concentration of the precatalytic species.

As discussed in Part 1, cost is an important factor in realizing a scalable energy storage system. A problem with the increased-concentration strategy is the amount of precatalytic spe-

cies necessary to drive the equilibrium towards the catalytic species. In the case of Co-OEC, for instance, the amount of Co must increase from on the order of 1 μmol used to deposit a film (see Table 6.1) to 1 M (the change in units is because the latter system is volume-dependent). Thus, a simple 100 mL cell increases the demand and cost of Co five orders of magnitude compared to thin films.

While Co is not a rare metal, the cost associated with saturation of electrolyte is prohibitive in the context of scalability. In addition, despite much of this work involving Co, the price of Co has quadrupled in the last two years, purportedly due to the demand in electric car batteries.[24] Demand for such batteries is anticipated to increase with the demand for electric vehicles. Therefore, the only way to achieve a scalable catalyst with this strategy is to select an affordable and abundant metal. Table 6.2 lists metals by prices.

The price chart of commodity metals illustrates that the ideal choice (by almost two orders of magnitude) is Fe. The low price of Fe is at least in part due to its abundance, being the most abundant transition metal in the Earth's crust.[25] There have been several studies on stable Fe thin films catalysts[8,26–29] and Symes *et al.* attempted to make a concentrated Fe OER catalyst, although with no success.[20]

Table 6.2. Commodity base and precious metal prices as of April 2018. Data from Reference 30.

Metal	Cost/kg
Rhodium	$71,959
Gold	$46,890
Iridium	$35,979
Palladium	$33,743
Platinum	$33,018
Ruthenium	$7,584
Silver	$580
Tantalite Ore	$159
Cobalt	$93.74
Ferro Vanadium	$35.20
Ferro Tungsten	$31.40
Molybdenum Oxide	$25.99
Tin	$21.12
Nickel	$13.25
Copper	$6.68
Ferro Titanium	$4.90
Zinc	$3.33
Ferro Chrome	$2.80
Lead	$2.40
Magnesium	$2.25
Manganese	$2.04
Aluminum	$2.01
Iron Ore Pellets	**$0.05**
Iron Ore Fines	**$0.04**

To determine what conditions may promote an Fe OER catalyst, we examine the Pourbaix diagram of Fe (Figure 6.19). For pH 0–4, only Fe^0, Fe^{2+}, and Fe^{3+} are available at moderate potentials. Above ~1.7 V, Fe(VI) is formed as ferrate (FeO_4^{2-}), following Equation 6.1,

$$Fe^{3+}\ 4H_2O \rightarrow [FeO_4]^{2-} + 8H^+ + 3e^-, \qquad \text{(Eq 6.1)}$$

which follows the Nernstian relationship,

$$E^0 = 1.700\ \text{V} - 158\text{mV}\ \text{pH}\log\frac{[FeO_4]^{2-}}{Fe^{3+}}. \qquad \text{(Eq 6.2)}$$

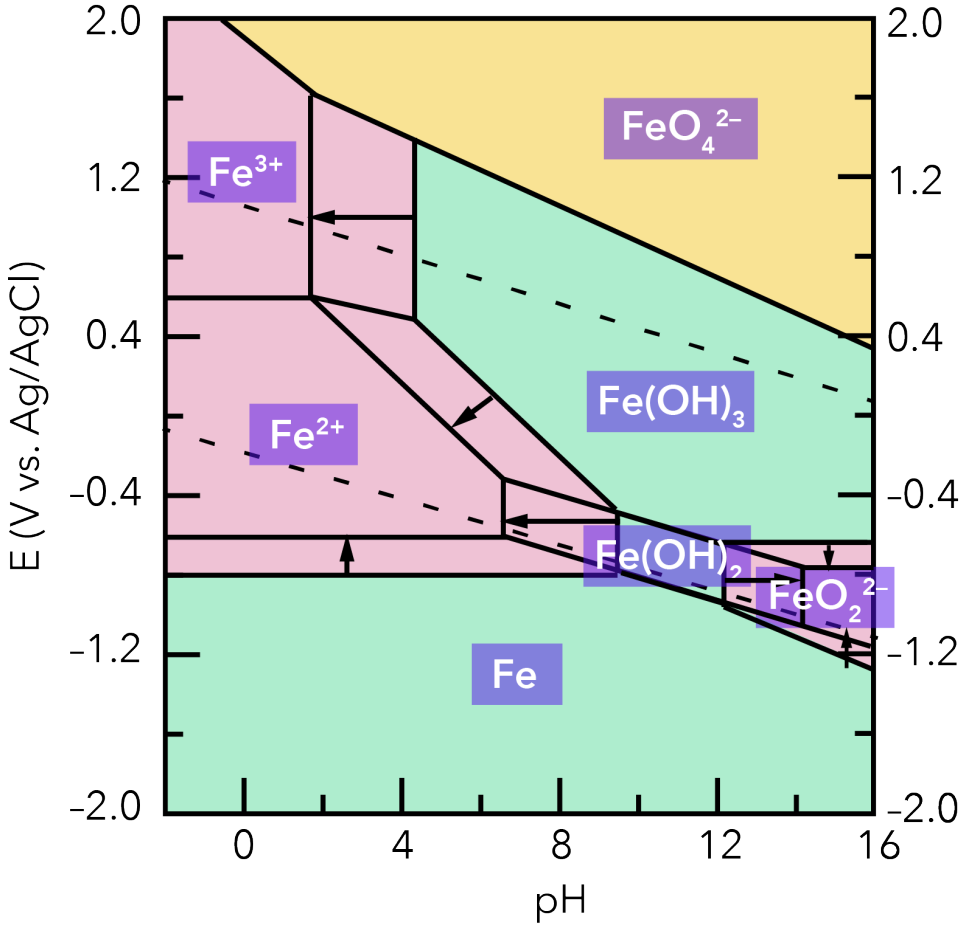


Figure 6.20. Pourbaix diagram for Fe in water, 25 °C. Colors indicate theoretical conditions for solid Fe (green) and soluble (red). FeO_4^{2-}, a species of interest for OER catalysts, is labeled in yellow. Arrow represents equilibrium shifting as $[Fe^{3+}]$ increases from 0.1 mM to 1 M. Dashed lines mark H_2/H^+ equilibrium (bottom) and H_2O/O_2 (top). Data from Reference 21.

There is a substantial body of work regarding the chemical behavior of FeO_4^{2-}, with interest in the space of wastewater treatment where FeO_4^{2-} is utilized industrially as an oxidant.[12,13,31–38] FeO_4^{2-} has a tetrahedral structure (Figure 6.20a).[39] Under acidic conditions, FeO_4^{2-} forms a bi-ferrate molecule, which can undergo inter-molecular oxo-coupling (Figure 6.20b).[31,32,34] At low pH, FeO_4^{2-} spontaneously decomposes according to the reaction,

$$2[H_4FeO_7]^{2+} \rightarrow 4Fe^{3+} + 8H_2O + 3O_2 \qquad \text{(Eq 6.3)}$$

It is known that the addition of potassium ferrate to water results in the evolution of oxygen.[32] Spontaneous O_2 evolution is also observed for CoP_i at low pH, where dissolution of the precatalyst results in O_2 formation.

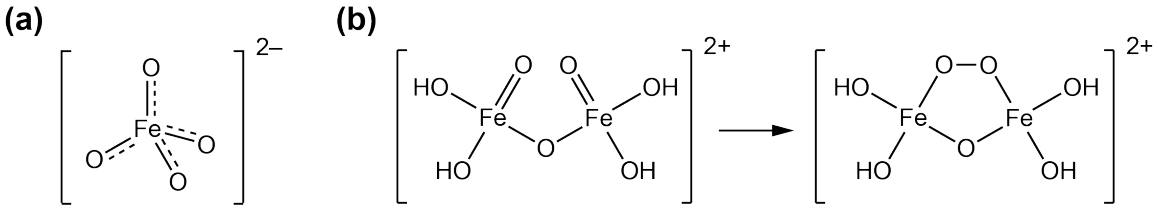


Figure 6.20. (a) Tetrahedral structure of ferrate. (b) Bi-ferrate structure formed under acidic conditions.

With a target species in mind that is in equilibrium with Fe^{3+}, the next step is to select a soluble Fe species to serve as the precatalyst. As discussed above, the solubility limit of the precatalyst will determine the favorability of the catalytic species. Fe^{2+} salts are an alternative Fe source, but since the ultimate species will have a redox state greater than Fe^{3+}, and since Fe^{3+} will be the thermodynamically favorable state under at open circuit potential in the presence of O_2, we decided to limit our search to Fe^{3+} salts. Some options for Fe precatalysts are listed in Table 6.3. Unfortunately, many Fe^{3+} salts are insoluble in water, but route provides a strategy for designing an acid-stable Fe OER system.

Table 6.3. Fe(III) Salts Solubility Table. Data from Reference 40.

Fe(III) compound	Solubility (g/100g H_2O)	Notes
Iron(III) acetate, basic	-	insoluble in H_2O, acid
Iron(III) 2,4-pentanediote	-	soluble in H_2O
Iron(III) arsenate dihydreate	-	insoluble H_2O, soluble in dilute acid
Iron(III) bromide	455	no entry
Iron(III) chloride	91.2	no entry
Iron(III) chloride hexahydrate	91.2	no entry
Iron(III) chromate	-	insoluble in H_2O, soluble in acid
Iron(III) citrate pentahydrate	-	soluble in H_2O
Iron(III) dichromate	-	soluble in H_2O and acid
Iron(III) ferrocyanide	5.92	insoluble in H_2O, dilute acids
Iron(III) fluoride	5.92	no entry
Iron(III) fluoride trihydrate	-	no entry
Iron(III) formate	-	soluble in H_2O
Iron(III) hydroxide	-	no entry
Iron(III) hydroxide oxide	-	insoluble in H_2O, soluble in acid
Iron(III) nitrate	82.5	no entry
Iron(III) nitrate hexahydrate	82.5	no entry
Iron(III) nitrate nonahydrate	82.5	no entry
Iron(III) oxalate	-	soluble in H_2O and acid
Iron(III) oxide	-	insoluble in H_2O, soluble in acid
Iron(III) phosphate dihydrate	-	insoluble in H_2O, soluble in HCl
Iron(III) pyrophosphate nonahydrate	-	insoluble in H_2O, soluble in acid
Iron(III) hypophosphite	-	insoluble H_2O
Iron(III) sodium pyrophosphate	-	insoluble in H_2O, soluble in HCl
Iron(III) sulfate	440	no entry
Iron(III) sulfate nonahydrate	440	no entry
Iron(III) biocyanate monohydrate	-	soluble in H_2O
Iron(III) metavanadate	-	insoluble in H_2O, soluble in acid

6.3.4.1 Fe(III) nitrate

After considering numerous Fe precatalyst candidates, we investigated $Fe(NO_3)_3$ due to its solubility. A challenge with designing an Fe^{3+} solution for OER is the relationship between $[Fe^{3+}]$ and the pH, and in turn, the redox potential for OER, as described qualitatively,

$$[Fe^{3+}] \propto pH^{-1} \propto E_{OER} \qquad \text{(Eq 6.4)}$$

This relationship is due to the decrease in pH incurred by the acidic nature of Fe^{3+}, which hydrolyzes water. It is therefore necessary to remain below 0.2 M $Fe(NO_3)_3$ to yield a pH of 3.

Electrolysis of 0.2 M $Fe(NO_3)_3$ at high overpotentials resulted in promising activity (Figure 6.11). (We discuss the curved Tafel in the proceeding section.) However, at an applied potential of 2.0 V, there was a substantial loss in activity, presumably from the oxidation of electrolyte (Figure 6.12), as suggested by an increase in resistance across the solution. The oxidation of nitrate to evolve nitrogen dioxide is a likely reaction that resulted in loss in electrolyte. It is known that NO_3^- can be oxidized at highly anodic potentials to NO_2^+ or N_2O_5, which eventually decomposes to highly toxic NO_2.[41] The threefold ratio of NO_3^- to Fe probably shifts the NO_3^-/NO_2^+ redox potential so that oxidation of NO_3^- can occur at a greater rate. The oxidation potential determining the stability of the electrolyte therefore represents another consideration in a electrolysis system designed to operate at a large overpotential. A straightforward remedy to this issue is substituting a portion of NO_3^- with another electrolyte, thereby shifting the oxidation NO_3^- to a higher potential. This is achieved in the $Fe(H_3C_2O_2)_3$ system as discussed in 6.3.6.

6.3.4.2 Fe(III) acetate

$Fe(H_3C_2O_2)_3$, known as basic iron, is used to generate non-acid solutions of Fe^{3+}. Notwithstanding, the solubility of $Fe(H_3C_2O_2)_3$ is limited, which is what gives rise to the lower pH. $Fe(H_3C_2O_2)_3$ was previously used as a stable thin film OER catalyst near pH 5.[29] It is reported to form a tri-nuclear oxo cluster in solutions of acetic acid.[42] Table 6.3 lists $Fe(H_3C_2O_2)_3$ as insoluble; however, using the filtration method described above, we were able to produce a very dark solution that were determined by UV-Vis spectrometry to contain 0.2 M in Fe with a measured pH of 3. We have yet to identify the soluble species.

Upon our Tafel analysis, the $Fe(H_3C_2O_2)_s$ solution produces large steady-state values that were sustained at a lower limit of 1-2 hr (Figure 6.13). No loss in current was observed beyond 2.0 V. However, at high overpotentials, the Tafel analysis was complicated by resistance issues. The large current results in a potentially significant influence from the Ohmic drop. For instance, using the instrument-measured resistance, we obtained a negative Tafel slope, while a lower limit in resistance produced a Tafel slope of 30 mV/dec. We were thus inclined to verify the instrument-measured resistance.

Using a CV method,[10] the uncompensated resistance, R_u, can be accurately determined from analysis of the double layer charging current, i_c. In a region absent of current caused by Faradaic processes, the double layer charging current is determined by

$$i_c = -C_d v \left[1 - \exp\left(-\frac{t}{R_u C_d}\right)\right] \tag{6.5}$$

where C_d is double layer charging capacitance, v is the scan rate, and t is time. The relationship between the cell resistance, R_e, and R_u, yields a "critical value" at their equivalence,

$$\Delta R_u = R_u - R_e = 0 \tag{6.6}$$

where R_e can be determined from the profile of the CV. As R_u approaches R_e, i_c becomes determined by the double layer capacitance, and the wave becomes rectangular. Beyond this critical value, oscillatory behaviors arises due to the bandpass limitations of the operation amplifiers used to generate the positive feedback compensation of the Ohmic drop. The results from CV measurements indicate that the potentiostat resistance measurement is accurate (6.14).

In light of our confidence in the value of R_e at open circuit potential, there are two explanations for the negative Tafel slope. In one scenario, the reaction forms a species at low current at the onset of the higher potential, which can then operate at lower potential more effi-

ciently than the species available at lower potentials prior to application of high potential. Such a species would be thermodynamically unstable, but perhaps persists due to the slow kinetics of decomposition. More likely, though, the negative Tafel slope can be explained by a change in the resistance. This occurs in the absence of supporting electrolyte, or when an active species participates in the double layer. Because $Fe(H_3C_2O_2)_3$ is in high concentration, it will likely be an important component in diffusion and charge transport. Therefore, a reaction involving could result in a change in resistance. Experiments are ongoing to identify the cause. Regardless, a R_e value of 20 Ω, approximately the resistance of FTO, can be substituted for the measured resistance as a lower limit.[6] This results in a Tafel slope of ~26 mV/dec, is still surprising low. The sustained high current density is attributed to the homogenous nature of the $Fe(H_3C_2O_2)_3$ system, which allows the high concentration of active sites to be continuously replenished, as activated $Fe(H_3C_2O_2)_3$ is transported away from the electrode. However, preliminary results indicate that current density is not mass transport limited at moderate overpotential. Kinetic studies will ultimately be necessary to determine the role of mass transport.

The Faradaic efficiency measurements illustrate that activity is approximately only due to OER (Figure 6.15). At high overpotential, we would anticipate CO_2 evolution from the oxidation of acetate. However, current is maintained, so electrolyte is not being significantly consumed. It is possible that a $Fe(H_3C_2O_2)_3$ cluster is responsible for stabilizing acetate in solution, although there is work to be done in analyzing the solution species. H_2O_2 or other high-energy intermediates are also possible, and decomposition of H_2O_2 catalyzed by $Fe(H_3C_2O_2)_3$ will have to be ruled out in future work.

In an effort to observe the active species, Spec-Echem was utilized (Figure 6.15). A shoulder at 275–320 nm and a feature at 510–560 is indicative of FeO_4^{2-}. In addition, bleaching

at 450 nm is observed. This may be caused as the red-orange $Fe(H_3C_2O_2)_3$ is converted to red-violet FeO_4^{2-}. The results are consistent with the formation of a steady state concentration of ferrate-like catalyst. We conclude that the $Fe(H_3C_2O_2)_3$ system should continue to be investigated as a possible source for a new variety of acid-stable molecular OER catalyst.

6.3.4.3 Fe(III) and Fe(II) sulfate

$Fe_2(SO_4)_3$ offers an alternative source of Fe^{3+}. However, it must be prepared from $FeSO_4$ in order to be solubilized. We speculate this is due to Fe^{3+} possessing SO_4^{2-} in the inner coordination sphere. Since the ligand exchange rate is slow, hydration (and therefore dissolution) occurs on a very slow timescale. Conversely, when the $FeSO_4$ is introduced into solution, an Fe^{2+} aquo complex is readily formed. Fe hydrolysis is preserved, even after oxidation to Fe^{3+} with H_2O_2. This system presents an alternative to $Fe(H_3C_2O_2)_3$ and $Fe(NO_3)_3$, but investigation into its electrochemical behavior is ongoing.

6.3.5 Towards engineering a competitive OER system

The concept of a soluble metal salt possessing functional stability toward high-current OER challenges fundamental conventions in the field of OER catalysis. In almost all contemporary electrochemical studies, the geometric surface area is used as a metric for predicting the efficiency, character, or otherwise prospect-for-success of a heterogeneous catalyst. This is because in these systems, the precatalyst must be condensed to the electrode surface in order to minimize its cost while optimizing accessible active sites. Even still, the idea of activity as a function of geometric surface area is always a falsehood, since many precatalysts can extend significantly away from the electrode, and all precatalysts at least have a z-height from the electrode. For the

Fe system, however, geometric surface area of the electrode is a poor indicator of competitiveness as an energy storage system. On the other hand, using molarity would assume that the Fe precatalyst species, let alone the Fe catalytic species, is stable enough to diffuse away from the electrode to form a homogenous concentration in solution. In any case, Fe, as one of the most affordable materials on the market, can be saturated in solution at a cost that is still competitive with other commodity base metals. Thus, once a conductive material is designed that can withstand the acidic and oxidizing potential, such as an FTO sponge,[43–45] Fe possesses a real prospect of serving as a competitive catalysis for energy storage applications.

6.4 Conclusion

Much of our dynamic precatalyst research is ongoing work. Nonetheless, some important results are discussed. Our work leads us to believe that CoP_i is a static catalyst that does not undergo continuous self-healing under OER conditions. This leads to the realization of optional pathways for Co-OEC to take in order to bypass dissolution. Moreover, the stability of CoP_i in neutral conditions appears to be the result of its environment, pointing to the role of O-binding in the catalyst film. We also gain insight into how the Co-OEC assembles on the surface of FTO.

Studies at low pH have revealed the importance of cell geometry considerations in procuring acid-stability in OER precatalyst films that are deposited at neutral pH. As such, the chemical stability of a film and thoughtful cell design (engineering) appear to be intertwined. The alternative to this strategy is to increase the precatalyst species. This has led to a new class of Fe-based acid-stable OER precatalysts that are dynamic in nature. The precatalyst structures and

active sites of these catalysts are of great interest in ongoing research efforts.

In OER, like all forms of catalysis, the currency of activity is the active site, and often, the active sites determine the efficiency of the system. The Fe system proposed here is unique in that it offers a high concentration of active sites using a scalable material. With that advantage, the geometric surface area metric of previous studies loses its significance, and assuming a high-surface area electrode can be fabricated, then the exchange current density of the Fe system increases, along with the efficiency of the system. We again find that the system's electrochemical performance can be improved by prudent engineering.

6.5 Experimental Methods

6.5.1 General electrochemical methods

All electrochemical experiments were conducted using a CH Instruments 760D bipotentiostat, a Pt-mesh counter electrode, and a BASi Ag/AgCl reference electrode (stored in saturated KCl). All electrochemical experiments were performed with a three-electrode setup and at ambient temperature (23 ± 1 °C). All potentials mentioned are referenced to Ag/AgCl (saturated KCl). Overpotentials for OER were calculated by correcting for resistance (E – iR, unless otherwise noted), correcting for a shift of –59 mV/pH, and converting the potential reference to Normal Hydrogen Electrode (+0.197 mV) for comparison with literature redox potential values. 0.1 M electrolyte solutions were prepared from KH_2PO_4 (99.0%, Alfa Aesar), H_3PO_4 (85 wt. %, >99.999% trace, Sigma Aldrich) K_2SO_4, (99.0%, Alfa Aesar), and HNO_3 (70 wt. %, >99.999% trace metal, Sigma Aldrich).

For pH 2.5–5.5 KP_i solutions, the pH of was adjusted by varying the ratio between 0.1 M H_3PO_4 and 0.1 M KH_2PO_4. The pH was measured using a VWR pH probe. For KPi pH 7 buffer, KOH pellets were added to 0.1 M KH_2PO_4.

6.5.3 Co-OEC precatalyst preparation

Electrodes were prepared by defining a 1 cm × 1 cm square surface on FTO using 3M Kapton tape. Films of CoP_i catalyst were deposited at 0.85 V in 0.5 mM Co^{2+} solutions made from $Co(NO_3)$ (99.999% trace metals, Sigma Aldrich) and 0.1 M K KPi, pH 7.

To fabricate 50 μm disks of CoP_i, FTO was first coated with S1805 photoresist at 4000 rpm for 45 s. Samples were baked at 115 °C for 2 min. 50 μm diameter circular openings were exposed over the surface using a Heidelberg μPG501 photowriter. Samples were developed in CD-26 for 3 min and washed thoroughly with water. CoP_i was then deposited into the circular openings following the deposition procedure above. Resists were removed with acetone and the substrates were rinsed with Type 1 water.

0.2 M $Fe(NO_3)_3$ was prepared by saturating 10 mL Type 1 H_2O with 11 g $Fe(NO_3)_3$ (99.999% trace metal, Sigma Aldrich), then diluting the solution to pH 3. The concentration of $Fe(NO_3)_3$ was determined using UV-Vis analysis (comparing to known concentrations of $Fe(NO_3)_3$ in concentrated HCl).

$Fe(H_3C_2O_2)_3$ catalysts were prepared by dissolving 1 g Fe (99.6%, ChemSavers) in 50 mL 0.1 M HNO_3. (Nitric acid was necessary to obtain a pH of 3.) The solutions were filtered using a 0.2 μm pore filter (Corning). 0.2 M $Fe(II)S_i$ was prepared by adding $FeSO_4$ (99.999% trace metal, Sigma Aldrich) to 0.1 M H_2SO_4. 0.2 M $Fe(III)S_i$ was prepared by adding $Fe_2(SO_4)_3$ (99.999% trace metal, Alfa Aesar) to 0.1 M K_2SO_4. The solution was then oxidized by adding 1

mL H_2O_2 (30% wt., Sigma Aldrich), allowing excess H_2O_2 to decompose for 48 hr. Since this procedure produces a dilute Piranha acid, it was necessary to use acid-washed glassware vials, whereas other solutions were prepared in 50 mL centrifuge tube (Falcon).

6.5.4 Detecting Co migration using a four-electrode configuration

100 mC/cm^2 CoP_i films were deposited on FTO. The CoP_i-coated electrode (E1), a second electrode (E2), and the reference electrode were both suspended in a 50 mL 0.1 M KPi solution (pH 7) in a 50 mL working compartmented separated by a frit from 50 mL counter compartment filled with 40 mL of the same solution. E2 was held at a potential for 72 hr. Co was extracted from the solution *in situ* using a second working electrode (E2) poised at 0.85 V to ensure formation of Co^{3+}. Co^{3+} was then measured on the electrodes by poising electrodes at 1 V. The solution was stirred with a stir bar rotating at ~200 rpm.

6.5.5 Spectrometric quantification of Co

Co and Fe concentrations were analyzed by dissolving the metal salts in concentrated HCl. The spectra of the HCl solutions were measured using a Cary 5000 UV-Vis spectrophotometer. Spectra of the HCl solutions were compared to titration curves measured from absorbance intensity of solutions ranging from 0–1 mM, with 20 μM increments. Intensities used for Co and Fe were the peak maximums at 691 nm and 362 nm, respectively.

6.5.6 O_2 measurements

An Ocean Optics oxygen sensor was utilized for measuring O_2 evolved in an air-tight cell. Calculations for O_2 were made following the Stern-Volmer relationship. The solution and

headspace were purged with N_2 for an hour and the sensor was placed in the headspace. Electrolysis was performed at 1.0 V (vs. Ag/AgCl) in 0.1 M KPO_4 (pH 7.0) for 10 h.

Gas chromatography utilized a custom-built, two-compartment electrochemical cell, in which an Ar carrier gas flowed from the cell to the thermal conductivity equipped GC (SRI Instrument). The flow pressure was set to 0.12 psi. Peaks were integrated and compared to the charge passed to determine the Faradaic efficiency.

6.5.7 *In situ* electrochemical UV-Vis spectroscopy

Spec-Echem spectra were taken of a diluted solution of $Fe(H_3C_2O_2)_3$ using a DT-Mini-2-GS ocean optics UV-Vis Spectrophotometer in a 1 mm path-length cuvette using a flag mesh Pt working electrode. Electrolysis at 1.8 V was run for 20 min. The reference electrode and Pt wire counter electrode were suspended in solution above the working electrode. Spectra were collected every 200 s.

6.5.8 Microscopy

Field emission SEM was performed with a Zeiss Supra55VP with InLens and SE2 detectors (Carl Zeiss AG) operating at 3 kV. EDS maps were acquired on an SEM operating at 7 kV with 60 μm aperture size and WD = 8.5 mm. Optical microscopy was performed using an Axio Scope.A1 microscope with a 50× objective and an AxioCam ICc 5 (all components Carl Zeiss Microscopy).

6.6 References

(1) McKone, J. R.; Lewis, N. S.; Gray, H. B *Chem. Mater.* **2014,** *26,* 407–414.

(2) Spöri, C.; Kwan, J. T. H.; Bonakdarpour, A.; Wilkinson, D. P.; Strasser, P. *Angew. Chem.;* **2017**, *56,* 5994–6021.

(3) Schinde, A.; Jones, R. J. R.; Guevarra, D.; Mitrovic, S.; Becerra-Stasiewicz, N.; Haber, J. A.; Jin, J.; Gregoire, J. M. *Electrocatalysis;* **2015**, *6,* 229–236.

(4) Fabbri, E.; Nachtegaal, M.; Binninger, T.; Cheng, X.; Kim, B-J.; Durst, J.; Bozza, F.; Graule, T.; Schäublin, R.; Wiles, L.; Pertoso, M.; Danilovic, N.; Avers, K. E.; Schmidt, T. J. *Nat. Mat.;* **2017**, *16,* 925–931.

(5) Ledendecker, M.; Mondschein, J. S.; Kasian, O.; Geiger, S.; Göhl, D.; Schalenback, M.; Zeradjanin, A.; Cherevko, S.; Schaak, R. E.; Mayrhofer, K. *Angew. Chem. Int. Ed.* **2017,** *56,* 9767–9771.

(6) Huynh, M.; Ozel, T.; Liu, C.; Lau, E. C.; Nocera, D. G. *Chem. Sci.;* **2017**, *8,* 4779–4794.

(7) McKone, J. R.; Lewis, N. S.; Gray, H. B. *Chem. Mater.;* **2014**, *26,* 407–414.

(8) Martindale, B. C. M.; Reisner, E. *Adv. Ener. Mat.* **2016,** *6,* 1–9.

(9) Diaz-Morales, O.; Raaijman, S.; Kortlever, R.; Kooyman, P. J.; Wezendonk, T.; Gascon, J.; Fu, W. T.; Koper, M. T. M. *Nat. Comm.* **2016,** *7,* 1–6.

(10) Savéant, J-M. *Elements of Molecular and Biomolecular Electrochemistry*. John Wiley & Sons, Inc. Hoboken, New Jersey, 2006. Pg. 14

(11) Liu, C.; Colón, B.; Ziesack, M.; Silver, P. A.; Nocera, D. G. *Science,* **2016,** *352,* 1210–1213.

(12) Bielski, B. H. J.; Thomas, M. J.; *J. Am. Chem. Soc.;* **1987**, *109,* 7761–7764.

(13) Lee, Y.; Cho, M.; Kim, J. Y.; Yoon, J. *J. Ind. Eng. Chem.,* **2004,** *10,* 161–171.

(14) Surendranath, Y.; Dinca, M.; Nocera, D. G. *J. Am. Chem. Soc.;* **2009**, *131,* 2615–2620.

(15) Lutterman, D. A.; Surendranath, Y.; Nocera, D. G. *J. Am. Chem. Soc.;* **2009**, *131,* 3838–3839.

(16) Constentin, C.; Nocera, D. G. *PNAS* **2017,** *114,* 13380–13384.

(17) Ullman, A. M.; Brodsky, C. N.; Li, N.; Zheng, S.-L.; Nocera, D. G. *J. Am. Chem. Soc.* **2016,** *138,* 4229–4236.

(18) Surendranath, Y.; Lutterman, D. A.; Nocera, D. G. *J. Am. Chem. Soc.* **2012,** *134,* 6326–6336.

(19) Gerken, J. B.; McAlpin, J. G.; Chen, J. Y. C.; Rigsby, M. L.; Casey, W. H.; Britt, R. D.; Stahl, S. S. *J. Am. Chem. Soc.* **2011,** *133,* 14431–14442.

(20) Bloor, L. G.; Molina, P. I.; Symes, M. D.; Cronin, L. *J. Am. Chem. Soc.* **2014,** *136,* 3304–3311.

(21) Pourbaix, M. *Atlas of Electrochemical Equilibria in Aqueous Solutions,* Pergamon Press: Oxford, 1966.

(22) Surendranath, Y.; Kanan, M. W.; Nocera, D. G. *J. Am. Chem. Soc.* **2010,** *132,* 16501–16509.

(23) Hassanali, A.; Giberti, F.; Cuny, J.; Kühne, T. D.; Parrinello, M. *PNAS* **2013,** *110,* 13723–13728.

(24) Olivetti, E. A.; Ceder, G.; Gaustad, G. G.; Fu, X. *Joule.* **2017,** *1,* 229–243.

(25) Lutgens, F. K.; Tarbuck, E. J. *Essentials of Geology*, 7th Ed.; Prentice Hall: 2000.

(26) Chemelewski, W. D.; Lee, H.-C.; Lin, J.-F.; Bard, A. J.; Mullins, C. B. *J. Am. Chem. Soc.*

2014, *136,* 2843–2850.

(27) Zou, S.; Burke, M. S.; Kast, M. G.; Fan, J.; Danilovic, N.; Boettcher, S. W. *Chem. Mater.;* **2015**, *27,* 8011–8020.

(28) Li, F.; Bai, L.; Li, H.; Wang, Y. *Chem. Comm.;* **2016**, *52,* 5753–5756.

(29) Wu, Y.; Chen, M.; Han, Y.; Luo, H.; Su, X.; Zhang, M.-T.; Lin, X.; Sun, J. Wang, L.; Deng, L.; Zhang, W.; Cao, R. *Angew. Chem. Int. Ed.;* **2015**, *54,* 4870–4875.

(30) Commodity and metal price charts. http://www.infomine.com/investment/metal-prices/ (accessed April 4, 2018).

(31) Barışçı, S.; Dimoglo, A. *Ferrites and Ferrates: Chemistry and Applications in Sustainable Energy and Environmental Remediation.* Washington, ACS Symposium Series: 2016. Ch. 12.

(32) Sarma, R.; Angeles-Boza, A. M.; Brinkley, D. W.; Roth, J. P. *J. Am. Chem. Soc.* **2012,** *134,* 15371–15386.

(33) Gan, W.; Sharma, V. K.; Zhang, X.; Yang, L. Yang, X. *J. Hazard. Mat.* **2015,** *292,* 197–204.

(34) Liu, X.; Wang, F. *Coord. Chem. Rev.* **2012,** *256,* 1115–1136.

(35) Yates, B. J.; Zboril, R.; Sharma, V. K. *J. Environ. Sci. Health, Part A* **2014,** *49,* 1603–1614.

(36) Song, Y.; Deng, Y.; Jung, C. *Chemosphere* **2016,** *146,* 145–153.

(37) Liu, Y.; Wang, L.; Ma, J.; Zhao, X.; Huang, Z. Mahadevan, G. D.; Qi, J. *Chem. Eng. J.* **2016,** *287,* 11–18.

(38) Barışçı, S.; Ulu, F.; Sillanpää, M.; Dimoglo, A. *J. Chem. Technol. Biotechnol.* **2015,** *91,* 257–266.

(39) Hoppe, M. L.; Schlemper, E. O.; Murmann, R. K. *Acta Cryst.* **1982,** *B38,* 2237–2239.

(40) Lide, D. R. *CRC Handbook of Chemistry and Physics*, 84th ed.; CRC Press LLC: 2004.

(41) Lund, H.; Hammerich, O. *Organic Electrochemistry*, 4th ed.; Marcel Dekker, Inc.: New York, 1991.

(42) Vrubel, H.; Hasegawa, T.; de Oliveira, E.; Nunes, F. S. *Inorg. Chem. Comm.* **2006,** *9,* 208–211.

(43) Das, N.; Jana, S.; Biswas, P. K. *Sci. Adv. Mat.* **2014,** *6,* 252–262.

(44) Aprile, C.; Terual, L.; Alvaro, M.; Garcia, H. *J. Am. Chem. Soc.* **2009,** *131,* 1342–1343.

(45) Biswas, P. K.; Das, N. *Mater. Sci.* **2015,** *9,* 126–131.

Page intentionally left blank.

"There must be no barriers to freedom of inquiry. There is no place for dogma in science. The scientist is free, and must be free to ask any question, to doubt any assertion, to seek for any evidence, to correct any errors. Our political life is also predicated on openness. We know that the only way to avoid error is to detect it and that the only way to detect it is to be free to inquire. And we know that as long as men are free to ask what they must, free to say what they think, free to think what they will, freedom can never be lost, and science can never regress."

-J. Robert Oppenheimer
Life, 139 (Oct 10, 1949)